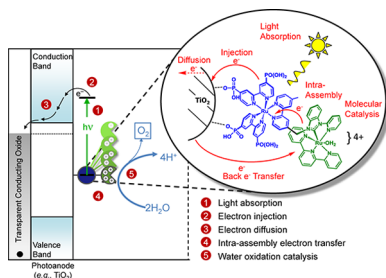


## Molecular Chromophore–Catalyst Assemblies for Solar Fuel Applications

Dennis L. Ashford,<sup>†</sup> Melissa K. Gish,<sup>†</sup> Aaron K. Vannucci,<sup>‡</sup> M. Kyle Brenneman,<sup>†</sup> Joseph L. Templeton,<sup>†</sup> John M. Papanikolas,<sup>†</sup> and Thomas J. Meyer\*,<sup>†</sup>

<sup>†</sup>Department of Chemistry, University of North Carolina at Chapel Hill, CB 3290, Chapel Hill, North Carolina 27599, United States

<sup>‡</sup>Department of Chemistry and Biochemistry, University of South Carolina, Columbia, South Carolina 29208, United States



### CONTENTS

1. Introduction	13006
2. Photoelectrochemical (PEC) Cells	13007
2.1. Water Oxidation	13008
3. Dye-Sensitized Photoelectrosynthesis Cells (DSPECs)	13010
3.1. Single-Photoelectrode DSPEC	13010
3.2. Tandem DSPEC	13011
3.3. Chromophore–Catalyst Assemblies	13011
3.4. The Oxide Semiconductor	13011
3.4.1. Surface Attachment and Stabilization	13012
3.5. Light Absorption	13013
3.6. Excited-State Potentials	13014
3.6.1. Electron Injection	13014
3.7. Water Oxidation	13015
3.7.1. Atom–Proton Transfer (APT)	13016
3.7.2. Nonaqueous Solvent	13016
3.7.3. Sun's bda Catalysts	13016
3.7.4. Water Oxidation on Oxide Surfaces	13016
3.7.5. Water Oxidation in Assemblies	13017
3.7.6. Rates	13017
3.8. Intra-assembly Electron Transfer: Catalyst Activation	13017
3.9. DSPEC Dynamics	13018
3.9.1. Core/Shell Advantage	13018
3.9.2. Cross-Surface Electron Transfer Activation and Accumulation of Redox Equivalents	13019
4. Chromophore–Catalyst Assemblies in Solution	13020
5. Chromophore–Catalyst Assemblies on Oxide Surfaces	13021
5.1. Surface Loading	13022
5.2. Oxide-Bound Assemblies	13022
6. Electrocatalytic Water Oxidation	13025
7. Assembly Interfacial Dynamics	13026
7.1. Kinetic Scheme	13026
7.2. Kinetic Efficiencies	13027

7.3. Electron Injection	13028
7.4. Assembly Injection	13029
7.5. Electron-Transfer Activation of the Catalyst	13029
7.6. Back Electron Transfer (BET)	13029
8. DSPEC Water Splitting	13031
8.1. Introduction	13031
8.1.1. Surface Binding and Stability	13031
8.1.2. pH and Buffer Base Effects	13031
8.1.3. Chromophore–Catalyst Stability	13031
8.1.4. Multi-Chromophore Advantage	13032
8.1.5. O <sub>2</sub> Measurements	13032
8.1.6. Initial Experiments: Related Results	13032
8.2. Water Splitting by Chromophore–Catalyst Assemblies	13033
9. Evaluating DSPEC Performance	13035
10. Postscript	13036
Author Information	13036
Corresponding Author	13036
Notes	13036
Biographies	13036
Acknowledgments	13038
Abbreviations	13038
References	13038

### 1. INTRODUCTION

As the world's population increases, the U.S. Department of Energy has estimated that energy consumption will increase with it, increasing from  $5.7 \times 10^{20}$  J in 2012 to  $8.1 \times 10^{20}$  J in 2040. This projection takes into account population growth, average gross domestic product per capita, and globally averaged energy intensity.<sup>1</sup> At the same time, there is an increased understanding of the importance of integrating good environmental practices with stimulating economic growth and leadership provided by international organizations, such as the Organization for Economic Cooperation and Development. Most of the increases in energy consumption will come from emerging economies in Asia, Africa, and South America where goals, priorities, and challenges are diverse. To meet these demands there is a need to develop alternate energy sources. Although renewable and nuclear energy are growing by 2.5% a year, fossil fuels are still projected to make up at least 80% of the global energy supply in 2040 (Figure 1).

**Special Issue:** Solar Energy Conversion

**Received:** April 16, 2015

**Published:** October 29, 2015

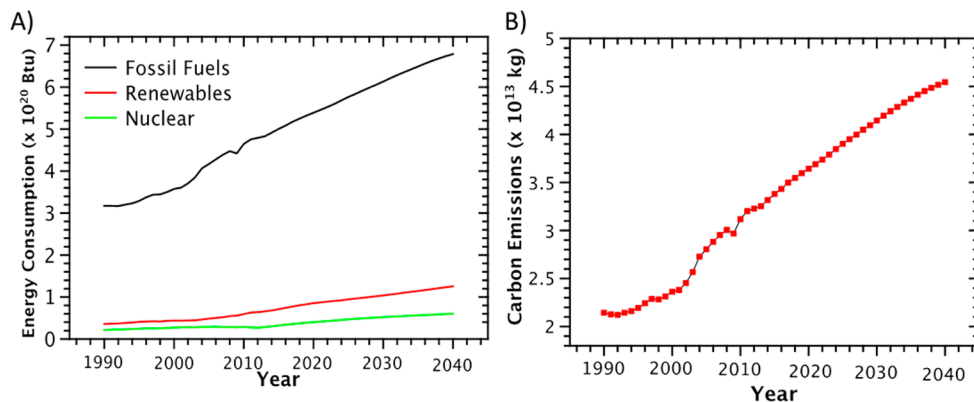


**Figure 1.** (A) World energy consumption (in British thermal units, Btu) of fossil fuels (black), renewables (red), and nuclear energy (green). (B) World carbon emissions per year. Data obtained from the Energy Information Administration, with values past 2012 predicted on the basis of current models.<sup>1</sup>

Fossil fuel reserves are predicted to last from less than 100 years to millennia based on current and anticipated future consumption.<sup>2–5</sup> There are uncertainties in estimates of fossil fuel reserves, but the potential for debilitating and possibly devastating environmental impacts arising from the combustion of fossil fuels creates a second imperative for developing alternate energy sources. In 2012 alone,  $3.21 \times 10^{13}$  kg of carbon dioxide was released into Earth's atmosphere from fossil fuels (Figure 1).<sup>1</sup> The atmospheric CO<sub>2</sub> concentration has risen above 400 ppm, a level not seen in the Earth's atmosphere in 450,000–600,000 years.<sup>2,6–9</sup> Release of hydrocarbons to the atmosphere is of increasing concern given their efficacy as greenhouse gases, but there are natural mechanisms for removing them from the atmosphere. In contrast, there are no natural mechanisms for removing CO<sub>2</sub> in the upper atmosphere and mixing between upper atmospheric CO<sub>2</sub> and the biosphere is slow, taking from 400 to several thousand years. As a result, CO<sub>2</sub> released during this century will remain in the atmosphere for 500–2000 years.<sup>2,9,10</sup>

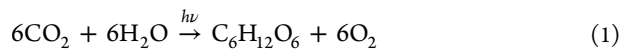
It is unclear what the optimal mix of renewable energy sources—wind, solar, geothermal, nuclear, biomass—will be in the future and how the mix will vary as renewable sources are phased in and hydrocarbons phased out. The current U.S. Secretary of Energy has discussed an “all of the above” strategy, with each energy source finding its place consistent with strategic planning for the future and the economic realities of the market place. Of the available renewable sources, the sun is, by far, the largest in availability and is the most likely long-term solution as the dominant primary, carbon-neutral energy source.<sup>2,11</sup> A solar energy conversion device collecting and converting all of the sunlight striking just 2% of the Earth's surface for 8 h with an energy conversion efficiency of 12% would be sufficient to satisfy global energy consumption for 2 weeks.<sup>1</sup>

Nonetheless, there are considerable obstacles to bringing solar energy on line as a primary energy source. Rain, clouds, and, especially, the diurnal sun cycle create energy storage demands on massive, as-yet unrealized scales. The sun is, also, not an ideal light source because it is diffuse. Using it at the required scale will necessitate vast collection areas. Its viability at the required scale mandates relatively high solar-to-energy conversion efficiencies and the use of inexpensive, Earth-abundant materials.

Today, photovoltaics (PVs) are produced on commercial scales that can directly convert solar energy into electricity with

recently reported efficiencies of up to 44.7% in multi-junction solar cells.<sup>12</sup> The solar energy harvested in PV devices can be stored in external batteries. The most efficient and lightweight batteries are typically Li<sup>+</sup> ion batteries, but current state-of-the-art Li<sup>+</sup> ion battery technology is unable to meet global energy storage demands, with a storage capability of only ~1.03 A·h/g, along with limited stability of many charge/discharge cycles.<sup>13–19</sup>

Artificial photosynthesis offers a way to overcome these challenges. The natural photosynthetic apparatus is remarkably complex. It has evolved over billions of years and uses sunlight to drive the reduction of CO<sub>2</sub> by water to make carbohydrates and oxygen (eq 1) with energy stored as adenosine

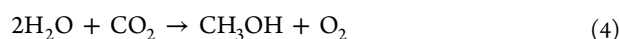
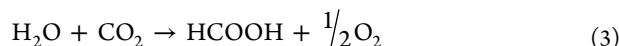


triphosphate.<sup>20–23</sup> However, photosynthesis is inefficient, converting only ~1% of the incident sunlight into biomass, with the remainder used for signaling, growth, and other energy demands.<sup>24–27</sup> Although biomass will continue to have its place in the world's energy mix, far higher efficiencies are needed to power the world's increasingly urban, industrialized economies.

Artificial photosynthesis looks to the natural analogue for inspiration and knowledge of fundamental processes but with greatly simplified strategies for converting sunlight into fuels. The targets are hydrogen from water splitting or CO<sub>2</sub> reduction to carbon-based fuels. A promising approach is available by using photoelectrochemistry. The results of a recent analysis suggest that photoelectrochemical cells operating with a solar efficiency of 10% could replace fossil fuels as the world's primary energy source.<sup>28,29</sup>

## 2. PHOTOLECTROCHEMICAL (PEC) CELLS

The artificial photosynthetic target of water splitting to give hydrogen is shown in eq 2, and solar-driven reduction of CO<sub>2</sub> by water to give the 2e<sup>-</sup> product formic acid is shown in eq 3. More highly reduced carbon targets are an ultimate goal; reduction to methanol is shown in eq 4.



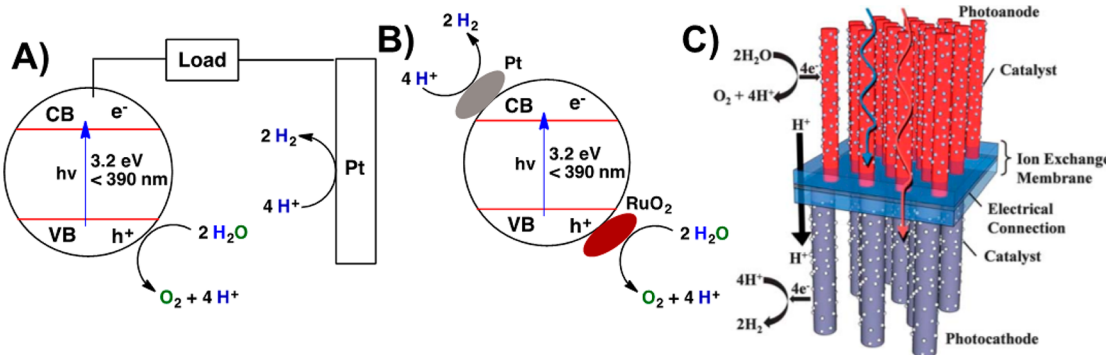


**Figure 2.** (A) Honda–Fujishima photoelectrochemical cell with TiO<sub>2</sub> as the photoanode.<sup>45</sup> (B) Illustrating a single semiconductor nanoparticle with RuO<sub>2</sub> as the water oxidation catalyst and Pt the reduction catalyst.<sup>59</sup> (C) PEC cell proposed by JCAP with nanowire arrays for light harvesting.<sup>70</sup> Reprinted from ref 70 with permission from the Royal Society of Chemistry.

In a photoelectrochemical cell, the reactions in eqs 2–4 are carried out by separate half-reactions for oxidation and reduction. The half-reactions for CO<sub>2</sub> reduction by H<sub>2</sub>O to give HCOOH and CH<sub>3</sub>OH are illustrated in eqs 3 and 4, respectively. In these reactions the O<sub>2</sub>/H<sub>2</sub>O couple is the essential “other” half-reaction, with water providing the reductive equivalents needed to produce hydrogen or a reduced carbon product and O<sub>2</sub> evolved as a useful byproduct. In either case, it is notable that subsequent direct or indirect combustion of H<sub>2</sub> to give water or of a reduced form of carbon to give CO<sub>2</sub> with recapture of CO<sub>2</sub> provides a basis for a renewable, closed cycle without impact on the environment:



## 2.1. Water Oxidation

In both natural and artificial photosynthesis, the thermodynamic, mechanistic, and kinetic requirements that arise from light-driven oxidation of water pose a significant challenge. The thermodynamic potential for water oxidation at pH 0 is 1.23 V vs the normal hydrogen electrode (NHE). It is pH dependent, decreasing with increasing pH by 59 mV/pH, as predicted by the Nernst equation, eq 7,

$$E = E^\circ - \frac{0.059m}{n} \log_{10} \frac{1}{a_{\text{H}^+}} \quad (\text{STP, } 25^\circ\text{C}) \quad (7)$$

with *m* the number of protons transferred, *n* the number of electrons transferred, and *a*<sub>H<sup>+</sup></sub> the activity of protons in the prevailing medium. Given the pH dependence of the half-reaction, the potential for water oxidation is 0.82 V at pH 7 and 0.40 V at pH 14.<sup>30–32</sup>

Numerous water oxidation catalysts (WOCs) have been identified, and detailed mechanistic insight is available about how this reaction occurs at single sites, assemblies, and clusters.<sup>30–37</sup> As discussed below for a single-site catalyst, proton-coupled electron transfer (PCET) is key with coupled electron/proton loss used to avoid electrostatic charge buildup. This allows for the accumulation of multiple redox equivalents at single sites over a narrow potential range.<sup>38–42</sup> In these catalytic cycles, electron/proton loss gives an active oxo-form of the catalyst. The M=O oxo group provides the molecular orbital basis for O-atom transfer, giving O–O bond formation, which is often the rate-limiting step in overall water oxidation cycles.

An additional challenge comes from integrating light absorption and catalysis in functional architectures at the molecular scale. In an efficient device, the rate of catalytic turnover exceeds the rate of solar insolation with light absorption being the rate-limiting step. In a commercial device undergoing millions of turnovers per year, a catalyst needs to be highly robust or be easily replaceable.<sup>43,44</sup> Demands on stability are severe in an operating device with performance sustained indefinitely under ambient sunlight free of deleterious decomposition pathways. In solar concentrator devices with large area collectors and a small active surface area, the demands arising from rate and robust behavior are even higher.

Multiple device architectures have been proposed for artificial photosynthesis. An early and remarkably simple approach was reported by Honda and Fujishima in 1972. They reported that water splitting into H<sub>2</sub> and O<sub>2</sub> occurred following ultraviolet (UV) excitation of anatase (titanium dioxide, TiO<sub>2</sub>) in a PEC cell with a Pt cathode and a small applied bias in acidic solution (Figure 2A).<sup>45</sup> Direct band gap excitation of TiO<sub>2</sub> nanoparticles (3.2 eV, <390 nm) generates highly oxidizing holes (h<sup>+</sup>) in the valence band which undergo hydroxyl radical-like chemistry with water at the surface. Oxidation of water frees conduction-band electrons for transfer to the cathode for H<sup>+</sup> reduction to H<sub>2</sub>. An external bias is required to maximize photocurrents to boost the potential of conduction-band electrons to drive proton reduction to H<sub>2</sub> to completion.

The semiconductor strategy relies on a single material for light absorption, charge transport, and water oxidation catalysis, all of which are separately demanding. It is also limited to UV irradiation and direct band gap excitation which limits device efficiencies since less than 10% of the solar spectrum is usable. Substantial progress has been made in improving semiconductor efficiencies for water splitting by controlling band gap and band edges to more closely match the thermodynamic requirements for water splitting while harvesting a greater portion of the solar spectrum.<sup>46–53</sup> However, rapid electron/hole recombination and photocorrosion remain significant challenges in this area.<sup>54–58</sup>

As shown in Figure 2B, a second architecture derived from the Honda–Fujishima design employs light-absorbing semiconductors derivatized with water oxidation and reduction catalysts. It has the advantage of separating light absorption and charge transport from catalysis. This approach greatly decreases the demands on the semiconductor and allows separate development of catalysts and catalyst design. In an early

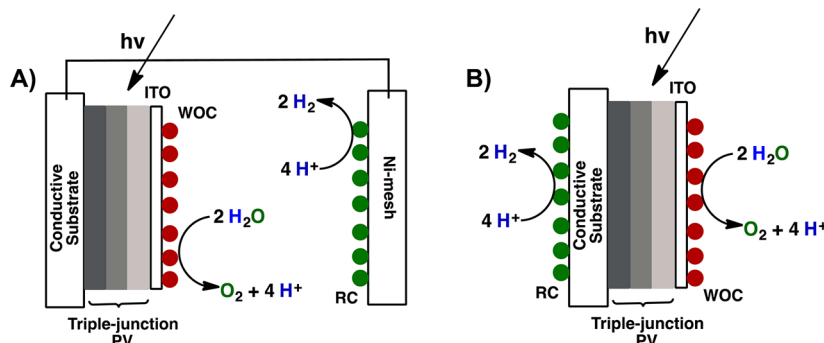


Figure 3. PV electrolysis cell with triple-junction Si PV device as the light harvester, wired (A) and wireless (B).

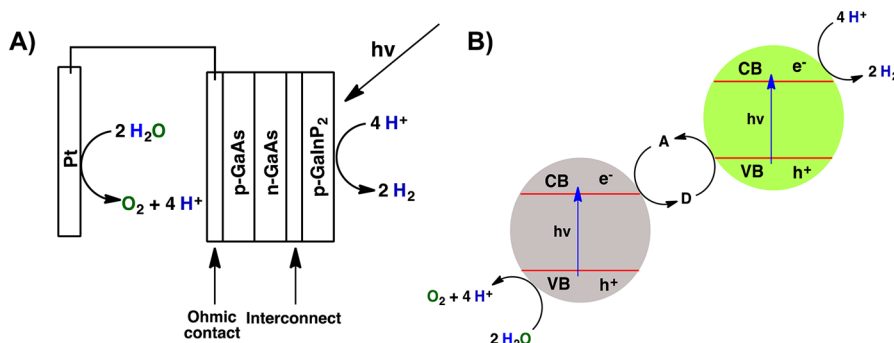


Figure 4. (A) Single GaAs p–n junction cell with a p-type GaInP<sub>2</sub> cathode.<sup>77</sup> (B) Schematic diagram of a two-photocatalyst Z-scheme based on nanoparticles in solution.

example, Grätzel and co-workers published an important early result with RuO<sub>2</sub> as the WOC and Pt as the proton reduction catalyst, with both on the surfaces of TiO<sub>2</sub> nanoparticles (Figure 2B).<sup>59</sup> Efficiencies were low due to back electron transfer (BET) and photocorrosion.<sup>60–66</sup>

A more elaborate strategy based on catalyst-derivatized, light-absorbing nanostructured semiconductor materials (Figure 2C) has been proposed by the Joint Center for Artificial Photosynthesis (JCAP). In this design, p-type Si nanowires derivatized with a reduction catalyst are used as the photocathode, with an array of metal oxide semiconducting nanowires derivatized with WOCs as the photoanode.<sup>67–71</sup> In a recent example, it was demonstrated that p-type silicon nanowires surface-modified with a Mo<sub>3</sub>S<sub>4</sub> cluster were capable of achieving a 10% solar-to-hydrogen (STH, Section 9) conversion efficiency with hydrogen oxidation occurring at the anode.<sup>72</sup> The STH efficiencies were obtained with broadband irradiation from a solar simulator at AM 1.5G without an external bias.<sup>73</sup>

Combining PVs and catalysts for water electrolysis is a proven technology with long-term device efficiencies demonstrated. In this architecture, the PV device produces an electrochemical bias in an electrochemical cell with catalytic anodes and cathodes. An early example for generation of solar fuels was reported by Rocheleau et al. in 1998. They modified a triple-junction amorphous-Si PV cell with Co<sub>0.73</sub>Mo<sub>0.27</sub> reduction and NiFe<sub>x</sub>O<sub>y</sub> WOCs.<sup>74</sup> A STH efficiency of 7.8% was reported for a 0.27 cm<sup>2</sup> device. In a more recent example reported by Nocera and co-workers, the anode was surface-modified with a Co-borate WOC, with the cathode a NiMoZn reduction catalyst (Figure 3).<sup>28</sup> With a 2 cm<sup>2</sup> electrode in 1 M K<sub>3</sub>BO<sub>3</sub> (pH 9.2) as electrolyte, a STH efficiency of 4.7% was achieved.<sup>44,75,76</sup> A wireless configuration was also described

with a buried junction offering the advantage of simplicity of design with an eye toward potential commercial applications (Figure 3). A disadvantage in this configuration is the lack of a provision for rapid pH equilibration which leads to pH gradients with associated *iR* drops and loss of cell efficiency.

In a different approach, a single p–n junction PV device has been used to apply an electrochemical potential to catalytically active electrodes. An early example was reported by Turner and Khaselev who used a single GaAs p–n junction to bias a p-type GaInP<sub>2</sub> photocathode (Figure 4A).<sup>77</sup> This design resulted in an impressive 12.4% STH efficiency but with significant photocorrosion and at high cost ( $\sim \$50,000\text{ m}^{-2}$ ). Both remain major challenges to overcome.<sup>78</sup>

An architecture resembling the Z-scheme of natural photosynthesis (Figure 4B) was described by Bard in 1979.<sup>79</sup> In photosynthesis, reduction of NADP to NADPH occurs at photosystem I (PSI) and water oxidation at photosystem II (PSII). Photosynthesis uses a tandem “Z-scheme” which integrates physically separated photochemical reactions. As in any tandem scheme, there is an inherent loss in efficiency because two photons are used rather than one. However, a tandem configuration offers far greater redox potentials for driving the separate half-reactions.<sup>64,80–83</sup>

In the Bard tandem cell, water oxidation and reduction were driven at separate nanoparticle photocatalysts in solution. As shown in Figure 4B, the half-reactions were interconnected by an added donor/acceptor diffusional redox couple. Maeda et al. used Pt-loaded ZrO<sub>2</sub>/TaON nanoparticles with TaON as the reductive catalyst, and PtO<sub>x</sub>/WO<sub>3</sub> nanoparticles with WO<sub>3</sub> as the oxidative catalyst with added IO<sub>3</sub><sup>-</sup>/I<sup>-</sup> as the redox shuttle, they obtained an apparent quantum yield of 6.3% for water splitting with 420 nm monochromatic light.<sup>80</sup> A disadvantage of this approach arises from light absorption/scattering from the

suspended particles.<sup>64</sup> There is also a requirement for high concentrations of added redox shuttles, which limits scalability and introduces competitive, nonproductive electron-transfer reactions.

There is real promise for artificial photosynthesis based on semiconductors with possibilities for scale up and use even on a global scale. This approach relies on light absorption and exciton formation in a semiconductor material followed by efficient electron ( $e^-$ )/hole ( $h^+$ ) pair separation and transport to reactive interfaces. In the absence of traps and impurities, exciton formation can be highly efficient, but  $e^-/h^+$  pair separation is typically inefficient, with recombination<sup>84–88</sup> the limiting factor in dictating device efficiencies.<sup>89–93</sup> Important issues continue to arise from the sometimes competing demands placed on the semiconductor. They arise from maintaining a high efficiency for  $e^-/h^+$  separation while adjusting the band gap of the semiconductor to maximize light absorption and, at the same time, ensuring or maintaining rapid catalytic rates at the interfaces. The systematic approach offered by the application of combinatorial techniques in this area offers real promise.<sup>91,94–99</sup>

### 3. DYE-SENSITIZED PHOTOLELECTROSYNTHESIS CELLS (DSPECS)

#### 3.1. Single-Photoelectrode DSPEC

Shortly after the initial report on UV water splitting at  $\text{TiO}_2$  by Honda and Fujishima,<sup>45</sup> the basis for another approach to water splitting by artificial photosynthesis appeared.<sup>100–105</sup> In acidic solutions of the Ru(II) polypyridyl complex  $\text{Ru}(\text{bpy})_3^{2+}$  and electron-transfer quencher methyl viologen ( $\text{MV}^{2+}$ , Figure 5),

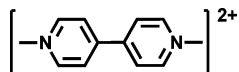
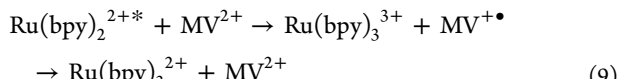
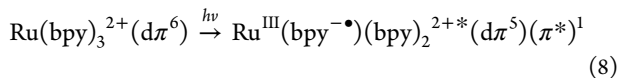


Figure 5. Structure of methyl viologen dication ( $\text{MV}^{2+}$ ).

flash photolysis measurements were used to demonstrate the excitation/electron transfer sequence in eqs 8 and 9. Light absorption by the complex gave the relatively long-lived ( $\mu\text{s}$ ) metal-to-ligand charge transfer (MLCT) excited state  $\text{Ru}(\text{bpy})_3^{2+*}$ , which underwent diffusional oxidative quenching by  $\text{MV}^{2+}$ . The oxidized product,  $\text{Ru}(\text{bpy})_3^{3+}$ , was thermodynamically capable of water oxidation over the entire pH range from pH 0 to pH 14 and  $\text{MV}^+$  of reducing  $\text{H}^+$  to  $\text{H}_2$  in acidic solutions.<sup>100,106–108</sup>



The  $\text{Ru}(\text{bpy})_3^{2+*}$  quenching scheme demonstrated that molecular-level light absorption coupled to electron transfer could be used to produce transiently stored redox equivalents. How to couple  $\text{Ru}(\text{bpy})_3^{3+}$  with water oxidation was an unknown, since there were no known WOCs. In solution, excitation and quenching was followed by BET, as shown in the second part of eq 9. An architecture had to be devised to use the photo-produced redox equivalents before BET could occur. The use of molecules and molecular-level phenomena was

promising, given the flexibility and relative ease of chemical synthesis to make systematic modifications.

We have pursued a promising hybrid molecular-semiconductor approach based on dye-sensitized photoelectrosynthesis cells (DSPECs). It combines molecular-level light absorption and catalysis by chromophore–catalyst assemblies with stable high-band-gap semiconductor oxides, either n-type ( $\text{TiO}_2$ ,  $\text{SnO}_2$ ,  $\text{ZnO}$ ) or p-type ( $\text{NiO}$ ). As in dye-sensitized solar cells (DSSCs), at an n-type oxide, water splitting in a DSPEC is initiated by light absorption by a surface-bound chromophore. In both cases, light absorption and excited state formation are followed by electron injection into the conduction band of the semiconductor and chromophore oxidation. In a DSSC, injected electrons are transferred to a separate cathode in the presence of a redox carrier couple, typically  $\text{I}_3^-/\text{I}^-$ , creating a photopotential and photocurrent.<sup>93,101,109,110</sup> In a DSPEC for water splitting, injected electrons are used to reduce  $\text{H}^+/\text{H}_2\text{O}$  to  $\text{H}_2$ . Oxidative equivalents are accumulated at the catalyst in a chromophore–catalyst assembly for water oxidation.

Figure 6 shows a schematic illustration of a DSPEC for solar water splitting. It uses a chromophore–catalyst assembly on

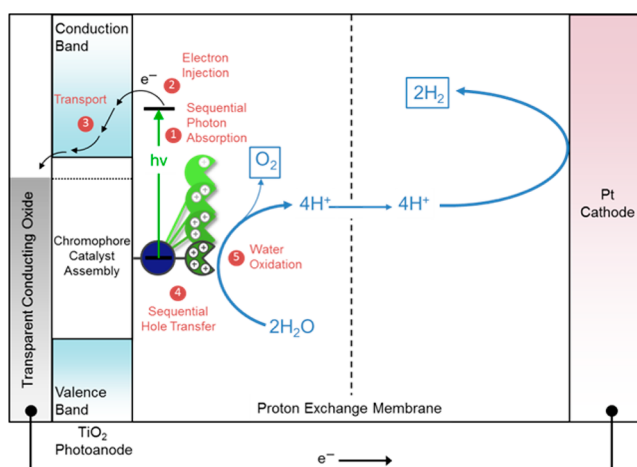


Figure 6. A DSPEC for water splitting into hydrogen and oxygen, illustrating the sequence: (1) chromophore light absorption; (2) excited-state electron injection into the conduction band of the semiconductor; (3) transfer of the injected electron through the semiconductor to a transparent conducting oxide for transfer to the cathode with application of a bias to drive  $\text{H}_2$  production to completion; (4) intra-assembly electron transfer from the catalyst to the chromophore activating the catalyst toward water oxidation; (5) repetition of steps 1–4 four times to drive water oxidation and oxygen evolution at the water oxidation catalyst, followed by  $\text{H}_2\text{O}/\text{H}^+$  reduction to  $\text{H}_2$  at the cathode. Image courtesy of James F. Cahoon.

$\text{TiO}_2$  as the photoanode. Key elements of the DSPEC are (1) a nanostructured, mesoporous n-type semiconductor oxide electrode, transparent in the visible (Vis) region; (2) a near-UV–visible light-harvesting chromophore which, upon excitation, forms an excited state or states which undergo efficient electron injection; (3) a WOC; and (4) a separate cathode where  $\text{H}_2\text{O}/\text{H}^+$  is reduced to  $\text{H}_2$ . Further details are provided in the caption to Figure 6.<sup>42,90,111–115</sup>

In a working DSPEC for water splitting, the photoanode is connected, through an external circuit, to a cathode with a membrane separator to prevent mixing of the gaseous products. In acidic solutions the membrane is permeable to proton diffusion, allowing protons to equilibrate between cell compart-

ments. In operating cells for water splitting based on  $\text{TiO}_2$ , an applied bias is required to maximize photocurrent response and cell efficiency. The applied bias provides the excess potential beyond the conduction-band potential for  $\text{TiO}_2$  to drive  $\text{H}^+/\text{H}_2\text{O}$  reduction to  $\text{H}_2$  to completion.

### 3.2. Tandem DSPEC

**Figure 7** illustrates a tandem DSPEC for the photoelectrochemical reduction of  $\text{CO}_2$  to CO. A similar configuration

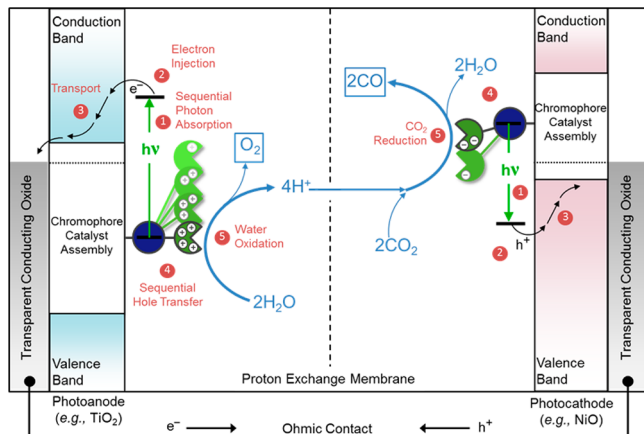
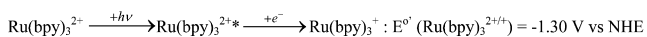
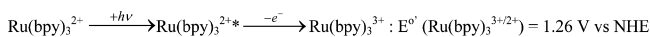


**Figure 7.** Tandem dye-sensitized photoelectrosynthesis cell (DSPEC) for water oxidation and  $\text{CO}_2$  reduction to CO. The sequence of events at the photoanode is the same as described in **Figure 6** with the added photocathode, demonstrating (1) chromophore light absorption; (2) hole injection into the valence band of the semiconductor; (3) transfer of the injected hole through the semiconductor to a transparent conducting oxide for transfer to the anode; (4) intra-assembly electron transfer from the chromophore to the reduction catalyst; (5) reduction of  $\text{CO}_2$  to CO. Image courtesy of James F. Cahoon.

could be used for bias-free water splitting. In a tandem cell two separate photoelectrodes are used, a photoanode for water oxidation, and photocathode for water or  $\text{CO}_2$  reduction. The use of two photons decreases the maximum cell efficiency by a factor of 2, but offers the advantage of greatly increased potentials for driving the integrated half-reactions.

Application of the enhanced driving force provided by a tandem configuration is illustrated for  $\text{Ru}(\text{bpy})_3^{2+*}$  in **Scheme 1**. For a phosphonic acid derivative such as  $[\text{Ru}(4,4'$

#### Scheme 1. Two-Photon Excitation To Give $\text{Ru}(\text{bpy})_3^{3+}$ and $\text{Ru}(\text{bpy})_3^+$



$(\text{PO}_3\text{H}_2)_2\text{bpy})(\text{bpy})_2]^{2+}$  ( $\text{RuP}^{2+}$ ) on an n-type oxide, excitation is followed by electron injection to give a powerful oxidant,  $\text{Ru}(\text{bpy})_3^{3+}$  in **Scheme 1**, with  $E^\circ'(\text{Ru}(\text{bpy})_3^{3+/2+}) = 1.26 \text{ V vs NHE}$ . At the p-type  $\text{NiO}$ , hole injection occurs by electron transfer from the electrode to the excited state to give  $\text{Ru}(\text{bpy})_3^+$ , a powerful reducing agent with  $E^\circ'(\text{Ru}(\text{bpy})_3^{2+/+}) = -1.3 \text{ V}$ .<sup>116–119</sup>

A tandem configuration is needed to drive water reduction of  $\text{CO}_2$  to CO to completion with  $E^\circ'(\text{CO}_2/\text{CO}) = -0.12 \text{ V}$  (vs NHE) and  $E_{\text{CB}}(\text{TiO}_2) \approx -0.1 \text{ V}$  at pH 0.<sup>120–123</sup> The development of photocathodes for water or  $\text{CO}_2$  reduction

has been limited heretofore by the lack of suitable p-type semiconductors with appropriate properties—valence band potential, long-term stability in aqueous solutions, favorable interfacial and intrafilm electron transport properties, optical transparency, and availability of nanoparticle mesoscopic films.<sup>124,125</sup> The most commonly investigated oxide has been  $\text{NiO}$ , although it suffers from slow hole transport and unfavorable interfacial kinetics. The absence of a suitable p-type oxide has greatly limited progress in implementing p-type DSSCs and DSPECs.<sup>126–133</sup> n-type photoanodes are far more advanced, and molecular assembly structures for water splitting applications will be emphasized in this Review.

### 3.3. Chromophore–Catalyst Assemblies

At the heart of a DSPEC is a chromophore–catalyst assembly. On high-band-gap oxides, the assembly or assembly components separately bound to the surface function as both light absorber and catalyst. Important characteristics for useful assemblies are summarized in **Figure 8**. They include (1) stable surface binding to the oxide electrode surface, which also provides an electronic orbital coupling pathway for electron transfer to occur; (2) a light-harvesting chromophore or chromophores that absorb light broadly throughout the near-UV and Vis and, upon excitation, undergo injection into the conduction band of the oxide [at a photocathode, the sense of the injection is reversed, with electron transfer occurring from the conduction band of the oxide to the excited state, net hole transfer from the excited state to the oxide]; (3) a bridging ligand, or other strategy for co-surface integration of a WOC; at a photocathode a catalyst for water reduction to  $\text{H}_2$  or  $\text{CO}_2$  reduction to CO; and (4) a stable, robust, WOC, or catalysts for water or  $\text{CO}_2$  reduction, capable of catalytic rates that significantly exceed the rate of solar insolation, of  $\sim 2 \text{ s}^{-1}/\text{assembly}$  with ambient sun light, see below. A working DSPEC for water splitting also includes the oxide semiconductor, an optically transparent conducting electrode for transferring electrons between cell compartments, and a membrane separator for separating gaseous products while providing for pH equilibration between cell compartments. In a final cell design, a zero gap configuration would be used to minimize the distance of proton migration and to minimize resistive losses from ion diffusion.

The emphasis in this Review is on assemblies for photoanode applications with water oxidation as the primary target. The evolution of strategies for photocathodes is less well-developed, largely because of a dearth of useful p-type oxide materials.  $\text{NiO}$  is the most commonly studied oxide but suffers from unfavorable interfacial electron-transfer kinetics and slow hole transport.

### 3.4. The Oxide Semiconductor

For optical transparency in the Vis, the semiconductor oxide bandgap should be  $\geq 3.2 \text{ eV}$ . At a photoanode, the conduction-band potential must be sufficient to accept an electron from the excited state. As a reference, for the excited state  $\text{Ru}(\text{bpy})_3^{2+*}$ ,  $E^\circ'(\text{Ru}(\text{bpy})_3^{3+}/\text{Ru}(\text{bpy})_3^{2+*}) = -0.8 \text{ V vs NHE}$ .<sup>93,116,117</sup> With  $E_{\text{CB}} = -0.1 \text{ V}$  (vs NHE) for  $\text{TiO}_2$  and  $\sim 0.28 \text{ V}$  for  $\text{SnO}_2$  at pH 0,<sup>93,114,116,134</sup> injection into  $\text{TiO}_2$  by  $\text{Ru}(\text{bpy})_3^{2+*}$  at pH 0 is favored by  $\sim 0.6 \text{ V}$  and into  $\text{SnO}_2$  by  $\sim 1.0 \text{ V}$ . Injection efficiencies,  $\eta_{\text{inj}}$ , of  $\sim 1$  have been reported for  $[\text{Ru}(4,4'-(\text{PO}_3\text{H}_2)_2\text{bpy})(\text{bpy})_2]^{2+*}$  on both oxides.<sup>93,114,116,134–138</sup>

With  $\text{TiO}_2$ , an applied bias of  $\sim 0.2 \text{ V}$  is required to drive  $\text{H}^+/\text{H}_2\text{O}$  reduction to  $\text{H}_2$  to completion and maximize water splitting. The conduction-band potential for  $\text{SnO}_2$  is more

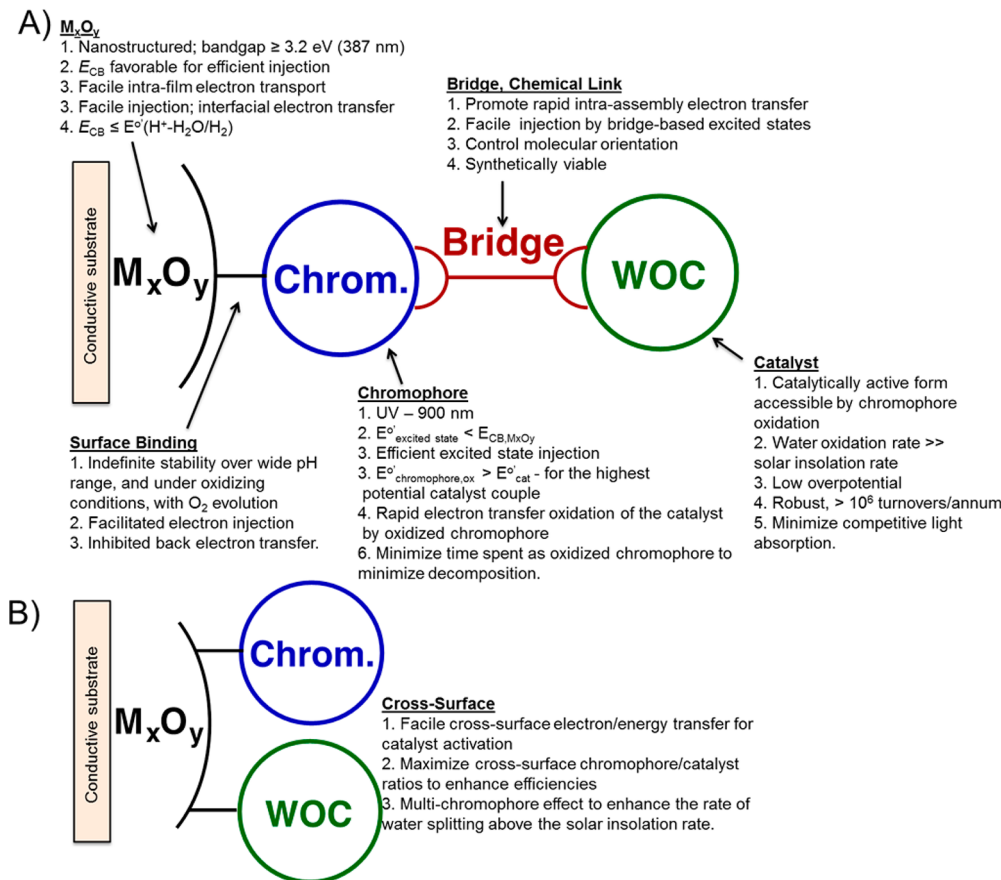


**Figure 8.** Design principles for (A) a covalently linked DSPEC chromophore–catalyst assembly and (B) a co-loaded assembly.

positive by  $\sim 0.3$  V, requiring a higher bias.  $SrTiO_3$ , with  $E_{CB}$  more negative than  $E_{CB}(TiO_2)$  by  $\sim 0.2$  V, is capable of bias-free, water splitting with the semiconductor as the light absorber, but is limited to high-energy photons.<sup>139,140</sup>  $Nb_2O_5$  was initially reported to have a conduction-band potential comparable to that of  $SrTiO_3$ , but a recent re-evaluation showed that its conduction band was slightly more positive than for  $TiO_2$ .<sup>141</sup>  $TiO_2$  and  $SnO_2$  are the two most commonly used metal oxides for photoanodes due to their low conduction-band potentials, ease of synthesis, and stability. Other metal oxides under investigation include  $WO_3$ ,<sup>142,143</sup>  $ZnO$ ,<sup>144,145</sup>  $Nb_2O_5$ ,<sup>141,146</sup>  $Zn_2SnO_4$ ,<sup>147</sup> and  $SrTiO_3$ .<sup>148,149</sup> Multiple tandem approaches are currently under investigation for carrying out bias-free water splitting and  $CO_2$  reduction.

**3.4.1. Surface Attachment and Stabilization.** A variety of strategies for surface binding to oxide surfaces have been investigated. They include surface bonding as alkoxides,<sup>150</sup> hydroxamates,<sup>151</sup> siloxanes,<sup>152</sup> and acetylacetones.<sup>153</sup> By far the most widely used strategies have been surface ester formation by carboxylic acid ( $-CO_2H$ ) and phosphonic acid ( $-PO_3H_2$ ) derivatives. Carboxylate–surface bonding has been used routinely in DSSC applications in nonaqueous solvents but typically suffers from instability toward hydrolysis from the surface in water. Siloxane–surface bonding gives hydrolytically stable surfaces, but silyl precursors are reactive and integrating them into the synthesis of complex chromophore–catalyst assemblies is typically formidable.

Phosphonate–surface binding is far more robust than carboxylate binding but, typically, subject to hydrolysis from the surface at  $pH > 5$  with added buffer bases.<sup>136,154,155</sup>

Instability as the pH is increased is problematic since the potential for water oxidation is decreased to 0.82 V at pH 7 and to 0.40 V at pH 14, with water oxidation becoming more accessible to lower potential oxidants. As noted below, there is also a mechanistic advantage with relatively high concentrations of added buffer bases. It arises from the intervention of the atom–proton transfer (APT) mechanism (shown below in Figure 14), with O---O bond formation occurring in concert with proton loss to the added acceptor bases, which can lead to significant rate accelerations.

Atomic layer deposition (ALD) has been used to stabilize phosphonate-derivatized chromophores, catalysts, and assemblies for applications in water oxidation catalysis and DSPEC water splitting.<sup>156–163</sup> A reactive precursor in the gas phase— $Al(CH_3)_3$  for  $Al_2O_3$ ,  $TiCl_4$  for  $TiO_2$ —is allowed to react with acidic  $-OH$  groups on the oxide surface. Following a hydrolysis step, layers or sublayers of the oxide form on the surface. Sequential gas phase–surface reaction–hydrolysis cycles are used to build-up multi-layers of the oxide on the surface. Figure 8 illustrates surface stabilization of the WOC [ $Ru(Mebimpy)-(4,4'-(PO_3H_2)_2bpy)(OH_2)]^{2+}$  (Mebimpy = 2,6-bis(1-methyl-1*H*-benzo[*d*]imidazol-2-yl)pyridine, 4,4'-( $PO_3H_2$ )<sub>2</sub>-bpy = ([2,2'-bipyridine]-4,4'-diylbis(methylene))diphosphonic acid). At pH 11 with added  $PO_4^{3-}$  and surface stabilization by an overlayer of  $TiO_2$ , it undergoes water oxidation with a turnover rate of  $\sim 10^4$  s<sup>-1</sup>, Figure 9.

Other surface stabilization strategies are being explored, including deposition of an overlayer polymer film of poly(methyl methacrylate) (PMMA).<sup>164</sup> In this strategy, an oxide film with a pre-surface-bound molecule or assembly is dipped

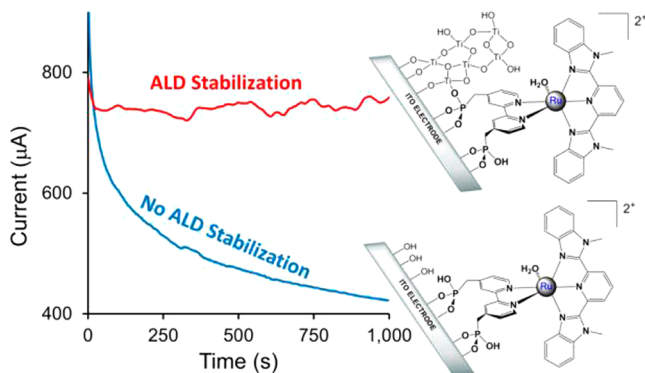


**Figure 9.** Water oxidation catalysis by surface-bound  $[\text{Ru}(\text{Mebimpy})-(4,4'-(\text{PO}_3\text{H}_2)_2\text{-bpy})(\text{OH}_2)]^{2+}$  at pH 11 on an oxide electrode surface protected by an ALD overlayer of  $\text{Al}_2\text{O}_3$  in a 0.1 M phosphate solution at an applied potential of 1.4 V vs NHE. Reprinted from ref 159 with permission from the National Academy of Science.

into a solution containing PMMA. With removal of the film, a conformal surface layer is formed, with the thickness controllable by varying the concentration of PMMA in the solution. The added hydrophobic polymer overlayer imparts surface stability over a wide pH range.

Figure 10 illustrates an electropolymerization strategy based on prior surface binding of a polypyridyl complex co-derivatized with phosphonic acid and 5,5'-vinyl-2,2'-bipyridine ligands on metal oxide electrodes.<sup>165–167</sup> CV scans to negative potentials result in reduction at  $\pi^*(\text{bpy})$  levels on the ligands. In solutions containing a vinyl-bpy derivative of a water oxidation catalyst, ligand-based reduction results in vinyl radical C–C coupling and surface assembly formation.

### 3.5. Light Absorption

Maximizing light absorption in a DSPEC device is desirable, but the range of useful light absorption is dictated by the redox potentials of the excited state, the potentials of the target half-reactions, and the conduction or valence band potentials of the oxide.<sup>93,114,116,134</sup> The energy content for 700 nm light is 1.77 eV, and that for 800 nm light is 1.55 eV. The latter approaches the  $\Delta G^\circ = 1.23$  eV/redox equivalent limit for water splitting into  $\text{H}_2$  and  $\text{O}_2$ . The water splitting threshold is 1008 nm, with four photons required. One-electron oxidation to the hydroxyl radical,  $\cdot\text{OH} + \text{H}^+ + \text{e}^- \rightarrow \text{H}_2\text{O}$ , occurs at  $E^\circ \approx 2.4$  V vs NHE (at pH 7), for which the energy threshold is  $\lambda \leq 516$  nm.<sup>42,168</sup> Because of the high energy of the hydroxyl radical, water oxidation with low-energy Vis light requires multiple photons to activate and use multi-electron pathways which avoid high-energy intermediates.

In the absence of a solar concentrator, the output of a DSPEC is limited by the rate of solar insolation. In a standard AM 1.5G solar flux, a typical dye molecule that is  $\sim 1$  nm wide

and has a molar absorptivity of  $2 \times 10^4 \text{ M}^{-1} \text{ cm}^{-1}$  is able to absorb only  $\sim 2$  photons per second in the Vis and near-infrared (IR) and only  $\sim 0.3$  photon in the UV.<sup>109,169–171</sup> Broad light absorption is desirable, ideally from the near-UV throughout the Vis into the near-IR, subject to the energy constraints of the reaction and of the device. Maximized molecular absorptivity is desirable as a way to minimize film thickness. In thinner films, the average distance from the site of injection through the film is minimized, which decreases losses from BET, Section 7.

The excited state or states reached by light absorption must be thermodynamically capable of injecting an electron into the conduction band of an n-type oxide, e.g.,  $\text{TiO}_2$ ,  $\text{SnO}_2$ , etc., or of accepting an electron from the valence band of a p-type oxide, such as  $\text{NiO}$ . Following electron injection, the oxidized chromophore must be thermodynamically capable of driving water oxidation at an electronically linked catalyst for water oxidation or, with hole injection, of driving a catalyst for water or  $\text{CO}_2$  reduction.

To date, DSPEC studies have been dominated by Ru(II) polypyridyl chromophores. As shown by the spectrum of  $[\text{Ru}(\text{bpy})_3]^{2+}$  in Figure 11, they typically absorb light with

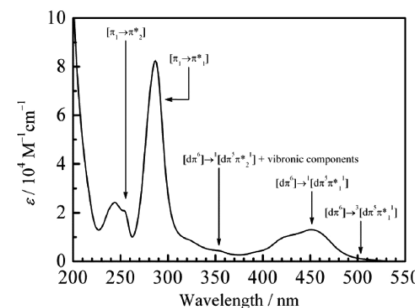
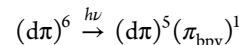
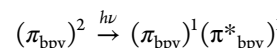


**Figure 11.** (A) UV–visible spectrum of  $[\text{Ru}(\text{bpy})_3]^{2+}$  in MeCN, including spectral assignments. Reprinted with permission from ref 117. Copyright 2014 International Union of Pure and Applied Chemistry.

relatively high absorptivities throughout the near-UV and Vis. Visible absorption bands arise from MLCT transitions with electronic excitation from  $d\pi$  orbitals on the metal to  $\pi^*$  acceptor levels on the polypyridyl ligands,



UV absorption is dominated by ligand-based transitions,



These complexes have significant advantages as chromophores. The background synthetic chemistry is well-developed,<sup>109,115–117,119,171,172</sup> and polypyridyl complexes of Ru(II)

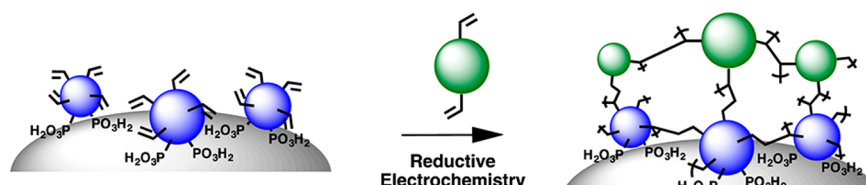


**Figure 10.** Electro-assembly formation at the vinyl-derivatized, surface-bound phosphonate chromophore  $[\text{Ru}(\text{dvb})_2((\text{PO}_3\text{H}_2)_2\text{bpy})]^{2+}$  ( $\text{dvb} = 5,5'$ -divinyl-2,2'-bipyridine;  $(\text{PO}_3\text{H}_2)_2\text{bpy} = [\text{2},\text{2}'\text{-bipyridine}]\text{-4},\text{4}'\text{-diylbis(phosphonic acid)}$ ) by reductive vinyl C–C coupling with the water oxidation catalyst.<sup>165–167</sup> Reprinted with permission from ref 167. Copyright 2014 American Chemical Society.

are typically coordinatively stable. Light absorption and excited-state structure and reactivity are well-understood.<sup>107,109,117,173–176</sup> There is also a well-developed, parallel Os(II) polypyridyl chemistry, but the synthetic chemistry is more demanding, given the inertia to substitution at Os(II), and the fact that, as a third-row transition metal, Os is “non-Earth-abundant”.<sup>117</sup>

Ru(II)–polypyridyl complexes can be disadvantaged as chromophores by limited absorptivity in the Vis and near-IR. This point is illustrated by the spectrum of Ru(bpy)<sub>3</sub><sup>2+</sup> in CH<sub>3</sub>CN in Figure 11. The molar absorptivity at the visible maximum wavelength ( $\lambda_{\text{max}}$ ), 449 nm, is only  $1.4 \times 10^4 \text{ M}^{-1} \text{ cm}^{-1}$ , which decreases to  $5.1 \times 10^2 \text{ M}^{-1} \text{ cm}^{-1}$  by 550 nm, limiting useful absorptivity to  $\lambda < 550 \text{ nm}$ . Given the orbital nature of the ground and excited states, light absorption can be manipulated systematically by varying the ligands. This approach has been used to prepare “black MLCT absorbers” that absorb light throughout the near-UV–Vis and into the near-IR.<sup>177</sup>

In practical DSPEC applications, the use of inexpensive organic dyes and first-row transition metal complex catalysts for water oxidation is clearly desirable, based on cost and abundance. In DSSC applications, other custom-designed chromophores are playing increasingly important roles as light absorbers, extending light absorption into the near-IR, leading to solar efficiencies well above 12%, with recent examples as high as 18.4% for perovskites.<sup>178–181</sup> In these applications, organic solvents, typically acetonitrile, are used in which transient organic cation radicals reasonable stabilities.

The use of these dyes for water splitting in water as solvent is problematic, given the instability of the radical cations. In PSII, antenna sensitization of the lowest singlet excited state of the penultimate chromophore, cytochrome P<sub>680</sub>, is followed by oxidative quenching to give P<sub>680</sub><sup>+</sup>. Although the chlorophyll radical cation is formed in the partly aqueous environment surrounding the reaction center, it is short-lived, undergoing rapid electron-transfer reduction by an adjacent phenol, Tyrosine<sub>Z</sub>. The Tyr<sub>Z</sub>O<sup>•</sup>–H-His(190) PCET couple subsequently oxidizes the Mn<sub>4</sub>Ca cluster in the oxygen evolving complex (OEC), where O<sub>2</sub> is evolved.<sup>21,38,182–185</sup>

### 3.6. Excited-State Potentials

**3.6.1. Electron Injection.** Light-induced electron injection at the chromophore–semiconductor interface is a complex process that can occur through either direct or multi-step mechanisms. Examples of direct injection, with photon absorption promoting an electron directly from the ground state of an adsorbed dye into the conduction band of the semiconductor, have been reported.<sup>186–190</sup> However, injection is typically dominated by excitation of a chromophore followed by electron injection from the excited-state intermediate. A theory of interfacial electron transfer was developed by Gerischer based on classical Marcus–Hush electron-transfer theory.<sup>186,187,18,19,22,23</sup> Equation 10, which comes from this

$$k_{\text{inj}} = \frac{2\pi}{\hbar} \int_{-\infty}^{\infty} g(E)(1 - f(E, E_F))|H_{\text{ab}}(E)|^2 W(E) \text{ d}E \quad (10)$$

theory, provides an expression for the injection rate constant,  $k_{\text{inj}}$ , in terms of  $g(E)$ , the distribution of acceptor levels in the oxide as a function of energy ( $E$ );  $f(E, E_F)$ , the Fermi function which gives the occupancy of levels at energy  $E$ ;  $H_{\text{ab}}(E)$ , the

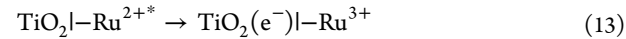
electron-transfer coupling matrix element; and  $W(E)$ , the distribution function describing the variation of the classical free energy of activation with free energy change  $\Delta G(E)$  and reorganization energy  $\lambda$ . From Marcus–Hush theory in the classical, harmonic limit,  $W(E)$  is given by eq 11. The

$$W(E) = \frac{1}{\sqrt{4\pi\lambda k_B T}} \exp\left(\frac{-(\Delta G(E) + \lambda)^2}{4\lambda k_B T}\right) \quad (11)$$

reorganization energy is the sum of intramolecular ( $\lambda_i$ ) and medium ( $\lambda_o$ ) reorganization energies.  $\Delta G(E)$  is related to the potentials for the acceptor levels in the conduction band ( $E_{\text{CB}}$ ) and injecting excited state by eq 12. Given the nature of the

$$\Delta G(E) (\text{eV}) = F(E_{\text{CB}} - E^{o'}_{-\text{Ru}^{3+}/-\text{Ru}^{2+*}}) \quad (12)$$

measurement,  $\lambda$  is the reorganization energy for single-site electron transfer on the surface; note the surface-bound  $-\text{Ru}^{3+}/2+*$  couple in eq 13.<sup>100,173,188–193</sup>



The free energy change for injection is given by eq 12, with  $F$  the Faraday constant, 1 eV/V, and  $E^{o'}_{-\text{Ru}^{3+}/-\text{Ru}^{2+*}}$  the excited-state reduction potential. With Ru(bpy)<sub>3</sub><sup>2+\*</sup> as the example, the formal reduction potential for excited-state oxidation, Ru(bpy)<sub>3</sub><sup>2+\*</sup> – e<sup>–</sup> → Ru(bpy)<sub>3</sub><sup>3+</sup>,  $E^{o'}(\text{Ru(bpy)}_3^{3+/2+*})$ , is given by eq 14, with  $\Delta G_{\text{ES}}$  the free energy of the excited state above the

$$E^{o'}(\text{Ru(bpy)}_3^{3+/2+*}) = E^{o'}(\text{Ru(bpy)}_3^{3+/2+}) - \Delta G_{\text{ES}} \quad (14)$$

ground state. Similarly, the reduction potential for the excited state as an oxidant, Ru(bpy)<sub>3</sub><sup>2+\*</sup> + e<sup>–</sup> → Ru(bpy)<sub>3</sub><sup>+</sup>, is given by eq 15.  $\Delta G_{\text{ES}}$  can be evaluated by a Franck–Condon analysis of

$$E^{o'}(\text{Ru(bpy)}_3^{2+*/+}) = E^{o'}(\text{Ru(bpy)}_3^{2+/+}) + \Delta G_{\text{ES}} \quad (15)$$

emission spectral profiles<sup>116,171,194–196</sup> or estimated from  $E_{0-0}$ , the energy of the 0–0 transition between the lowest vibrational levels ( $v = 0$ ) of the ground and excited states. It is also approximated as the normalized intersection between emission and absorption spectra but subject to significant error.<sup>109,117,197–199</sup>

As noted above, and as illustrated in Figure 12, the reduction potential for the lowest <sup>3</sup>MLCT excited state for surface-bound [Ru(4,4'-(PO<sub>3</sub>H<sub>2</sub>)<sub>2</sub>bpy)(bpy)<sub>2</sub>]<sup>2+</sup> (–RuP<sup>2+</sup>, with bpy = 2,2'-bipyridine) is ~–0.8 V vs NHE,<sup>135,136,154</sup> and injection by –RuP<sup>2+\*</sup> in acidic solution occurs with an efficiency of ~1.<sup>135,136,154</sup>

Based on the results of ultrafast transient absorption (TA) spectroscopy measurements on –RuP<sup>2+\*</sup> and related Ru(II)–polypyridyl complexes, injection is kinetically complex.<sup>109,169,171,173,200</sup> An injection scheme in 0.1 M HClO<sub>4</sub> is shown in Figure 13. An initial injection process or processes occurs on the time scale of hundreds of femtoseconds to hundreds of picoseconds. On this time scale, injection occurs from the initial MLCT singlet state(s), TiO<sub>2</sub>|–{[(4,4'-(PO<sub>3</sub>H<sub>2</sub>)<sub>2</sub>bpy)<sup>–</sup>]Ru<sup>III</sup>(bpy)<sub>2</sub>]<sup>2+\*</sup>}, before <sup>1</sup>MLCT → <sup>3</sup>MLCT internal conversion can occur. A second contribution comes

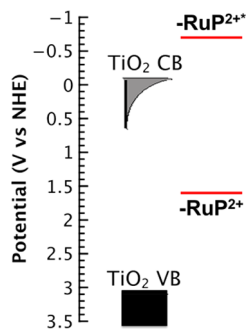


**Figure 12.** Potential diagram for injection into the conduction band of  $\text{TiO}_2$  by the MLCT excited state(s) of surface-bound  $[\text{Ru}(4,4'-(\text{PO}_3\text{H}_2)_2\text{bpy})(\text{bpy})]^{2+}$  ( $-\text{RuP}^{2+}$ ) at pH 0 in aqueous solution at room temperature. CB and VB are labels for the conduction and valence bands, respectively. A distribution of trap states lying below the CB is also illustrated.

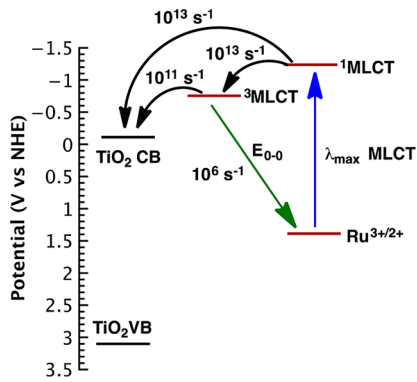


**Figure 13.** Potential diagram for  $\text{TiO}_2\text{|}-\text{RuP}^{2+}$ , illustrating the conduction band (CB) and valence band (VB) of  $\text{TiO}_2$  and MLCT excited-state injection in 0.1 M  $\text{HCO}_4$  at room temperature.

from the lowest triplet state before it undergoes vibrational relaxation.<sup>196,201–204</sup>

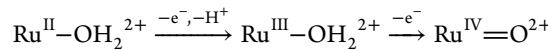
### 3.7. Water Oxidation

In the semiconductor-based PEC cells discussed in Section 2, water oxidation catalysis occurs at metal oxides—as  $\text{RuO}_2$  nanoparticles,  $\text{CoO}_x$  films, etc.—and mechanistic insight is limited.<sup>43,205–211</sup> Water oxidation by molecular catalysis in a DSPEC offers the advantage that the catalyst can be modified by chemical synthesis with a variety of experimental techniques available for monitoring rates and mechanisms. The first designed molecular catalyst for water oxidation was the Ru(III) “blue dimer”, *cis,cis*-[(bpy)<sub>2</sub>( $\text{H}_2\text{O}$ )Ru<sup>III</sup>O $\text{Ru}^{\text{III}}(\text{OH}_2)$ (bpy)<sub>2</sub>]<sup>4+</sup> (note the structure shown in Figure 32).<sup>42,212,213</sup> It undergoes PCET activation to give  $[(\text{bpy})_2(\text{O})\text{Ru}^{\text{V}}\text{ORu}^{\text{V}}(\text{O})(\text{bpy})_2]^{4+}$  as a kinetic transient, followed by rapid O-atom transfer to a water molecule to give the intermediate peroxide,  $[(\text{bpy})_2(\text{O})\text{Ru}^{\text{V}}\text{O}\text{-Ru}^{\text{III}}(\text{OOH})(\text{bpy})_2]^{4+}$ . The peroxide intermediate undergoes further oxidation and  $\text{O}_2$  release, returning the complex to the water oxidation cycle.<sup>168,214</sup> Water oxidation catalysis by the blue dimer is inhibited by anion capture which accompanies  $\text{O}_2$  release.<sup>42,214–216</sup>

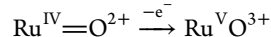
The detailed mechanistic insight gained from the blue dimer, and the conclusion that O---O bond formation occurs between a single  $\text{Ru}^{\text{V}}(\text{O})$  site and an external water molecule, led to the successful design of a family of single-site Ru(II)–polypyridyl catalysts.<sup>34,35,168,217,218</sup> Single-site catalysis had first been reported by Thummel and co-workers.<sup>219</sup> Kinetic and

mechanistic studies on Ru(II)–polypyridyl–aqua complexes based on Ce(IV) as the oxidant in acidic solution, and electrochemical measurements over an extended pH range, have provided detailed mechanistic insight.<sup>34,35,220</sup> Single-site catalysis by Ru(II)–polypyridyl complexes has been extended to oxide electrodes by using phosphonic acid-derivatized complexes and assemblies.<sup>216,221</sup>

Many single-site catalysts have been reported, including examples of Ru(II),<sup>33,222–227</sup> Ir(III),<sup>228–233</sup> Co(III),<sup>234,235</sup> Cu(II),<sup>236</sup> and Fe(II),<sup>237–239</sup> with reviews in the recent literature.<sup>227,240–243</sup> Mechanistic information is available for complexes of Ir(III),<sup>228,229,244,245</sup> Co(III),<sup>234,235,246,247</sup> Cu(II),<sup>236,248,249</sup> and Fe(II),<sup>237,239,250</sup> with especially detailed insight available for polypyridyl complexes of Ru(II).<sup>35,42,168,222,223,251–254</sup> A generic mechanism for aqua-based complexes is illustrated for the solution-based catalyst  $[\text{Ru}(\text{Mebimpy})(\text{bpy})(\text{OH}_2)]^{2+}$  ( $\text{Ru}^{\text{II}}\text{-OH}_2^{2+}$ ) in Figure 9.<sup>33–35</sup> It features sequential oxidative activation,



by PCET, which, with combined  $\text{e}^-/\text{H}^+$  loss, avoids charge buildup, enabling multiple oxidative equivalents to accumulate at single sites or clusters at accessible redox potentials.<sup>38–41,251</sup> Further  $1\text{e}^-$  oxidation occurs to give  $\text{Ru}^{\text{V}}(\text{O})^{3+}$ ,



The resulting high-oxidation-state oxo complexes have a well-established reactivity based on concerted electron–proton transfer (EPT), H-atom transfer, C–H insertion, hydride transfer, and O-atom transfer, with the latter a key step in the water oxidation mechanism in Figure 14.<sup>32–35,42,219,227,255,256</sup>

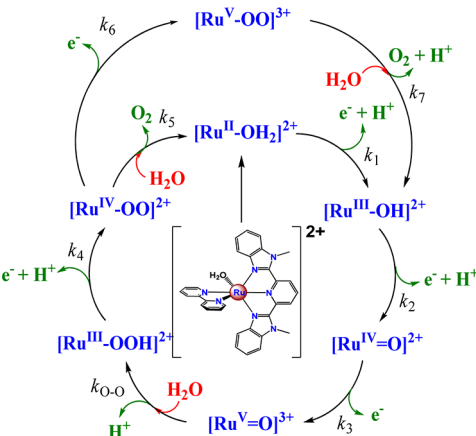
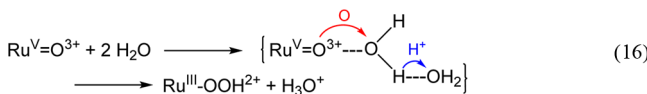


**Figure 14.** Mechanism of water oxidation by the single-site water oxidation catalyst  $[\text{Ru}(\text{Mebimpy})(\text{bpy})(\text{OH}_2)]^{2+}$ . Reprinted with permission from ref 34. Copyright 2008 American Chemical Society.

For  $[\text{Ru}(\text{Mebimpy})(\text{bpy})(\text{OH}_2)]^{2+}$ , rate-limiting O---O bond formation occurs following  $3\text{e}^-/2\text{H}^+$  oxidation of  $\text{d}\pi^6 \text{Ru}^{\text{II}}\text{-OH}_2^{2+}$  to  $\text{d}\pi^3 \text{Ru}^{\text{V}}(\text{O})^{3+}$ . O---O bond formation occurs by O-atom transfer to a water molecule to give the intermediate hydroperoxide,  $\text{Ru}^{\text{III}}\text{-OOH}^{2+}$ , followed by further oxidation and  $\text{O}_2$  loss through a  $\text{Ru}^{\text{IV}}(\text{OO})^{2+}$  peroxide intermediate, Figure 14.  $\text{Ru}^{\text{IV}}(\text{OO})^{2+}$  intermediates have been detected in water oxidation cycles in solution and on oxide surfaces. They undergo  $\text{O}_2$  loss, re-entering the catalytic cycle as  $\text{Ru}^{\text{II}}\text{-OH}_2^{2+}$ , which can be slow. Further oxidation to  $\text{Ru}^{\text{V}}(\text{OO})^{3+}$  results in

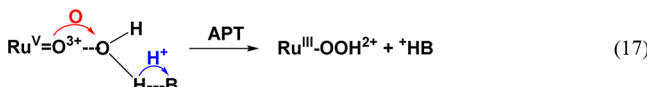
rapid loss of O<sub>2</sub>, returning the complex to the catalytic cycle as Ru<sup>III</sup>—OH<sup>3+</sup> or Ru<sup>III</sup>—OH<sup>2+</sup>, depending on the pH.<sup>35,42,217,257</sup>

**3.7.1. Atom-Proton Transfer (APT).** In most catalytic cycles, the rate-limiting step is O-atom transfer with O---O bond formation. Based on the results of DFT calculations and the observation of a H<sub>2</sub>O/D<sub>2</sub>O kinetic isotope effect of 6.6 for water oxidation by [Ru<sup>V</sup>(tpy)(bpm)(O)]<sup>3+</sup> (tpy = terpyridine, bpm = 2,2'-bipyrimidine), O---O bond formation has been proposed to occur in concert with proton loss to a H-bonded water molecule or cluster, eq 16, by the microscopic APT

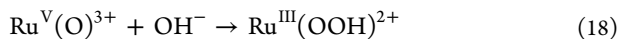


pathway.<sup>258</sup> APT has the advantage of forming the hydroperoxide intermediate directly. It avoids the higher energy hydrogen peroxide intermediate,  $\text{Ru}^{\text{III}}(\text{OOH}_2)^{3+}$ , formed by direct reaction with water,  $\text{Ru}^{\text{V}}(\text{O})^{3+} + \text{H}_2\text{O} \rightarrow \text{Ru}^{\text{III}}(\text{OOH})^{3+}$ .

Because APT and O---O bond formation are rate-limiting, addition of buffer bases leads to significant rate enhancements, with the added base acting as the proton acceptor, eq 17. The



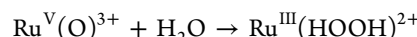
extent of the rate enhancement depends on the concentration of added base (B) and its base strength, as measured by the  $pK_a$  of the conjugate acid ( $\text{HB}^+$ ). With added buffer bases, terms appear in the rate law for water oxidation that are first-order in added base,  $k_B[B]$ . For  $[\text{Ru}^\text{V}(\text{Mebimpy})(\text{bpy})(\text{O})]^{3+}$  as the oxidant,  $k_B = 3.8 \pm 0.5$ ,  $10.3 \pm 1$ , and  $48 \pm 5 \text{ M}^{-1} \text{ s}^{-1}$  for  $\text{H}_2\text{PO}_4^-$  ( $pK_a(\text{H}_3\text{PO}_4) = 2.15$ ),  $\text{OAc}^-$  ( $pK_a(\text{HOAc}) = 4.75$ ), and  $48 \pm 5$  for  $\text{HPO}_4^{2-}$  ( $pK_a(\text{HPO}_4^{2-}) = 7.20$ ). At high concentrations of added base, rate accelerations of up to  $10^4$  are observed. At even higher pH, with the concentration of  $\text{OH}^-$  kinetically significant, pathways first-order in  $\text{OH}^-$  appear in the rate law arising from direct O-atom transfer to give the hydroperoxide, eq 18.<sup>159</sup>



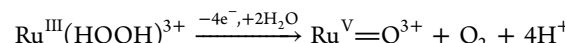
The impact of added bases and APT pathways on reactivity can be significant. The overpotential for water oxidation by  $[\text{Ru}^{\text{IV}}(\text{tpy})(\text{bpz})(\text{O})]^{2+}$  ( $\text{bpz} = 2,2'$ -bipyrazine) is only  $\sim 0.2$  eV over an extended pH range, but, in acidic solutions, water oxidation is too slow to be of interest. With high concentrations of  $\text{PO}_4^{3-}$  added as an APT base, the rate of water oxidation is greatly enhanced. Under these conditions, the observed rate constant,  $k_{\text{obs}}$ , takes the form  $k_{\text{obs}} = k_{\text{H}_2\text{O}} + k_{\text{PO}_4^{3-}} + k_{\text{OH}^-}$ , with separate pathways appearing for direct reactions with  $\text{H}_2\text{O}$  and  $\text{OH}^-$  and APT with  $\text{PO}_4^{3-}$  as the acceptor base ( $k_{\text{PO}_4^{3-}}$ ). At pH 11 in 1 M  $\text{PO}_4^{3-}$ , the half-time for water oxidation by  $\text{Ru}^{\text{IV}}=\text{O}^{2+}$  is 130 ms at an overpotential of only 180 mV. It is also significant that the reactive intermediate in this case,  $[\text{Ru}^{\text{IV}}(\text{tpy})(\text{bpz})(\text{O})]^{2+}$ , is accessible after only two excitation/injection/electron transfer cycles with  $2\text{e}^-/2\text{H}^+$  oxidation of the catalyst, rather than three cycles and  $3\text{e}^-/2\text{H}^+$  oxidation of the catalyst.

**3.7.2. Nonaqueous Solvent.** The molecularity of water as a reagent in water oxidation was investigated in propylene carbonate (PC) as solvent, with water miscible up to 8% by

volume. In PC, water oxidation by  $[\text{Ru}^{\text{V}}(\text{Mebimpy})(\text{bpy})-\text{(O)}]^{\text{3+}}$  was first-order in both  $\text{Ru}^{\text{V}}(\text{O})^{\text{3+}}$  and  $\text{H}_2\text{O}$ , consistent with rate-limiting O-atom transfer from  $\text{Ru}^{\text{V}}(\text{O})^{\text{3+}}$  to water to give a hydrogen peroxide intermediate,



followed by further oxidation and O<sub>2</sub> release



Rate constant comparisons reveal that the rate of water oxidation is enhanced by ~300 in PC compared to H<sub>2</sub>O, with the increase attributed to the greatly decreased solvent stabilization of H<sub>2</sub>O in PC compared to H<sub>2</sub>O in water.<sup>259</sup>

**3.7.3. Sun's bda Catalysts.** Sun and co-workers have demonstrated impressive catalytic rates at relatively low overpotentials for water oxidation by complexes of the type Ru(bda)(L<sub>2</sub>) (bda = 2,2'-bipyridine-6,6'-dicarboxylate, L = picoline, iso-quinoline, or other substituted pyridine), Figure 15.<sup>222,223,254,260</sup> The mechanistic chemistry of these catalysts

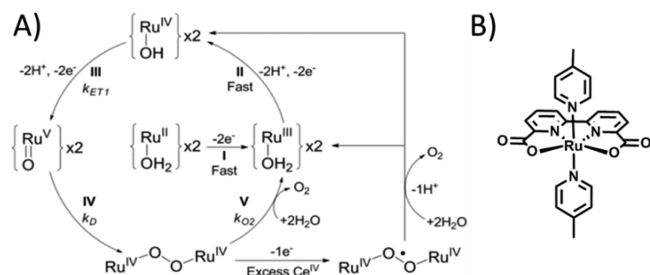


**Figure 15.** (A) Catalytic scheme for Ce(IV) water oxidation catalyzed by Ru(bda)(L<sub>2</sub>). (B) Structure of Ru(bda)(picoline)<sub>2</sub>. Reprinted with permission from ref 222. Copyright 2012 Nature Publishing Group.

continues to evolve, but kinetic measurements in acidic solution with Ce(IV) as oxidant have provided evidence for facile pathways involving oxidation and coordination expansion to seven-coordinate Ru(V)-oxo intermediates, followed by bimolecular O–O coupling and formation of peroxy intermediates. Figure 15 illustrates the structure of Ru(bda)-(picoline)<sub>2</sub> and a kinetic scheme proposed by Sun and co-workers.<sup>222,223,254,260</sup> In a recent report, Concepcion and co-workers have presented evidence for a water oxidation mechanism involving the formation and reactivity of a “blue dimer”-like intermediate in the catalytic cycle.<sup>261</sup>

In another recent study, it was shown that the isoquinoline complex,  $[\text{Ru}^{\text{II}}(\text{bda})(\text{isoq})_2]$ , in aqueous solution 4% by volume of MeCN, exists as the open-arm chelate,  $[\text{Ru}^{\text{II}}(\text{CO}_2\text{-bpy-CO}_2^-)(\text{isoq})_2(\text{NCCH}_3)]$ , with  $\text{pK}_a = 2.4$ , as shown by  $^1\text{H}$  and  $^{13}\text{C}$  NMR spectra, X-ray crystallography, and pH titrations. Rates of water oxidation with the open-arm chelate are remarkably enhanced by APT and added proton acceptor bases. In 1.0 M  $\text{PO}_4^{3-}$ , the calculated half-time for water oxidation was  $\sim 7 \mu\text{s}$ .<sup>262</sup>

**3.7.4. Water Oxidation on Oxide Surfaces.** In a DSPEC application, water oxidation catalysis is integrated with light absorption and excited-state injection on a semiconductor oxide surface. It has been shown that reactivity in solution can be transferred to the surfaces of oxide electrodes by using phosphonic-acid-derivatized chromophores, catalysts, and assemblies with limited impact on reactivity or other properties.<sup>263,264</sup> Figures 9 and 16 illustrate the phosphonate-

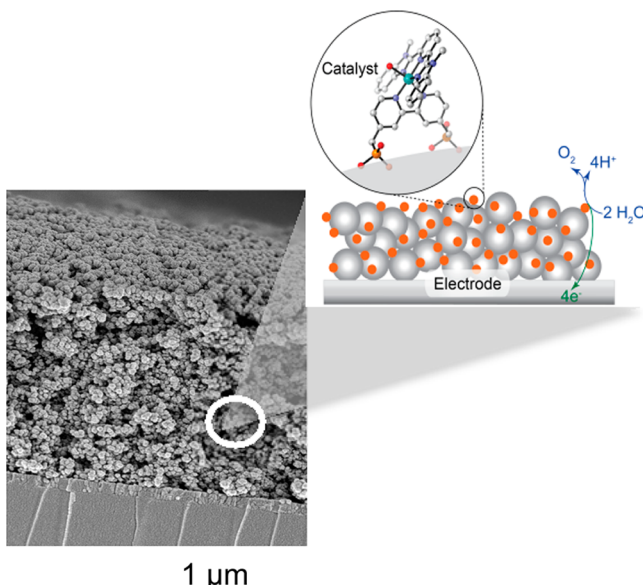


**Figure 16.** Depiction of the water oxidation catalyst  $[\text{Ru}(\text{Mebimpy})(4,4'-(\text{PO}_3\text{H}_2)_2\text{bpy})(\text{OH}_2)]^{2+}$  (Mebimpy = 2,6-bis(1-methylbenzimidazol-2-yl)pyridine; 4,4'-(PO<sub>3</sub>H<sub>2</sub>)<sub>2</sub>bpy = 4,4'-bis-methylene-phosphonato-2,2'-bipyridine) surface-attached to a nanoparticle film of tin-doped indium oxide (Sn:In<sub>2</sub>O<sub>3</sub>).

derivatized catalyst,  $[\text{Ru}(\text{Mebimpy})(4,4'-(\text{PO}_3\text{H}_2)_2\text{bpy})(\text{OH}_2)]^{2+}$ , surface-bound to an optically transparent, mesoscopic nanoparticle film of tin-doped indium oxide (nanoITO). The optical transparency of the conducting oxide allows for spectroelectrochemical monitoring of surface-bound molecules and assemblies, identification of reactive intermediates, and kinetic monitoring. As discussed in Section 3.7.3, in DSPEC applications, surface-bound Ru(bda)(L<sub>2</sub>) catalysts have played a critical role because of the relatively low potentials needed to access Ru<sup>V(O)</sup><sup>3+</sup> and their relatively rapid rates of water oxidation.

**3.7.5. Water Oxidation in Assemblies.** Water oxidation by surface-bound chromophore–catalyst assemblies has also been investigated, initially for the assembly  $[(4,4'-(\text{PO}_3\text{H}_2)_2\text{bpy})_2\text{Ru}^{\text{II}}(\text{bpm})\text{Ru}^{\text{II}}(\text{Mebimpy})(\text{OH}_2)]^{4+}$  (1), Figure 17. In acidic solution it was shown to undergo sustained water oxidation catalysis through 28,000 turnovers without decomposition at a rate of  $0.6 \text{ s}^{-1}$ .<sup>218</sup>

Water oxidation catalysis by the assembly  $[(4,4'-(\text{PO}_3\text{H}_2)_2\text{bpy})_2\text{Ru}(4\text{-Mebpy-4'-bimpy})\text{Ru}(\text{tpy})(\text{OH}_2)]^{4+}$  (18, also called  $[\text{Ru}_a^{\text{II}}-\text{Ru}_b^{\text{II}}-\text{OH}_2]^{4+}$ , where Ru<sub>a</sub><sup>II</sup> refers to the light-harvesting chromophore and Ru<sub>b</sub><sup>II</sup> refers to the WOC in the assembly, see Figure 28 below), surface-bound to nanoITO, has been investigated electrochemically in acidic solution, Section 6.<sup>265</sup> Sequential  $1\text{e}^-/1\text{H}^+$  oxidation of the catalyst in the assembly to  $-\text{Ru}_b^{\text{IV}}=\text{O}^{2+}$  is followed by further oxidation of the chromophore to  $-[\text{Ru}_a^{\text{III}}-\text{Ru}_b^{\text{IV}}=\text{O}]^{5+}$  at 1.36 V. Importantly,  $-[\text{Ru}_a^{\text{III}}-\text{Ru}_b^{\text{IV}}=\text{O}]^{5+}$  undergoes O–O bond formation without having to undergo further oxidation to  $-[\text{Ru}_a^{\text{III}}-\text{Ru}_b^{\text{V(O)}}]^{6+}$  at 1.6 V. In this assembly,  $3\text{e}^-/2\text{H}^+$  activation is distributed between chromophore and catalyst, and the suggestion has been made that rate-limiting O–O bond formation occurs by O-atom transfer to an external water molecule in concert with single-electron transfer to both  $-\text{Ru}_a^{\text{III}}$  and  $-\text{Ru}_b^{\text{IV}}=\text{O}$ , a pathway described as electron–atom–proton transfer (EAPT).

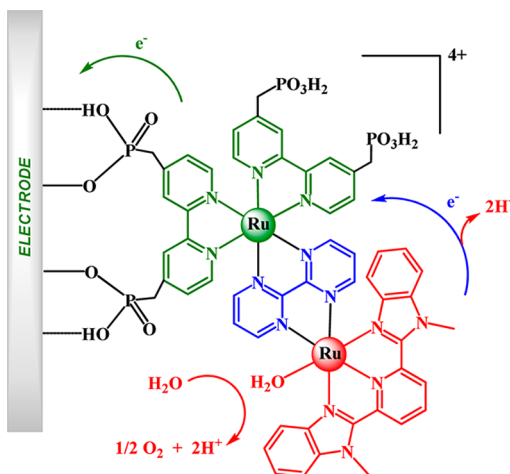


**Figure 17.** Structure of  $[(4,4'-(\text{PO}_3\text{H}_2)_2\text{bpy})_2\text{Ru}^{\text{II}}(\text{bpm})\text{Ru}^{\text{II}}\text{-}(\text{Mebimpy})(\text{OH}_2)]^{4+}$ . Reprinted with permission from ref 218. Copyright 2009 Wiley-VCH Verlag GmbH & Co.

**3.7.6. Rates.** Water oxidation catalysis continues to evolve with the twin goals of achieving higher rates and greater long-term stability while avoiding competitive, nonproductive light absorption.<sup>24,266–269</sup> To put rate into perspective, in ambient sunlight the rate of solar insolation per chromophore in the Vis is  $\sim 2 \text{ s}^{-1}$ . Since water oxidation requires four photons, the theoretical maximum rate of water oxidation is  $\sim 0.5 \text{ s}^{-1}$  without solar concentration. In order to avoid losses in efficiency or stability due to slow water oxidation, it is desirable for the slowest step in the water oxidation cycle to be significantly more rapid, at least by a factor of 10, to avoid losses from BET and decomposition of the oxidized chromophore.

With a solar concentrator the demands on rate are even higher. Solar-driven water oxidation occurs in PSII in natural photosynthesis. PSII uses an “antenna” of hundreds of coupled chromophores consisting of chlorophyll and auxiliary pigments. They absorb light and funnel it rapidly and efficiently to a single chlorophyll acceptor site, P<sub>680</sub>, in the Reaction Center where water oxidation occurs at a Mn<sub>4</sub>Ca cluster in the OEC.<sup>21,183–185</sup> The antenna effect concentrates the solar input from multiple chromophores increasing the effective rate of solar insolation from seconds to milliseconds.

In a working device, catalyst stability is also an important issue, with turnovers of  $\geq 10^6$  per year cited as a figure of merit for commercialization<sup>93,114</sup> and  $\sim 10^9$  turnovers desirable before replacement by a new catalyst in a commercial device.<sup>114</sup> Catalyst stability on these time scales has yet to be proven, but turnovers through 10,000s of cycles have been reported.<sup>159,218,222,227</sup>

### 3.8. Intra-assembly Electron Transfer: Catalyst Activation

For the oxide-bound assembly in Figure 9, injection is followed by electron transfer activation of the catalyst. Water oxidation is a  $4\text{e}^-$  process requiring four excitation/injection cycles with the resulting oxidative equivalents delivered to the catalyst for water oxidation. In a TiO<sub>2</sub>-based DSPEC the energetic demands on chromophore and excited state are narrow and demanding. The chromophore excited state or states must be sufficiently reducing to inject into the conduction band of the semiconductor with high efficiency. At the same time, the oxidized form must be thermodynamically capable of driving the WOC through a complete water oxidation cycle including the highest potential step, ultimately with loss of  $4\text{e}^-$ .

Assembly 18 (see Figure 28, below) provides a useful perspective on energy demands. At pH 1,  $E^{\circ'}$  for the excited state of its chromophore as a reducing agent is  $E^{\circ'}(\text{Ru}^{\text{II}}(\text{bpy})/\text{Ru}^{\text{III}}(\text{bpy}^-)) \approx -0.7$  V vs NHE, and injection occurs with high efficiency. Following injection, the oxidized chromophore, with  $E^{\circ'}(\text{Ru}^{\text{III}/\text{II}}) = 1.36$  V, is capable of oxidizing the catalyst from  $-\text{Ru}_b^{\text{II}}-\text{OH}_2^{2+}$  to  $-\text{Ru}_b^{\text{IV}}=\text{O}^{2+}$ , with  $E^{\circ'} = 1.15$  and 0.90 V for the  $-\text{Ru}_b^{\text{III}}-\text{OH}_2^{3+/2+}$  and  $-\text{Ru}_b^{\text{IV}}=\text{O}^{2+}/-\text{Ru}_b^{\text{III}}-\text{OH}_2^{3+}$  couples. However, the active form of the catalyst is  $-\text{Ru}_b^{\text{V}}(\text{O})^{3+}$ , with  $E^{\circ'} \approx 1.6$  V for the  $-\text{Ru}_b^{\text{V}}(\text{O})^{3+}/-\text{Ru}_b^{\text{IV}}=\text{O}^{2+}$  couple. Following a third excitation/injection cycle to give  $-[\text{Ru}_a^{\text{III}}-\text{Ru}_b^{\text{IV}}=\text{O}]^{4+}$ , there is insufficient potential in  $-\text{Ru}_a^{\text{III}}$  to access the active  $-\text{Ru}_b^{\text{V}}(\text{O})^{2+}$  form of the catalyst at 1.6 V, creating a kinetic roadblock. The successful use of this assembly in DSPEC applications for water splitting relies on O---O bond formation by  $-[\text{Ru}_a^{\text{III}}-\text{Ru}_b^{\text{IV}}=\text{O}]^{4+}$  by the EAPT pathway described in section 3.7.5, in which O-atom transfer to a water molecule occurs in concert with single-electron transfers to  $-\text{Ru}_a^{\text{III}}$  and  $-\text{Ru}_b^{\text{IV}}=\text{O}$ . Modifying the synthetic chemistry to increase  $E^{\circ'}$  for the  $-\text{Ru}_a^{\text{III}/\text{II}}-\text{Ru}_b^{\text{IV}}=\text{O}]^{5+/4+}$  couple is possible, but at the expense of  $E^{\circ'}$  for injection.

Although data are limited, for the examples that have been studied, intra-assembly electron-transfer oxidation of the catalyst is rapid. From ultrafast TA measurements on assemblies 17, 19, and 20 (see Figure 28),  $\tau_{\text{intra}} = 145, 380,$  and 170 ps, respectively, for intra-assembly electron-transfer oxidation,  $-[\text{Ru}_a^{\text{III}}-\text{Ru}_b^{\text{II}}-\text{OH}_2]^{5+} \rightarrow -[\text{Ru}_a^{\text{II}}-\text{Ru}_b^{\text{III}}-\text{OH}_2]^{5+}$ , in 0.1 M HClO<sub>4</sub> at room temperature. All of the intramolecular reactions are thermodynamically favored, with  $\Delta G^{\circ'} \approx -0.30$  eV for assembly 17, for example. They are far more rapid than  $\sim\mu\text{s}$  BET,  $\text{TiO}_2(\text{e}^-)|-[\text{Ru}_a^{\text{II}}-\text{Ru}_b^{\text{III}}-\text{OH}_2]^{5+} \rightarrow \text{TiO}_2|-\text{[Ru}_a^{\text{II}}-\text{Ru}_b^{\text{II}}-\text{OH}_2]^4$ , which is an important factor in maximizing DSPEC efficiencies.

### 3.9. DSPEC Dynamics

At the microscopic level, the efficiency of a DSPEC device is dictated by the fraction of light absorbed, the injection efficiency, and the microscopic dynamics that occur following injection. A summary of relevant time scales is shown in Figure 18 for assembly 15 (see Figure 28). It highlights the extraordinary range of time scales that play a role in an operating DSPEC. Time scales extend from the femtosecond to picosecond time scale for injection to an indefinite time scale for stable surface binding.

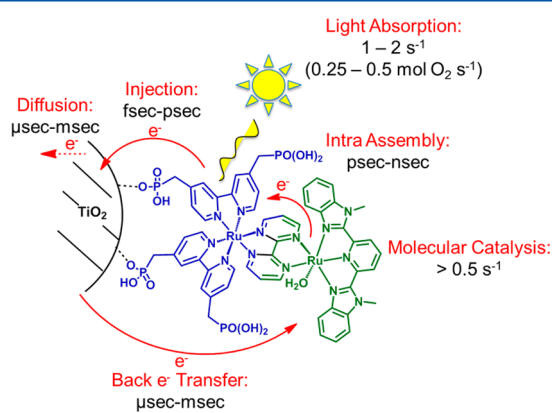
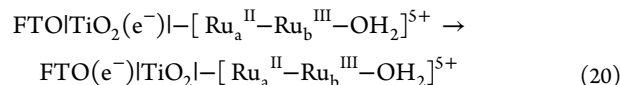
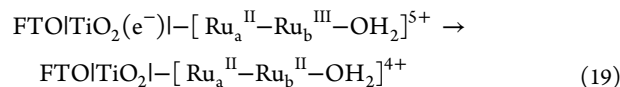


**Figure 18.** Interfacial processes and time scales that dictate DSPEC performance following light absorption and injection into a semiconductor oxide, with assembly 15 (see Figure 28),  $[(4,4'-\text{PO}_3\text{H}_2)_2\text{bpy}]_2\text{Ru}(4\text{-Mebpy}-4'\text{-bimpy})\text{Ru}(\text{tpy})(\text{OH}_2)]^{4+}$ , used as the example.

In ambient sunlight, the relatively low rate of solar insolation of  $\sim 2 \text{ s}^{-1}$  in the Vis and the requirement for four-photon absorption are significant factors affecting device efficiencies. Even though rapid, efficient injection and intra-assembly catalyst activation occur with absorption of a first photon, further  $1\text{e}^-$  activation of the catalyst must await a second solar photon. The second light absorption event also occurs on the seconds time scale, while BET from injected electrons in TiO<sub>2</sub> to the oxidized assembly, eq 19, occurs on the microsecond time scale, Section 7. Here, FTO is a fluorine-doped tin oxide (F:SnO<sub>2</sub>) collector electrode.



DSPEC efficiencies are dictated by the relative time scales for BET and electron diffusion through the TiO<sub>2</sub>. The latter varies with applied bias, light intensity, and other factors but typically occurs on the milliseconds time scale. *With this mismatch in rates between intra-oxide electron diffusion and back electron transfer, the efficiency of building up oxidative equivalents at the catalyst is greatly limited, even for single-photon excitation.* With a requirement for four photon-driven excitation/electron transfer cycles, DSPEC water splitting at TiO<sub>2</sub> is predicted to be highly inefficient.

In PSII in natural photosynthesis, competition from BET is addressed in two ways. One is by enhancing the rate of solar insolation by using an antenna effect in which a multiple-component chromophore array/antenna focuses excited-state energy to terminal chlorophyll P<sub>680</sub>, effectively increasing the rate of solar insolation into the millisecond time scale. Once formed, <sup>1</sup>P<sub>680</sub>\* undergoes rapid (picoseconds) oxidative quenching by a neighboring pheophytin to give P<sub>680</sub><sup>+</sup>. Oxidative quenching is followed by a sequence of four additional electron transfers, delivering an oxidative equivalent to the Mn<sub>4</sub>Ca core in the OEC and a reductive equivalent to quinone Q<sub>B</sub>. The two redox sites are separated by >50 Å, and the electron-transfer sequence is complete on the nanosecond time scale.<sup>21,102,270–272</sup> At this separation distance, BET between Q<sub>B</sub><sup>–</sup> and the oxidized Mn<sub>4</sub>Ca cluster is slow allowing multiple oxidative equivalents to be accumulated and water oxidation to occur.

Multiple strategies have been exploited to slow BET in DSSCs to maximize efficiencies. They include increasing the separation distance between the chromophore and metal oxide surface by chemical modification,<sup>273–277</sup> placing insulating layers between the semiconductor interface and the chromophore,<sup>160,162,163,278,279</sup> altering the mesoporous structure of the semiconductor,<sup>280–282</sup> and increasing the conductivity of the semiconductor by doping or added blocking layers.<sup>126,283,284</sup>

**3.9.1. Core/Shell Advantage.** Recently, the kinetic equivalent of the electron-transfer chain in PSII was introduced into DSPECs by using oxide core/shell structures to control local interfacial dynamics resulting in greatly enhanced efficiencies. ALD was used to prepare thin, 2–4 nm conformal shells of TiO<sub>2</sub> on the surfaces of nanoparticle films of the transparent conducting oxides nanoITO or nanoATO or the semiconductor SnO<sub>2</sub>.<sup>167,285</sup> Figure 19 shows a transmission electron microscopy (TEM) image of a core/shell nanoparticle

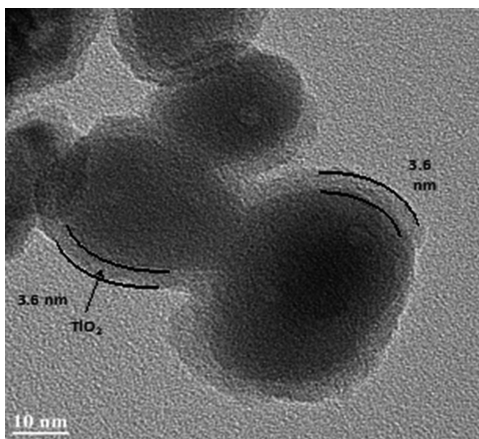
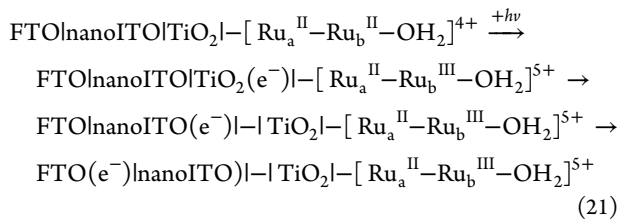


**Figure 19.** TEM of a nanoITO/TiO<sub>2</sub> core/shell structure in a nanoITO film with a 3.6 nm shell of TiO<sub>2</sub>. Reprinted with permission from ref 126. Copyright 2013 Proceedings of the National Academy of Science.

film structure of nanoITO with a 3.6 nm TiO<sub>2</sub> shell. In these core/shell structures, electron injection from the excited chromophore to the TiO<sub>2</sub> shell is followed by rapid electron transfer through the thin shell to the core, eq 21. Once in the

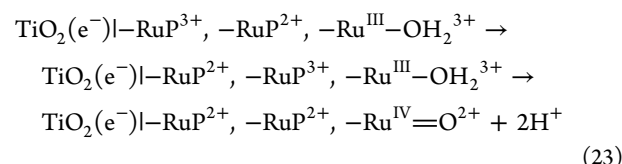
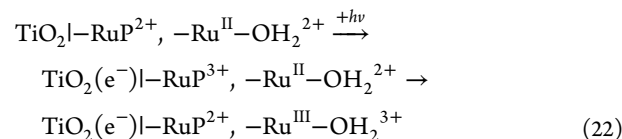


core, electron transfer to the underlying collector electrode limits BET, allowing multiple oxidative equivalents to accumulate at the external catalyst where water oxidation occurs, with H<sub>2</sub> evolution occurring at the cathode.<sup>126</sup> BET by tunneling through the thin TiO<sub>2</sub> layer to the assembly is still a competing process, with per-photon absorbed efficiencies for water splitting of only 4.4% obtained with assembly 18 (see Figure 28) as the chromophore–catalyst assembly. With the same assembly, but on a SnO<sub>2</sub>/TiO<sub>2</sub> core/shell, the efficiencies are increased by factors of 3–5. With SnO<sub>2</sub> as the core, BET to the assembly on TiO<sub>2</sub> is inhibited because of a ~0.4 V unfavorable potential gradient for SnO<sub>2</sub>(e<sup>-</sup>) → TiO<sub>2</sub> electron transfer.<sup>126,286</sup>

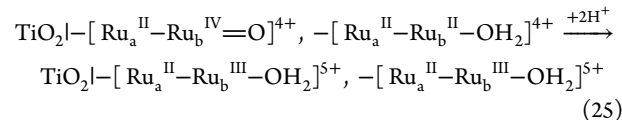
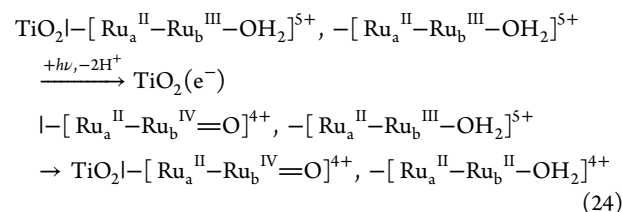
Electron-transfer dynamics have been investigated for a DSSC with a nanoITO/TiO<sub>2</sub> core/shell by a combination of photocurrent, electrochemical impedance, and open-circuit TA measurements.<sup>287</sup> They reveal an important role for shell thickness, with a maximum cell efficiency reached at ~3.6 nm. The thickness effect was attributed to a decrease in the rate of FTO|nanoITO(e<sup>-</sup>) → Ru(III) BET because of the longer tunneling distance. For thicker films, trap states appear in the shell, inhibiting electron transport to the core.

**3.9.2. Cross-Surface Electron Transfer Activation and Accumulation of Redox Equivalents.** Even given the kinetic limitations on TiO<sub>2</sub> as a photoanode, Sun and co-workers have reported significant photocurrents on TiO<sub>2</sub> surfaces co-loaded with chromophores and catalysts. Their results point to a mechanism for accumulating oxidative equivalents at the TiO<sub>2</sub> surface, even given the unfavorable local electron-transfer

dynamics following injection.<sup>288,289</sup> A possible explanation for this effect has come from recent TA and steady-state measurements on surfaces co-loaded with RuP<sup>2+</sup> and the WOC [Ru(Mebimpy)(4,4'-(PO<sub>3</sub>H<sub>2</sub>)<sub>2</sub>bpy)(OH<sub>2</sub>)]<sup>2+</sup>, assembly 26 (see Figure 29), with chromophore-to-catalyst ratios from 2.2:1 to 8.5:1. Light absorption and injection in these assemblies is dominated by -RuP<sup>2+</sup>. As shown by TA measurements, following injection, rapid, sub-nanosecond oxidation of the nearest-neighbor catalyst occurs, eq 22. Local oxidation is in competition with -RuP<sup>3+</sup>/-RuP<sup>2+</sup> electron-transfer migration across the surface, with further oxidation of -Ru<sup>III</sup>-OH<sub>2</sub><sup>3+</sup> to -Ru<sup>IV</sup>=O<sup>2+</sup>, eq 23. This and related sequences provide a biphotonic mechanism for building up higher oxidation states by cross-surface electron transfer. Under steady-state photolysis conditions, ~10% of the catalyst sites were estimated to be present on the surface as -Ru<sup>IV</sup>=O<sup>2+</sup> for assembly 26.<sup>290</sup>



In a more recent TA study, injection and interfacial electron transfer were investigated for assembly 18 (shown in Figure 28 and introduced in section 3.7.5) on TiO<sub>2</sub> in both the -[Ru<sub>a</sub><sup>II</sup>-Ru<sub>b</sub><sup>II</sup>-OH<sub>2</sub>]<sup>4+</sup> and -[Ru<sub>a</sub><sup>II</sup>-Ru<sub>b</sub><sup>III</sup>-OH<sub>2</sub>]<sup>5+</sup> forms in 0.1 M HClO<sub>4</sub>. For the mixed-valence assembly, TA measurements following excitation and injection revealed the growth of -[Ru<sub>a</sub><sup>II</sup>-Ru<sub>b</sub><sup>II</sup>-OH<sub>2</sub>]<sup>4+</sup> and -[Ru<sub>a</sub><sup>II</sup>-Ru<sub>b</sub><sup>IV</sup>=O]<sup>4+</sup> separately across the surface. It was proposed that, following injection, electron migration occurs through the oxide, with trapping at -[Ru<sub>a</sub><sup>II</sup>-Ru<sub>b</sub><sup>III</sup>-OH<sub>2</sub>]<sup>5+</sup>, eq 24. This sequence of events leaves -[Ru<sub>a</sub><sup>II</sup>-Ru<sub>b</sub><sup>II</sup>-OH<sub>2</sub>]<sup>4+</sup> and -[Ru<sub>a</sub><sup>II</sup>-Ru<sub>b</sub><sup>IV</sup>=O]<sup>4+</sup> at isolated sites across the surface, and cross-surface electron transfer between them, eq 25, is slow, occurring on the time scale of tens of microseconds.



In either of these sequences with co-loaded assembly 26 or assembly 18, a microscopic basis exists for the transient and steady-state appearance of water oxidation precursors, TiO<sub>2</sub>|-RuP<sup>2+</sup>, Ru<sup>IV</sup>=O<sup>2+</sup> or -[Ru<sub>a</sub><sup>II</sup>-Ru<sub>b</sub><sup>IV</sup>=O]<sup>5+</sup>, on TiO<sub>2</sub>, providing a basis for a third excitation/electron-transfer cycle and water oxidation.

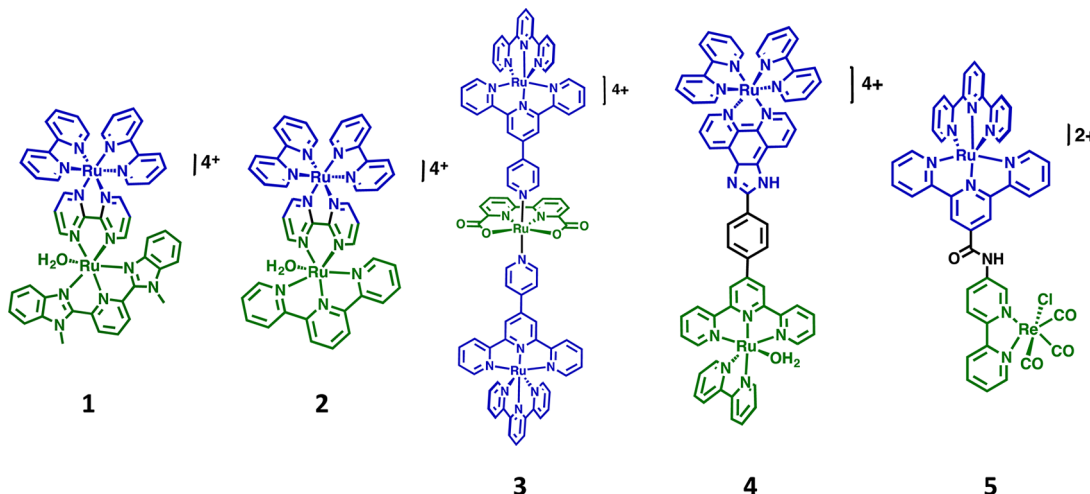


Figure 20. Structures of solution chromophore–catalyst assemblies 1–5.

#### 4. CHROMOPHORE–CATALYST ASSEMBLIES IN SOLUTION

Significant progress has been made in the synthesis, characterization, and reactivity of molecular chromophore–catalyst assemblies for catalytic water oxidation or  $\text{H}^+/\text{CO}_2$  reduction, as summarized in recent reviews.<sup>92,114,115,291,292</sup> In these assemblies, the typical structural motif is a light-harvesting chromophore covalently linked to an oxidation or reduction catalyst by a bridging ligand. As shown in Figure 20, ligand bridges that have been used include 2,2'-bipyrimidine (1,<sup>218,293</sup> 2),<sup>294,295</sup> pyridine (3),<sup>294,295</sup> imidazole (4),<sup>296</sup> and direct amide bonding (5)<sup>297</sup> (Figure 20), all with intact, ligand-based  $\pi$ -bonding networks between the linked metal centers. *In the structures in Figure 20, and elsewhere in this Review, the chromophore is color-coded blue and the catalyst green to help identify the functional components.*

In this series, use of unsaturated bridging ligands comes with a potential disadvantage. As illustrated for assembly 1 in Figure 21, if the  $\pi^*$  levels of the bridge fall below those of the surface-

synthesized by amide coupling (7,<sup>267</sup> 8<sup>294</sup>) and by click chemistry (9<sup>299</sup>), with examples shown in Figure 22.

Due to the absence of an orbital basis for significant electronic coupling, the chromophore and catalyst components in these assemblies maintain their individual electronic properties. This is evident in the UV–vis spectrum of 7 in  $\text{H}_2\text{O}$  in Figure 23, which compares spectra for chromophore  $[\text{Ru}(\text{bpy})_2(4'\text{-methyl-2,2'-bipyridin-4-yl})\text{methanamine}]^{2+}$  (green), catalyst  $[\text{Ru}(4\text{-COOH-tpy})(\text{bpy})(\text{OH}_2)]^{2+}$  (blue, COOH-tpy = 4-(2,2'-6'2-terpyridin-4'-yl)benzoic acid), chromophore and catalyst (cyan), and the assembly (red), all in  $\text{H}_2\text{O}$  at room temperature.<sup>267</sup>

Complexes 6–8 retain their catalytic water oxidation properties, both electrochemically and chemically with Ce(IV) as a chemical oxidant. It is notable that Ce(IV)-driven water oxidation by assembly 6 is 8 times more rapid than that by the component catalyst,  $[\text{Ru}(\text{tpy})(\text{Mebimpy})(\text{OH}_2)]^{2+}$ , Figure 24. The rate enhancement was attributed to a redox mediator effect, with prior, rapid oxidation of the chromophore followed by intra-assembly oxidation of the catalyst.<sup>216,298</sup> The redox mediator effect is discussed in more detail in Section 6.

Other chromophores have also been investigated for possible use in PEC applications, including porphyrin 10<sup>300</sup> and the organic dye-based assemblies 11–13,<sup>301</sup> Figure 25. Wasielewski and co-workers have pioneered the use of perylene-3,4:9,10-bis(dicarboximide) (PDI) chromophores chemically linked to a known Ir(III)-based WOC (12 and 13, Figure 25).<sup>302</sup> Time-resolved TA measurements have been used to demonstrate that, following photoexcitation of the perylene chromophore, ultrafast electron transfer from the Ir(III) catalyst to a perylene excited state occurs on the picosecond time scale, eq 26. Excitation and electron transfer give the redox-separated state  $\text{PDI}^{\bullet-}\text{Ir}^{\text{IV}}$ , while the form of the catalyst active toward water oxidation is  $\text{Ir}^{\text{V}}$ .<sup>228,229</sup> The redox-separated state in 12 is short-lived, undergoing BET to the ground state with biexponential kinetics, with  $\tau_1$  and  $\tau_2 = 14$  and 75 ps, respectively, as determined by monitoring the  ${}^1\text{PDI}^{\bullet}$  absorption centered at 725 nm (Figure 26).<sup>302</sup>



Oxidative quenching of  $\text{Ru}(\text{bpy})_3^{2+*}$  by methyl viologen ( $\text{MV}^{2+}$ ), added as an oxidative quencher, eq 28, has been used to generate  $\text{Ru}(\text{bpy})_3^{3+}$  as a transient for oxidative activation of

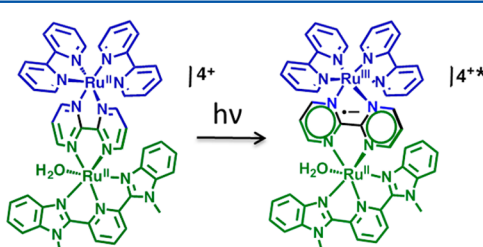
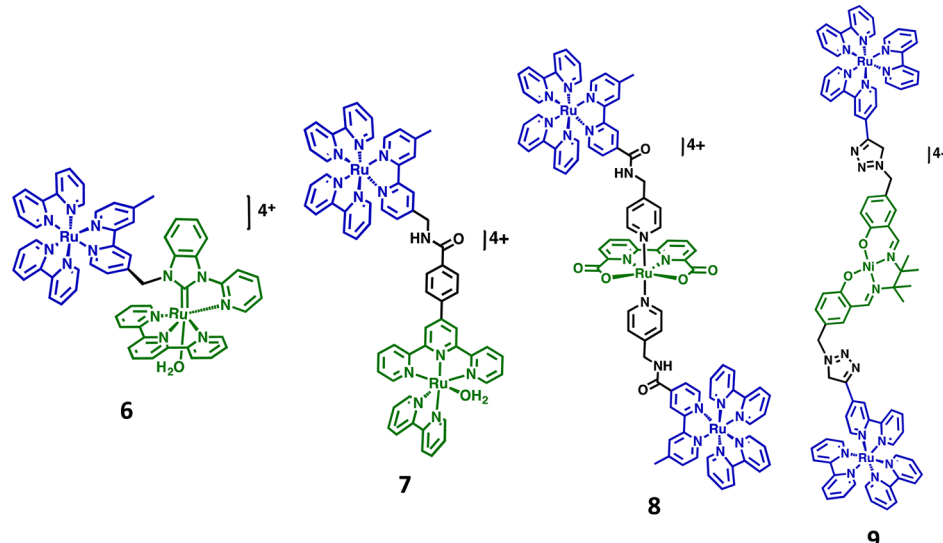


Figure 21. Photoexcitation to an MLCT localized on the bridging ligand.

bound, injecting chromophore, then the lowest excited state lies away from the surface toward the catalyst. This can greatly inhibit injection either dynamically or by introducing a lowest-lying MLCT state below the conduction-band edge.<sup>266,269</sup>

Assemblies have been prepared with saturated methylene spacers that avoid low-lying bridge-based excited states, with examples shown in Figure 22. Chromophore–catalyst assembly 6,  $[(\text{bpy})_2\text{Ru}(4\text{-Mebpy-4'-bimpy})\text{Ru}(\text{tpy})(\text{OH}_2)]^{4+}$ , with a single methylene spacer, is notable for its use in DSPECs for water splitting, Section 3.<sup>298</sup> Assemblies have also been



**Figure 22.** Structures of chromophore–catalyst assemblies **6–9** with saturated bridges.

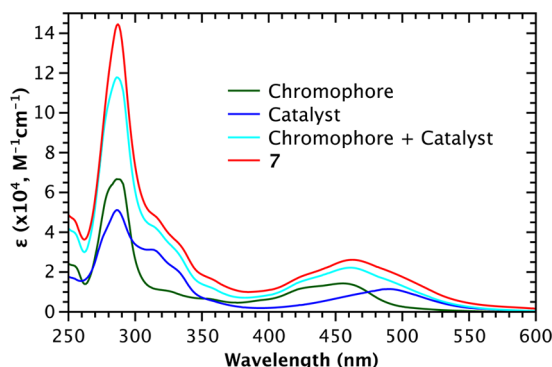


**Figure 23.** Absorption spectra of chromophore  $[\text{Ru}(\text{bpy})_2(4'\text{-methyl}-2,2'\text{-bipyridin-4-yl})\text{methanamine}]^{2+}$  (green), catalyst  $[\text{Ru}(4\text{-(COOH-tpy)}(\text{bpy})(\text{OH}_2)]^{2+}$  (blue), chromophore + catalyst (cyan), and assembly **7** (red) in  $\text{H}_2\text{O}$ . Reprinted with permission from ref 267. Copyright 2012 American Chemical Society.

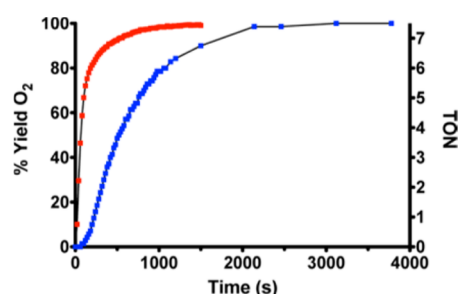
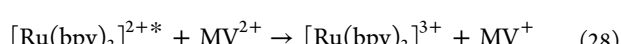
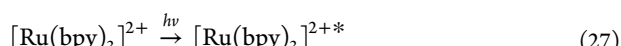


**Figure 24.**  $\text{O}_2$  evolution with time for the catalyst  $[\text{Ru}(\text{tpy})\text{-(Mebimpy)}(\text{OH}_2)]^{2+}$  (blue) and assembly **6** (blue) with 30 equiv of added  $\text{Ce}(\text{IV})$  at 298 K in 0.1 M  $\text{HNO}_3$ . Reprinted with permission from ref 298. Copyright 2013 American Chemical Society.

chromophore–catalyst assemblies in solution.<sup>303–306</sup> However, under diffusional conditions, BET between the oxidized assembly and  $\text{MV}^+$  is rapid, and it is not possible to build-up multiply oxidized assemblies to any significant extent.



## 5. CHROMOPHORE–CATALYST ASSEMBLIES ON OXIDE SURFACES

As noted in Section 3.4.1, the most commonly used oxide surface attachment strategies are based on carboxylic acid ( $-\text{CO}_2\text{H}$ ) and phosphonic acid ( $-\text{PO}_3\text{H}_2$ ) derivatives. Surface loading from organic solvents by  $-\text{CO}_2\text{H}$  derivatives or from organic solvents or acidic aqueous solutions of  $-\text{PO}_3\text{H}_2$  derivatives by simple dipping methods results in surface binding by surface carboxylate or phosphonate ester formation.<sup>154</sup> Phosphonate–surface ester binding in aqueous solutions is far more stable than carboxylate binding, as highlighted in a recent photochemical study.<sup>136,154</sup> Phosphonic acid derivatives are required for long-term surface stability unless the carboxylates are surface-stabilized.<sup>156–158,160,163,166</sup> Methods for stabilization of surface binding by ALD, hydrophobic polymer overlays, and electro-assembly overlayer formation were discussed in Section 3.4.1.

Redox potentials for surface-bound couples are typically obtained by cyclic voltammetry (CV) or square wave voltammetry (SWV) on transparent conducting oxide (TCO) electrodes—fluoride-doped tin oxide (FTO), antimony-doped tin oxide (ATO), or tin-doped indium oxide (ITO)—with the assembly surface-bound to the oxide. Nanoparticle, mesoscopic films of the same materials—nanoITO, nanoATO—have low resistivities ( $\sim 10^{-4} \Omega \text{ cm}$ ) and optical transmittances of greater than 80% in the Vis and UV, enabling spectroelectrochemical characterization of surface-bound intermediates and applications in PEC devices.<sup>307–310</sup> Electrochemical measurements of complexes or assemblies on  $\text{TiO}_2$ , or other semiconductor oxide at potentials within the bandgap of semiconductor, are possible on fully loaded surfaces at slow scan rates by site-to-site, cross-surface electron-transfer hopping to the underlying conducting substrate.

The use of high-surface-area, three-dimensional oxide electrodes is highly advantageous compared to planar oxide electrodes. The higher surface areas lead to significant current enhancements and provide internal structures that mimic those used in DSPEC semiconductor oxides.<sup>93,113</sup> Because of their high surface areas, accurate determination of assembly loadings is possible and they allow acquisition of spectral and electrochemical data on intermediates as they form on the

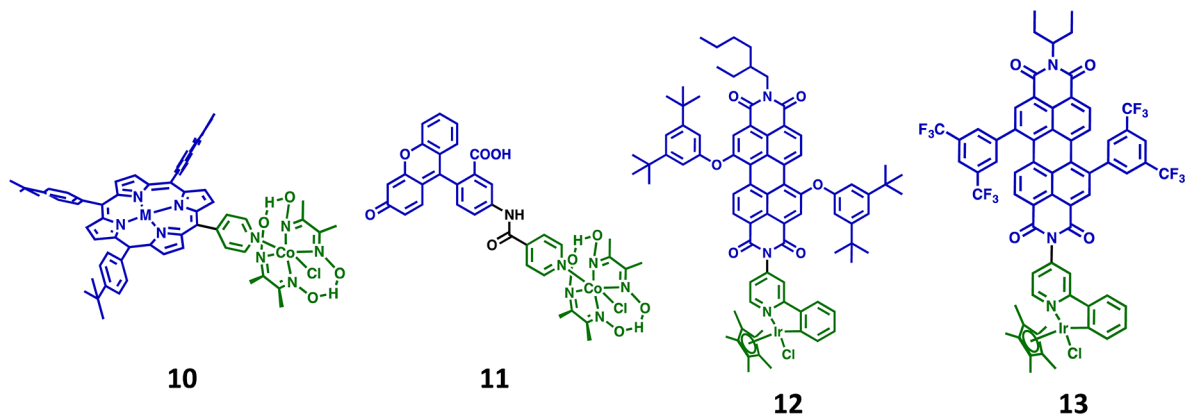


**Figure 25.** Structures of porphyrin **10** and organic dye-based chromophore–catalyst assemblies **11–13**.

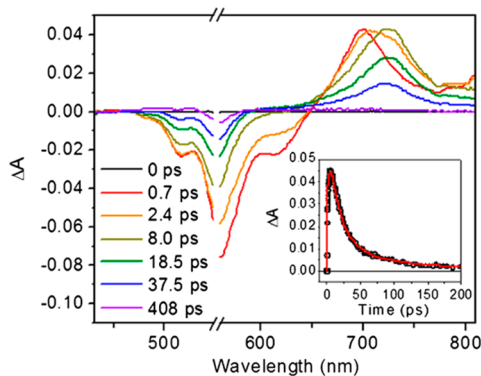


**Figure 26.** Femtosecond transient absorption spectra of assembly **12** in  $\text{CH}_2\text{Cl}_2$  with 550 nm laser excitation at room temperature. Inset: Kinetic trace at 725 nm with a nonlinear least-squares fit. Reprinted with permission from ref 309. Copyright 2013 Proceedings of the National Academy of Science.

surface. Based on a considerable body of experimental data, the properties of assemblies surface-bound to these oxides are largely retained.<sup>263</sup>

### 5.1. Surface Loading

Strategies for surface attachment to oxide electrodes have been reviewed elsewhere.<sup>311–315</sup> Surface loadings are evaluated either by electrochemical or spectrophotometric monitoring and reported as surface coverages,  $\Gamma$  in  $\text{mol}/\text{cm}^2$  or, for nanoparticle film electrodes in  $\text{mol}/\text{cm}^2/\mu\text{m}$ . With electrochemical monitoring by CV, surface loading is evaluated from the areas under cyclic voltammetric waves with the use of eq 29, where  $Q_{cv}$  is

$$\Gamma = Q_{cv}/nFA \quad (29)$$

the integrated charge from the area of the background-corrected current–potential waveform,  $n$  is the number of electrons transferred for the redox couple,  $F$  is Faraday's constant, and  $A$  is the surface area of the electrode in  $\text{cm}^2$ .<sup>316</sup>

Surface coverages are also evaluated from UV–Vis measurements by using eq 30, with  $A(\lambda)$  the measured absorbance and

$$\Gamma = \frac{A(\lambda)}{10^3 \epsilon(\lambda)} \quad (30)$$

$\epsilon(\lambda)$  the molar absorptivity at wavelength  $\lambda$  for a solution analogue.<sup>317</sup> Figure 27 illustrates surface loading of the catalyst

$[\text{Ru}(\text{Mebimpy})(4,4'-(\text{PO}_3\text{H}_2)_2\text{bpy})(\text{OH}_2)]^{2+}$ , 0.1 mM in methanol, on nanoITO monitored at  $\lambda_{\max} = 493 \text{ nm}$  ( $\epsilon_{\max} = 1.5 \times 10^4 \text{ M}^{-1}$ ) as a function of soaking time. The results of equilibrium surface loading studies as a function of added complex or assembly typically follow Langmuir isotherm behavior, characterized by a surface binding constant,  $K$ .<sup>136,154,318,319</sup> Comparisons between surface coverages obtained from electrochemical and spectroscopic measurements typically show that all surface-bound sites are electroactive.<sup>165,166,217,263</sup>

### 5.2. Oxide-Bound Assemblies

The first example of a DSPEC based on a chromophore–catalyst assembly, surface-bound to  $\text{TiO}_2$ , appeared in 1999 and applied to the dehydrogenation of 2-propanol to acetone.<sup>320</sup> Water oxidation catalysis by the surface bound assemblies  $[(4,4'-(\text{PO}_3\text{H}_2\text{CH}_2)_2\text{bpy})_2\text{Ru}^{\text{II}}(\text{bpm})\text{Ru}^{\text{II}}(\text{tpy})(\text{OH}_2)]^{4+}$  (**14**,  $4,4'-(\text{PO}_3\text{H}_2\text{CH}_2)\text{bpy} = ([2,2'\text{-bipyridine}]-4,4'\text{-dihydrobis(methylene)})\text{bis}(\text{phosphonic acid})$ ) and  $[(4,4'-(\text{PO}_3\text{H}_2\text{CH}_2)_2\text{bpy})_2\text{Ru}^{\text{II}}(\text{bpm})\text{Ru}^{\text{II}}(\text{Mebimpy})(\text{OH}_2)]^{4+}$  (**15**), Figure 28,<sup>218</sup> was reported in 2009. The results of TA measurements on injection and BET for the assembly  $[(\text{dcb})_2\text{Ru}^{\text{II}}(\text{bpy-Mebimpy})_2\text{Ru}^{\text{II}}(\text{bpy})(\text{OH}_2)]^{4+}$  (**16**,  $\text{dcb} = 4,4'\text{-dicarboxylic acid-2,2'\text{-bipyridine}}$ ;  $\text{bpy-Mebimpy} = 2,2'\text{-}(4\text{-methyl-[2,2':4',4'\text{-terpyridine]}-2'',6''\text{-diyl})bis(1-methyl-1H-benzo[d]imidazole)}$ ) were reported in 2011 by Song et al., Figure 28.<sup>269</sup> In assemblies **14–16**, the electronic properties of the assemblies are significantly modified compared to those of the separate chromophore and catalyst components by the electronic interaction through the ligand bridge.

In the assemblies  $[(\text{PO}_3\text{H}_2\text{CH}_2)_2\text{bpy})_2\text{Ru}^{\text{II}}(\text{bpy-NH-CO-tpy})\text{Ru}^{\text{II}}(\text{bpy})(\text{OH}_2)]^{4+}$  (**17**,  $\text{bpy-NH-CO-tpy} = N\text{-(}[2,2'\text{-bipyridin}-4\text{-ylmethyl})-4\text{-([2,2':6',2''\text{-terpyridin}-4\text{-yl})-benzamide]}$ ) and  $[(\text{PO}_3\text{H}_2)_2\text{bpy})_2\text{Ru}^{\text{II}}(4\text{-Mebpy-4'\text{-bimpy}})\text{Ru}^{\text{II}}(\text{tpy})(\text{OH}_2)]^{4+}$  (**18**,  $(\text{PO}_3\text{H}_2)_2\text{bpy} = [2,2'\text{-bipyridine}]-4,4'\text{-dihydrobis(phosphonic acid)}$ ,  $4\text{-Mebpy-4'\text{-bimpy}} = 4\text{-}(4\text{-methyl-bipyridin-4'-yl)-N-(benzimid)-N'-pyridine}$ ) a bridging ligand with saturated links between chromophore and catalyst was incorporated to interrupt conjugation in the bridging ligand (Figure 28).<sup>265,266</sup> In these assemblies, the lowest energy MLCT excited state(s) are oriented toward the metal oxide interface, and the saturated spacers were added to provide a basis for controlling BET from the surface following injection,  $\text{TiO}_2(\text{e}^-)\text{I}-[\text{Ru}_a^{\text{II}}-\text{Ru}_b^{\text{III}}-\text{OH}_2]^{5+} \rightarrow \text{TiO}_2\text{I}-[\text{Ru}_a^{\text{II}}-\text{Ru}_b^{\text{II}}-\text{OH}_2]^{4+}$ . However, as noted in Section 3, BET for the assemblies studied to date is dominated by slow electron transport within the nanoparticle  $\text{TiO}_2$  films.

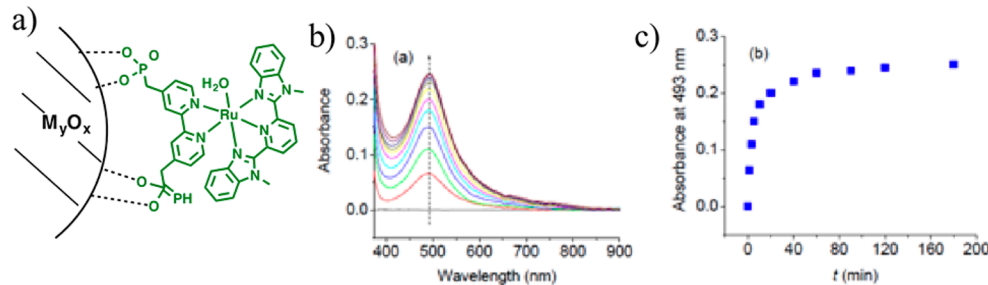


**Figure 27.** (a) Structure of surface-bound water oxidation catalyst  $[\text{Ru}(\text{Mebimpy})(4,4'-(\text{PO}_3\text{H}_2)_2\text{-bpy})(\text{OH}_2)]^{2+}$  bound to a metal oxide electrode. (b) UV–vis spectra as a function of soaking time in a 0.1 mM solution of the catalyst in methanol on nanoITO. (c) Dependence of the absorbance at 493 nm on the soaking time with full surface coverage reached at  $\Gamma^\circ = 1.7 \times 10^{-8} \text{ mol/cm}^2$  for a 10  $\mu\text{m}$  film, with  $\Gamma^\circ = 1.7 \times 10^{-9} \text{ mol/cm}^2/\mu\text{m}$ . Reprinted with permission from ref 217. Copyright 2009 American Chemical Society.

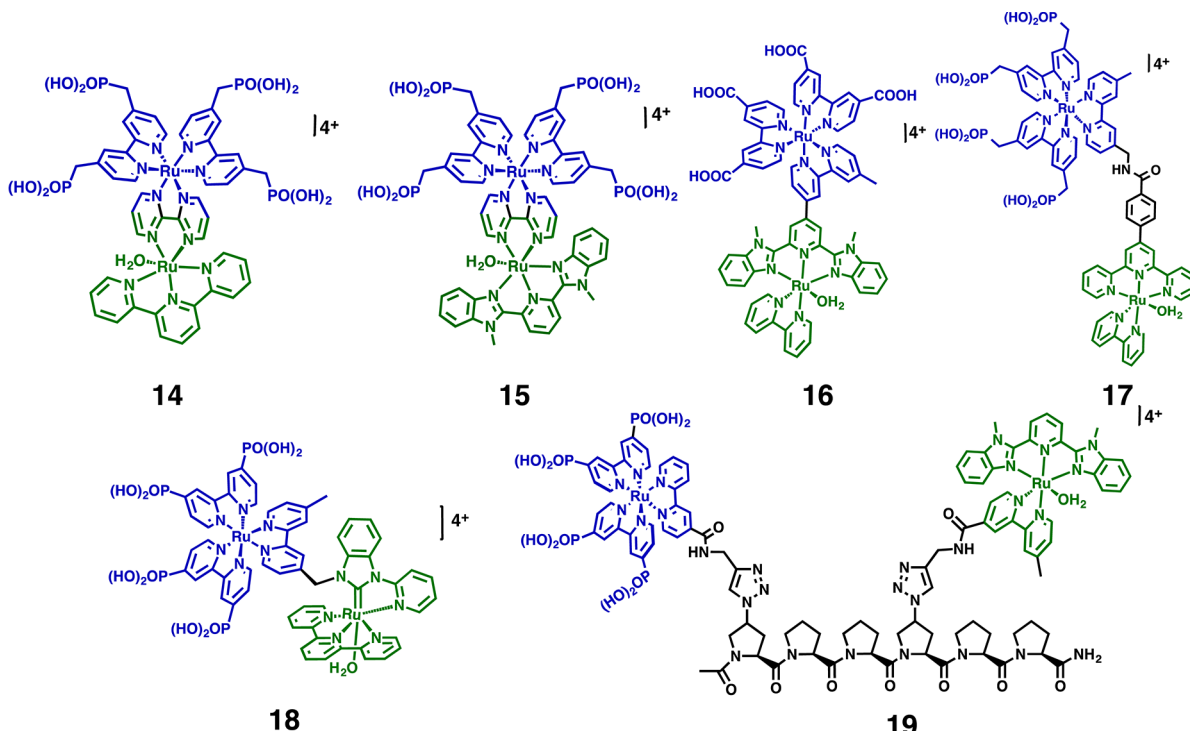


**Figure 28.** Structures of covalently linked assemblies 14–19.

Solid-phase peptide synthesis, with the controlled step-by-step addition of spacers or active functional groups, has been used to prepare peptide assemblies for investigating the distance dependence of electron and energy transfer in solution.<sup>321–325</sup> More recently, the same approach was used to prepare chromophore–catalyst assemblies such as 19.<sup>326</sup> In these syntheses, copper(I)-catalyzed azide–alkyne cycloaddition (CuAAC) was used to prepare the chromophore for addition to the helical proline assembly. The use of proline, with its propensity to form helical structures, adds a structural element with control of site-to-site separation distances in a well-defined molecular scaffold. In these assemblies, systematic variations in the peptide backbone lead to controlled spacings between chromophore and catalyst for investigating the distance dependence of electron and energy transfer.<sup>326,327</sup> Assembly structures such as 17 and 19 were designed to exploit the advantage of using systematic synthetic variations to control the spacing between chromophore and catalyst and, with it, the rate of BET following injection. However, as noted above, TA

measurements have shown that BET is dominated by electron transport within the oxide.

Covalently linked assemblies 14–19 provide well-defined structures for systematic investigations on oxide surfaces. However, they typically require multiple synthetic steps and result in low overall yields. More straightforward, and potentially practical, approaches have evolved based on surface assembly strategies. They include bilayers (20,<sup>328</sup> 21,<sup>329</sup> 22<sup>330</sup>) by layer-by-layer addition of a chromophore followed by a catalyst overlayer (Figure 29), assembly formation by electrostatic interactions between the surface-bound chromophore and a polyoxometalate WOC (23) by Hill and co-workers.<sup>331</sup> Ion-exchange overlayers of the oxidatively stable perfluorinated polymer Nafion have also been used to immobilize catalysts in films on top of pre-bound or adsorbed chromophores (24, 25).<sup>332,333</sup>

Notable for both generality and simplicity are co-loading approaches which have been used to assemble functioning DSPEC photoanodes, 26–29.<sup>288–290,334</sup> The use of electro-polymerization/electro-assembly to prepare layered, multi-

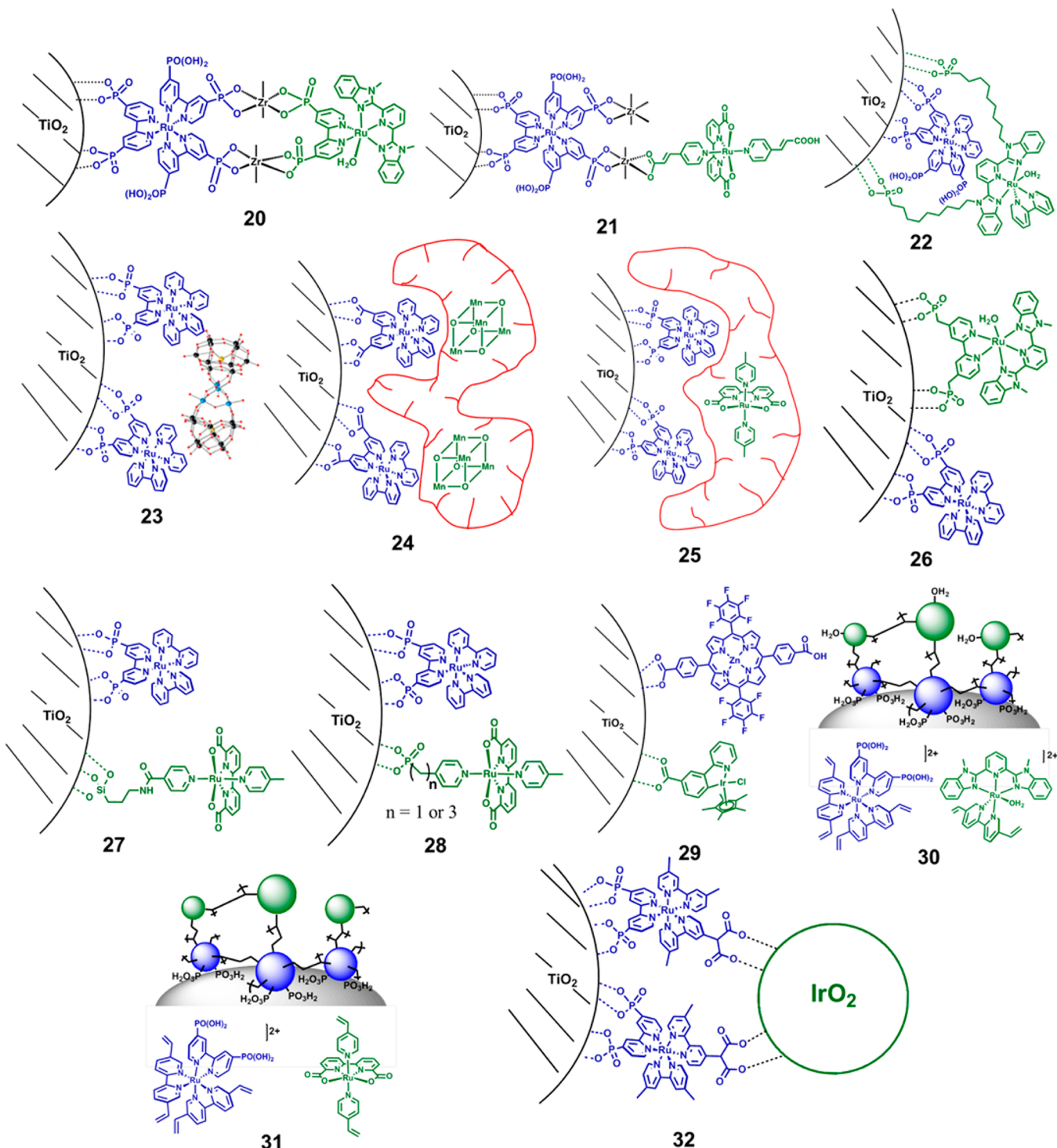


**Figure 29.** Structures of assemblies 20–32 prepared by surface assembly procedures. Local charges and proton contents for the surface-bound complexes are pH dependent.

component films on metal oxides, 30 and 31, has also been demonstrated.<sup>165–167</sup> The properties of these assemblies—electrocatalysis, photocatalysis, photophysics—are discussed in other sections.

Also notable, although outside the scope of this Review, which is focused on molecular-based assemblies, are the chromophore–oxide nanoparticle assemblies pioneered by Mallouk and co-workers. They incorporate iridium oxide nanoparticles as the WOC in photoanodes for use in DSPECs

and provided the first example of DSPEC water splitting.<sup>90,335,336</sup> A structure is shown as assembly 32 in Figure 29. In this design, the RuP<sup>2+</sup>-like chromophore is derivatized with a malonate group for selective binding to the IrO<sub>x</sub> WOC. IrO<sub>2</sub> has been shown to be a rapid and efficient WOC which operates at relatively low overpotentials, making the Ru(II) polypyridyl chromophore–IrO<sub>x</sub> attractive as an electrode design.<sup>335,337–339</sup> In DSPEC applications, a dual working

electrode was added for measuring photogenerated oxygen near the photoanode surface, Section 8.<sup>90,336</sup>

## 6. ELECTROCATALYTIC WATER OXIDATION

A close relationship exists between solar-driven and electrocatalytic water oxidation for assemblies on oxide surfaces. The use of electrochemical techniques to elucidate water oxidation mechanism is well-documented in recent reviews and was discussed briefly in Section 3.8.<sup>38,105,170,291,340</sup> Redox potentials for surface-bound couples are typically obtained by CV or SWV on planar or nanoparticle TCO electrodes.

Reduction potentials are listed in Table 1 for the assemblies in Figures 28 and 29. In this series, the chromophore potentials,

**Table 1. Formal Reduction Potentials,  $E^{\circ'}$  vs NHE, for Chromophore (Ch)–Catalyst (Cat) Assembly ( $\text{Ch}^{(n+1)}/\text{Ch}^n$ ) and Cat<sub>ox1</sub>, Cat<sub>ox2</sub>, and Cat<sub>ox3</sub>Couples**

assembly	$\text{Ch}^{(n+1)}/\text{Ch}^n$	Cat <sub>ox1</sub>	Cat <sub>ox2</sub>	Cat <sub>ox3</sub>
14 <sup>a</sup>	1.43	0.86	1.20	1.69
15 <sup>a</sup>	1.35	0.78	1.13	1.59
16 <sup>b</sup>	1.65	0.82	1.26	
17 <sup>a</sup>	1.32	1.04	1.15	
18 <sup>a</sup>	1.36	0.90	1.15	~1.5
19 <sup>a</sup>	1.24	0.71	1.16	
20 <sup>a</sup>	1.38	0.80	1.3	1.68
22 <sup>a</sup>	1.41	0.82	1.29	1.67
23 <sup>a</sup>	1.28	0.28	0.66	
24 <sup>c</sup>	1.35	1.12		
25 <sup>d</sup>	1.32	0.86	1.5	
26 <sup>a</sup>	1.32	0.90	1.26	1.68
27 <sup>e</sup>	1.40	0.71	1.14	1.25
28 <sup>f</sup>	1.40	0.68		~1.20
29 <sup>g</sup>	1.35	1.1	1.55	1.76
30 <sup>a</sup>	1.34	0.85	1.20	
31 <sup>h</sup>	~1.35	0.69	1.01	

<sup>a</sup>At pH 1. <sup>b</sup>In PC with 2% added water and 0.1 M KPF<sub>6</sub> in V vs NHE.

<sup>c</sup>In H<sub>2</sub>O (0.1 M Na<sub>2</sub>SO<sub>4</sub>) in a Nafion film, in V vs SCE. <sup>d</sup>At pH 1, in a Nafion film.

<sup>e</sup>At pH 6.8, in phosphate buffer. <sup>f</sup>In aqueous 0.1 M Na<sub>2</sub>SO<sub>4</sub> at pH 6.4. <sup>g</sup>In dichloromethane solution, 0.1 M in TBAPF<sub>6</sub>.

<sup>h</sup>Recorded in water at pH 1 (0.12 M Britton–Robinson buffer) with 30% CF<sub>3</sub>CH<sub>2</sub>OH added.

$\text{Ch}^{(n+1)} + e^- \rightarrow \text{Ch}^n$ , vary from 1.28 V vs NHE for assembly 23 to 1.65 V for 16. The high potential for the chromophore couple in assembly 16 is due to a change in medium, with the measurements carried out in PC with 2% added water.<sup>269</sup>

Notable features in these data include the significant variations in  $E^{\circ'}$  values for the sequence of catalyst couples that ultimately lead to water oxidation. These potentials—Cat<sub>ox1</sub>, Cat<sub>ox2</sub>, Cat<sub>ox3</sub>—vary greatly depending on the nature of the catalyst, the medium, and the pH-dependent properties of the individual couples. For most of the examples investigated, water oxidation with O–O bond formation occurs at the 3e<sup>-</sup>/2H<sup>+</sup> stage. Experimentally, it can be difficult to discern the wave for the final 1e<sup>-</sup> oxidation because of overlap with the current arising from water oxidation catalysis.

Controlled potential electrolysis measurements are used to evaluate catalyst turnover numbers (TONs) by integration of current–time traces with the use of eq 31. In this equation, C is

$$\text{TON} = C/nF n_{\text{Cat}} \quad (31)$$

the total charge passed, F is Faraday's constant, and  $n_{\text{Cat}}$  is the moles of catalyst. n is the number of electrons transferred, with n = 4 if water oxidation is the only reaction at the electrode. The turnover frequency (TOF), in s<sup>-1</sup>, is the TON divided by the electrolysis time. The long-term stability or instability of the catalyst is typically apparent from the stability or instability of long-term current–time traces. As noted in Section 3.7, the TON measures the total charge passed and, because of competing processes, may not be a direct measure of O<sub>2</sub> produced.

A more meaningful measure of catalytic efficiency is the Faradaic efficiency or percent efficiency. It is the fraction or percentage of the total current passed, accounting for the stoichiometry of the reaction that leads to the desired product. The Faradaic efficiency may differ significantly from the total charge passed due to side reactions or catalyst decomposition. An expression for the Faradaic efficiency is given in eq 32, with n, C, and F defined above and  $n_{\text{prod}}$  the moles of product, O<sub>2</sub> for the case of water oxidation.

$$\% \text{ Faradaic efficiency} = [(nF n_{\text{prod}})/C] \times 100\% \quad (32)$$

As noted above, electrocatalytic water oxidation for assemblies 14 and 15 was first reported on planar ITO and TiO<sub>2</sub> electrodes.<sup>218</sup> Sustained water oxidation electrocatalysis was observed over a 13 h period for 15 in 1.0 M HClO<sub>4</sub> with an external bias of 1.8 V vs NHE (Figure 30). Both the percentage

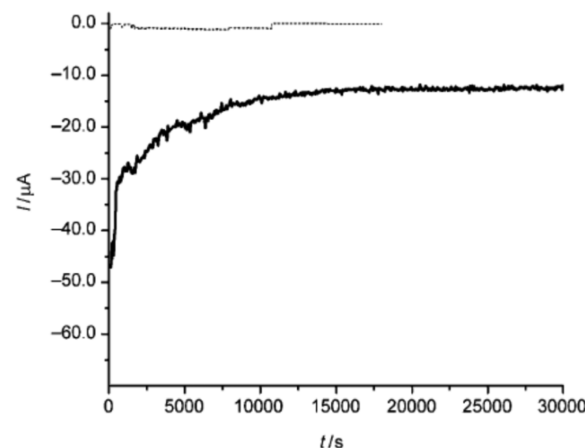


**Figure 30.** Current–time profile for water oxidation electrocatalysis by assembly 15 on planar ITO electrode (solid line) compared to the electrode background (dashed line) at 1.8 V vs NHE in 1.0 M HClO<sub>4</sub>: 8900 turnovers at a TOF of 0.6 s<sup>-1</sup>; current density 6.7  $\mu\text{A cm}^{-2}$ ;  $\Gamma = 7 \times 10^{-10}$  mol  $\text{cm}^{-2}$ . Reprinted with permission from ref 218. Copyright 2009 Wiley-VCH Verlag GmbH & Co.

Faradaic efficiency for oxygen production of 98%, as measured by gas chromatography, and catalyst longevity without decomposition were impressive. The results of CV studies on 15 and 18 were consistent with earlier observations on the mechanism of water oxidation by related single-site catalysts.<sup>33–35</sup>

Controlled potential electrolysis of layer-by-layer assembly 30 in 0.1 M HClO<sub>4</sub> at 1.7 V vs NHE for 2.7 h (9800 s) was shown by GC measurements to give O<sub>2</sub>.<sup>328</sup> Sustained water oxidation electrocatalysis was also observed for electro-assembly 30 at pH 4.7 in 0.1 M NaOAc/HOAc, 0.5 M in NaClO<sub>4</sub>. The TOF for water oxidation was 0.046 s<sup>-1</sup> (based on

oxygen production), with a TON of 501 and percentage Faraday efficiency of 77%. There was no catalyst decomposition after the 2 h electrolysis period, although complete decomposition of the chromophore was observed (Figure 31).<sup>165</sup> Long-term stability of surface binding at the higher pH was a notable advantage of the electropolymerization/electro-assembly strategy used to prepare the assembly.<sup>165,166</sup>

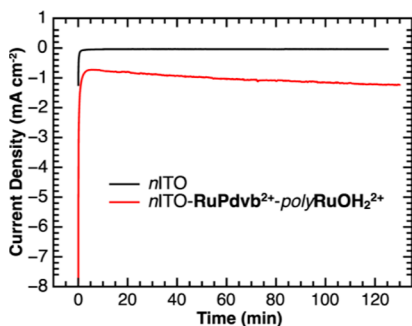


**Figure 31.** Current–time trace for electro-assembly 30 on nanoITO (nITO-RuPdvb<sup>2+</sup>-polyRuOH<sub>2+</sub>, red line) compared to the undervatized electrode at pH 4.7 (0.1 M NaOA/HOAc, 0.5 M NaClO<sub>4</sub>) at 1.7 V vs NHE. Reprinted with permission from ref 165. Copyright 2014 American Chemical Society.

Because they undergo rapid electron-transfer self-exchange with low electron-transfer barriers, [Ru(bpy)<sub>3</sub>]<sup>3+/2+</sup> and related [Ru(bpy)<sub>2</sub>(N-N)]<sup>3+/2+</sup> (N-N = 2,2'-bipyrimidine (bpm) or 2,2'-bipyrazine (bpz)) couples can act as redox mediators in enhancing rates of water oxidation. The redox mediator effect has its origin in enhancing slow electron-transfer steps in catalyst activation cycles. Mediator-assisted water oxidation was observed for the ruthenium “blue dimer” *cis,cis*-[(bpy)<sub>2</sub>(H<sub>2</sub>O)-RuORu(OH<sub>2</sub>)(bpy)<sub>2</sub>]<sup>4+</sup>, Figure 32, with 30 equiv of added

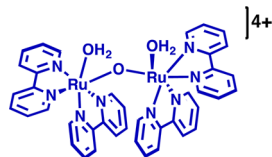


**Figure 32.** Structure of the ruthenium “blue dimer” *cis,cis*-[(bpy)<sub>2</sub>(H<sub>2</sub>O)RuORu(OH<sub>2</sub>)(bpy)<sub>2</sub>]<sup>4+</sup>.

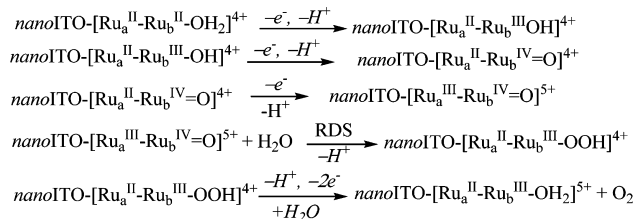
Ce(IV).<sup>216</sup> With the mediators [Ru(bpy)<sub>2</sub>(bpm)]<sup>2+</sup> and [Ru(bpy)<sub>2</sub>(bpz)]<sup>2+</sup>, rate enhancements of up to 30 were observed for water oxidation catalysis.<sup>216</sup> A related result was obtained by [Ru(bpy)<sub>3</sub>]<sup>3+</sup> formed by oxidative quenching of [Ru(bpy)<sub>3</sub>]<sup>2+\*</sup> by persulfate.<sup>216,265,298,341</sup>

The redox mediator effect has also been demonstrated for chromophore–catalyst assemblies with Ru(II)–polypyridyl chromophores. Water oxidation catalysis by solution assembly 6 with Ce(IV) as the oxidant is enhanced by a factor of 6 compared to that by the related single-site catalyst (Figure 24).<sup>33,298</sup> For 14 surface-bound to planar ITO, sustained water oxidation catalysis was observed at 1.43 V vs NHE in 0.1 M HNO<sub>3</sub>, in contrast to the single-site analogue, [Ru(tpy)(bpm)-(OH<sub>2</sub>)]<sup>2+</sup> (tpy = 2,2':6',2"-terpyridine), which has an onset of water oxidation at ~1.6 V vs NHE.<sup>218</sup>

The results of a detailed electrochemical investigation on water oxidation by assembly 18 (Figure 28, also called [Ru<sub>a</sub><sup>II</sup>-Ru<sub>b</sub><sup>II</sup>-OH<sub>2</sub>]<sup>4+</sup>) surface-bound to nanoparticle ITO (Sn-doped

indium oxide; nanoITO) in acidic solution led to the mechanism in Scheme 2.<sup>265</sup> As noted in Section 3.7, sequential

### Scheme 2. Scheme for Water Oxidation by Assembly 18



PCET 1e<sup>-</sup>/1H<sup>+</sup> oxidation of the catalyst in the assembly to -Ru<sub>b</sub><sup>IV</sup>=O<sup>2+</sup>, followed by further 1e<sup>-</sup> oxidation of the chromophore to give -[Ru<sub>a</sub><sup>III</sup>-Ru<sub>b</sub><sup>IV</sup>=O]<sup>5+</sup>, is sufficient to initiate water oxidation. Rate-limiting O–O bond formation occurs by O-atom transfer to a water molecule, in concert with electron transfers to both -Ru<sub>a</sub><sup>III</sup>- and -Ru<sub>b</sub><sup>IV</sup>=O by EAPT. In DSPEC applications, reaching the reactive form of the catalyst at the 3e<sup>-</sup>/2H<sup>+</sup> stage is essential because loss of the Ru(II) in chromophore -[Ru<sub>a</sub><sup>III</sup>-Ru<sub>b</sub><sup>IV</sup>=O]<sup>5+</sup> obviates further light-driven excitation/activation cycles.

### 7. ASSEMBLY INTERFACIAL DYNAMICS

There is an extensive literature on interfacial dynamics following photoexcitation of molecular chromophores adsorbed or chemically bound to metal oxide semiconductors.<sup>268,134,135,137,200,342–360</sup> The majority of these studies have investigated electron injection into TiO<sub>2</sub>, with emphasis on chromophores used in DSSC applications.<sup>354,361–364</sup> Interfacial dynamics in DSPEC devices are inherently more complex involving both chromophores for light-harvesting and catalysts for water oxidation (or CO<sub>2</sub> reduction). Multiple light absorption/injection events are required to generate the multiple redox equivalents for the solar fuel half-reactions.

In these studies, significant challenges arise from conducting measurements that extend over many time scales from femtoseconds to milliseconds. The results of these investigations have provided experimental insight into excited-state injection, BET, and, to a lesser extent, intra-assembly electron transfer activation of the catalyst.<sup>24,268,269,331</sup> They rely on short-pulse (femtoseconds to nanoseconds) excitation, utilization of characteristic spectral features, global analysis of complex spectra that evolve with time, and what are often complex kinetic analyses arising from competing processes and the heterogeneous nature of the assembly oxide interface.

#### 7.1. Kinetic Scheme

A kinetic scheme illustrating the sequence of events that occurs following chromophore excitation in a chromophore–catalyst assembly bound to an n-type semiconductor oxide—TiO<sub>2</sub>, SnO<sub>2</sub>—is shown in Figure 33. It is based on the results of transient absorbance measurements on a variety of chromophore–catalyst assemblies. It illustrates the photophysical events and following chemical reactions that occur upon excitation and injection by the chromophore. It follows the progression of four photon events through a complete cycle for DSPEC water oxidation. The scheme is generic, consistent with the known 4e<sup>-</sup>/4H<sup>+</sup> mechanism for water oxidation by surface-bound assemblies, but the details are assembly specific. To date, only the dynamic events that occur following the initial two

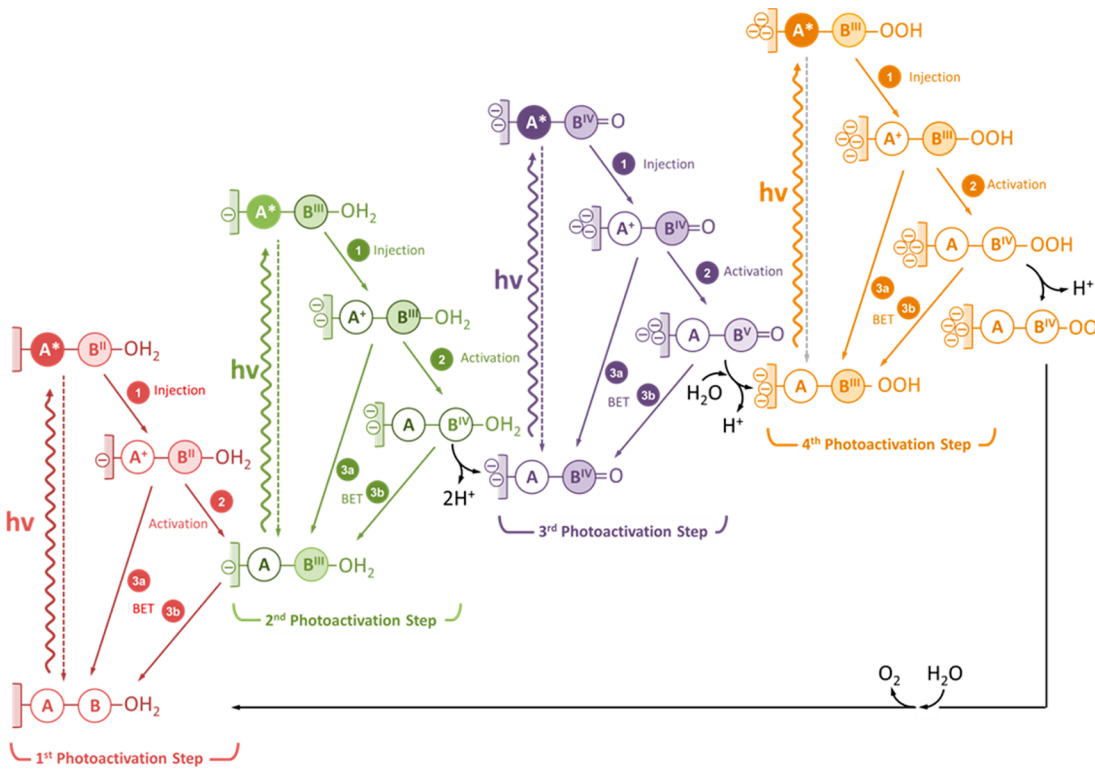


Figure 33. Kinetic scheme illustrating the dynamic processes that occur in photoactivated water oxidation at a DSPEC photoanode.

photon excitation events have been studied in detail and, more typically, only the first.

The kinetic scheme highlights key events in single-photon activation and in photoactivation of a DSPEC for water oxidation. It builds on the introduction to DSPEC dynamics in Section 3 and illustrates a number of important points:

- Maximizing efficiencies requires maximized light absorption and efficient injection followed by rapid intra-assembly or cross-surface electron-transfer activation of the catalyst, all before BET can occur.
- Four excitation/injection/catalyst activation cycles are required. For each there is a competition between activation/water oxidation and BET.
- The rate-limiting step in water oxidation cycles is typically O---O bond formation, which occurs at the  $3e^-/2H^+$  or  $2e^-/2H^+$  stage.
- Because of the slow rate of solar insolation of  $\sim 2\text{ s}^{-1}$  in the Vis region of the spectrum, the millisecond to microsecond time scale for BET on  $TiO_2$ , and the need to accumulate multiple oxidative equivalents at the catalyst, core/shell or related structures are required to control interfacial electron-transfer dynamics.
- High efficiencies require rapid water oxidation, with the DSPEC efficiency directly dependent on the rate of solar insolation.

## 7.2. Kinetic Efficiencies

Neglecting factors dictating long-term performance in an operating DSPEC—pH gradients, gas handling, etc.—DSPEC cell efficiencies are dictated by local microscopic dynamics. The per-photon-absorbed efficiency for completion of the first photoactivation step ( $\eta_1$ ) is given by eq 33, with  $F_{h\nu}$  the fraction of photons absorbed by the chromophore at the excitation wavelength,  $\Phi_{inj}$  the overall electron injection efficiency, and

$$\eta_1 = F_{h\nu}(\Phi_{inj}\Phi_{ET}) \quad (33)$$

$\Phi_{ET}$  the efficiency of transferring the oxidative equivalent to the catalyst. In the evaluation of  $\Phi_{inj}$  for a series of Ru(II) polypyridyl assemblies, the intensity of a 375 nm absorption feature to the ground-state bleach on  $TiO_2$  has been compared to  $ZrO_2$  on which injection does not occur.<sup>187</sup> Values for  $\eta_1$  have been evaluated for assemblies **20** ( $\eta_1 = 0.43$ ),<sup>365</sup> **19** ( $\eta_1 = 0.49$ ),<sup>301</sup> and **17** ( $\eta_1 = 0.66$ ).<sup>268</sup> In all three cases, intra-assembly transfer of the oxidative equivalent after injection (<500 ps) is significantly more rapid than BET (microseconds to milliseconds) with  $\Phi_{ET} \approx 1$ , as determined by kinetic modeling.<sup>187,301,371</sup>

Light absorption by the catalyst is typically nonproductive, leading to rapid excited-state nonradiative decay and low injection efficiencies.<sup>268,365</sup> For Ru(II)-polypyridyl catalysts, competitive catalyst light absorption can noticeably decrease  $\Phi_{inj}$  for the first photoactivation step by competitive light absorption, as observed by TA measurements. For assembly **17**, with a 1:1 chromophore:catalyst ratio, the fraction of photons absorbed by the catalyst at laser excitation wavelengths in the region 415–425 nm varies from 15% to 25% for assemblies **17**, **19**, and **20**,<sup>268</sup> with  $F_{h\nu} = 0.75–0.85$ . The fraction of absorbed photons is evaluated from normalized ground-state absorption spectra and the ratio of chromophore to catalyst absorbance at a defined excitation wavelength, as described elsewhere.<sup>187,301,371</sup> Competitive catalyst light absorption past the first photoactivation step for these assemblies is insignificant because of the loss of the Ru(II)-based MLCT transitions upon oxidation to Ru(III) and past Ru(III) to the higher oxidation states. An additional advantage of “antenna” assemblies with multiple chromophores and efficient antenna dynamics, Section 3.3, is the minimization of competitive catalyst light absorption.

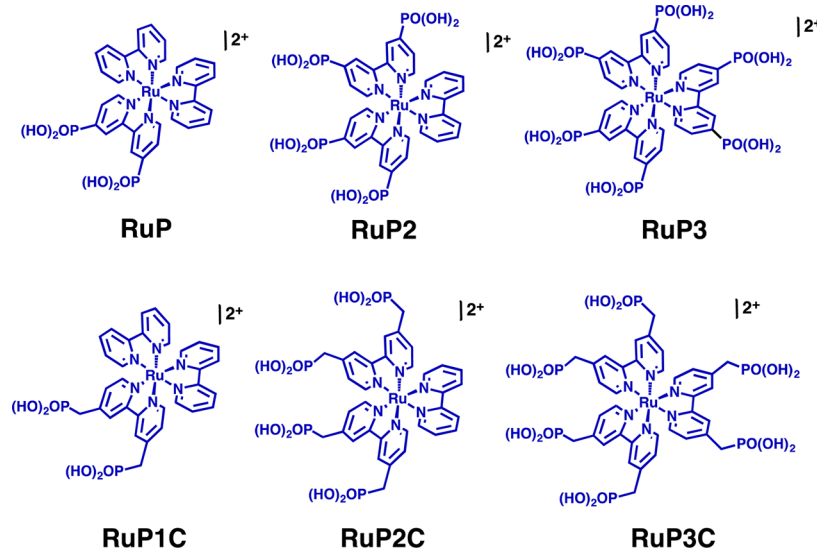


**Figure 34.** Phosphonate-derivatized Ru(II)–polypyridyl chromophores.

### 7.3. Electron Injection

Electron injection has been investigated for organic, porphyrin, and Ru(II)–polypyridyl chromophores of relevance to DSSC and DSPEC applications.<sup>347,366–372</sup> As noted in Section 3.7, for Ru(II)–polypyridyl chromophores (Figure 34), both direct light-driven<sup>201</sup> and excited-state injection have been observed, with the latter dominating.<sup>196,344,346,347,352,373</sup>

Moran and co-workers have investigated direct electron injection into TiO<sub>2</sub> (Figure 35), observing the coupling of

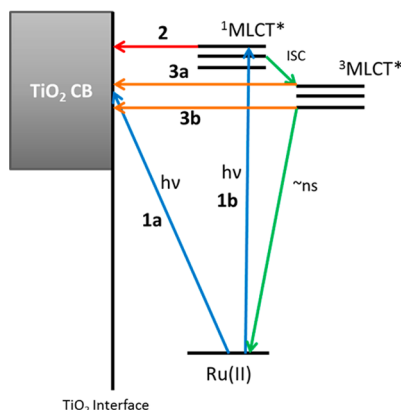


**Figure 35.** Illustration of injection into TiO<sub>2</sub> following MLCT excitation of a Ru(II)–polypyridyl chromophore, illustrating direct optical injection (1a), injection by <sup>1</sup>MLCT (2), and injection by vibrationally excited <sup>3</sup>MLCT (3a), or relaxed <sup>3</sup>MLCT (3b).

surface vibronic modes for both RuP<sup>2+</sup> (Figure 26) and catechol by using femtosecond transient grating spectroscopy.<sup>201</sup> Catechol is strongly coupled to the semiconductor electronically, with substantial delocalization of the excited-state wave function over both the molecule and the TiO<sub>2</sub> nanoparticle surface. Excited-state electronic coupling to the surface for RuP<sup>2+</sup> is considerably less, but evidence for direct injection was obtained by Raman measurements.<sup>201</sup>

As noted in Section 3.4, and as illustrated in Figure 35, multi-step injection occurs by complicated, multi-exponential ultrafast and picosecond time scale kinetics. Rapid injection occurs from the initially formed singlet state, <sup>1</sup>MLCT, in competition with

rapid (<200 fs) intersystem crossing to the lowest triplet, <sup>3</sup>MLCT. Rapid injection also occurs from initially formed <sup>3</sup>MLCT states before vibrational relaxation occurs. Slower injection, 10–100 ps, occurs from a distribution of thermally equilibrated triplet states.<sup>196,346,348,374–378</sup>

An extensive study of excited-state injection by the phosphonic acid-derivatized chromophores in Figure 34 by TA and transient grating measurements was recently completed in 0.1 M HClO<sub>4</sub> from tens of femtoseconds to hundreds of picoseconds. The time dependence for the decrease in the  $\pi \rightarrow \pi^*(\text{bpy}^{\bullet-})$  excited-state absorption feature at 380 nm following laser excitation is shown for three of the complexes in Figure 36. The loss of absorption in this region, without loss of the ground-state bleach at 460 nm, provides a signature for electron injection from the MLCT excited state.<sup>268</sup> Injection kinetics are biexponential and ligand dependent, with rapid injection by –RuP<sup>2+</sup> having time constants of 7.5 and 69 ps. In accounting for the trends in the data, there was no need to invoke rate-limiting

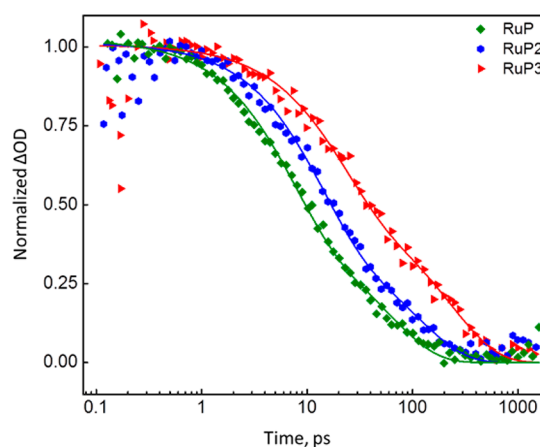


**Figure 36.** Kinetic traces and multi-exponential fits monitored at the  $\pi \rightarrow \pi^*(\text{bpy}^{\bullet-})$  maximum at 380 nm for –RuP<sup>2+</sup> (green diamonds), –RuP2<sup>2+</sup> (blue circles), and –RuP3<sup>2+</sup> (red triangles) from 500 fs to 1.2 ns after laser excitation on 1–3 μm TiO<sub>2</sub> slides in deaerated 0.1 M HClO<sub>4</sub>. The data illustrate a decrease in injection rate with increasing number of phosphonic-ACID-derivatized ligands.

dipole rotation from MLCT states remote from the surface to the interface, e.g.,  $-\text{PRu}^{\text{III}}\text{P}^{2+*} \rightarrow -\text{P}^*\text{Ru}^{\text{III}}\text{P}^{2+*}$ , followed by injection.<sup>349,351</sup> Rather, injection rates were found to be consistent with the Marcus–Gerischer interfacial electron-transfer model, with the rate constants dictated by the density of states at the semiconductor surface and the reduction potential of the excited-state chromophore.

#### 7.4. Assembly Injection

The assembly strategies in Figures 28 and 29 link chromophore and catalyst in structures that facilitate intra-assembly electron transfer. In both, modification of the bpy bridging ligand affects injection efficiencies on TiO<sub>2</sub>. With the benzamide link in 17 the injection efficiency is relatively unaffected, decreasing to 90% from 95% for  $-\text{RuP2C}^{2+}$ .<sup>266,268</sup> For the layer-by-layer, Zr(IV)-bridged structure in assembly 20, the injection efficiency is ~80% compared to ~100% for RuP2<sup>2+</sup>.<sup>365</sup> For the amide functionalized peptide in assembly 19, the injection efficiency is ~70%.<sup>379</sup> For assembly 16, the lowest MLCT excited state is localized on the bridging ligand, energetically stabilized and directed away from the interface, resulting in a decrease in injection efficiency to 17%.

The nature of the link can also affect electron injection dynamics. For assembly 17, injection from the thermally equilibrated excited state occurs with  $\tau_3 = 540$  ps, compared to the control chromophore with  $\tau_3 = 255$  ps.<sup>268</sup> For assembly 23, an increase in the injection rate occurs in concert with a decrease in injection yield due to the ion-paired, negatively charged polyoxometalate (POM) catalyst. Hill and co-workers attribute this difference to suppression of injection from the <sup>3</sup>MLCT state of RuP<sup>2+</sup> due to a change in the conduction-band edge of TiO<sub>2</sub> induced by the POM catalyst.<sup>334</sup>

As noted above, the majority of studies to date on assemblies bound to TiO<sub>2</sub> have concentrated on the dynamic events following initial one-photon excitation of the assembly, for the Ru(II)–polypyridyl-based assemblies, such as  $-\text{[Ru}^{\text{II}}\text{--Ru}^{\text{II}}\text{--OH}_2]^{\text{4+}}$ . In these assemblies, a series of potential intra-assembly photochemical events also exist which, in principle, can compete with injection, leading to decreased injection yields. In assemblies with accessible low-lying excited states on the catalyst, both MLCT and metal-centered dd states for Ru(II)–polypyridyl complexes, a competing process is intra-assembly energy transfer,  $\text{TiO}_2|-\text{[Ru}^{\text{II}*}\text{--Ru}^{\text{II}}\text{--OH}_2]^{\text{4+}} \rightarrow \text{TiO}_2|-\text{[Ru}^{\text{II}}\text{--(Ru}^{\text{II}}\text{--OH}_2)^{*}]^{\text{4+}}$ . For the singly oxidized assembly,  $\text{TiO}_2|-\text{[Ru}^{\text{II}}\text{--Ru}^{\text{III}}\text{--OH}_2]^{\text{5+}}$ , there is competition from intra-assembly electron transfer,  $\text{TiO}_2|-\text{[Ru}^{\text{II}*}\text{--Ru}^{\text{III}}\text{--OH}_2]^{\text{5+}} \rightarrow \text{TiO}_2|-\text{[Ru}^{\text{III}}\text{--Ru}^{\text{II}}\text{--OH}_2]^{\text{5+}}$  and, potentially, from energy transfer to low-lying excited states on the oxidized catalyst.

#### 7.5. Electron-Transfer Activation of the Catalyst

There are only limited data on electron-transfer activation of the catalyst following injection, and interpretation of data that are available is complicated by overlapping processes and convoluted dynamics.<sup>268</sup> In assembly 23, with the catalyst electrostatically bound, intra-assembly electron-transfer oxidation of the catalyst was monitored by recovery of the ground-state bleach for surface-bound  $-\text{RuP}^{3+}$ .<sup>334</sup> In assemblies that have both Ru(II)–polypyridyl chromophore and catalyst, 17, 19, and 20,<sup>268,365,379</sup> the catalyst activation step is difficult to discern because of spectral overlap between TA and bleach features.<sup>268,365,379</sup>

The significant spectral overlap between chromophore and catalyst in these assemblies, with the  $\lambda_{\text{max}}$  of each component differing by only tens of nanometers, prevents the quantitative

evaluation of rate information for intra-assembly electron transfer by single-wavelength kinetics. TA spectra evolve as contributions appear in the transients due to the oxidized catalyst. Because the ground-state bleach of the catalyst is red-shifted from the chromophore bleach, intra-assembly electron transfer can be monitored qualitatively by plotting the change in wavelength at the red edge of the ground-state bleach over a 1 ns interval, as shown in Figure 37. Assemblies 19 and 20 exhibit a dramatic change in the red edge of the bleach compared to the chromophore alone.

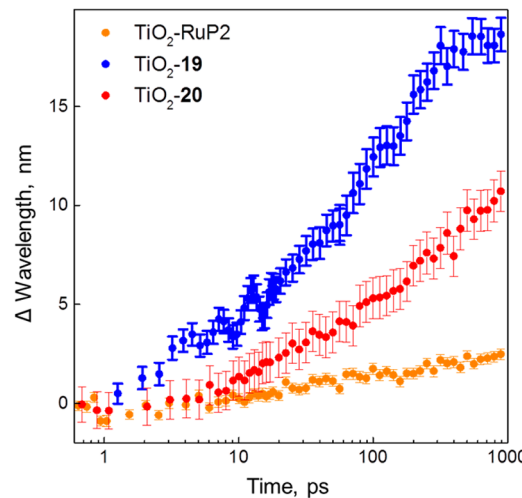


**Figure 37.** Illustration of red-shifts in bleach minima with time for  $-\text{RuP}^{2+}$  (orange) and assemblies 19 (blue) and 20 (red) on TiO<sub>2</sub> in deaerated 0.1 M HClO<sub>4</sub> at 22 °C, with the latter arising from intra-assembly oxidation of the catalyst following injection.

The analysis illustrated in Figure 37, while useful for ascertaining whether or not electron transfer has occurred, is not useful for obtaining quantitative rate information. For quantitative evaluation of the time dependence of the spectral traces, kinetic modeling based on singular value decomposition (SVD) of the data can be applied.<sup>187,371,384</sup> With SVD analysis, lifetimes for intra-assembly electron transfer ( $\tau_{\text{intra}}$ ) were found to be 145, 380, and 170 ps for assemblies 17, 19, and 20, respectively, in 0.1 M HClO<sub>4</sub>.<sup>268,365,379</sup> The decrease for 19 was attributed to the increased distance between chromophore and catalyst along the oligoproline helix.<sup>379</sup> Percentage electron-transfer efficiencies for assemblies 17 and 20 were ~100%, and ~49% for 19, with a contribution to the latter from an inactive Ru<sup>IV</sup>(OO) form of the catalyst. For assembly 23,  $\tau_{\text{intra}} = 102$  ps based on ground-state bleach kinetics.<sup>331</sup>

Experiments are currently underway to map the injection/intra-assembly electron-transfer dynamics from the initial  $-\text{[Ru}^{\text{II}}\text{--Ru}^{\text{II}}\text{--OH}_2]^{\text{4+}}$  state to  $-\text{[Ru}^{\text{II}}\text{--Ru}^{\text{IV}}=\text{O}]^{\text{4+}}$  for assemblies 17 and 18.<sup>126,266,268</sup> Excitation and injection of the latter to give  $-\text{[Ru}^{\text{III}}\text{--Ru}^{\text{IV}}=\text{O}]^{\text{5+}}$  will be used to trigger the O–O bond-forming step, Figures 17 and 18.

#### 7.6. Back Electron Transfer (BET)

BET has been extensively investigated in DSSCs by transient absorbance measurements.<sup>380</sup> At TiO<sub>2</sub>, there are kinetically competing regimes between electron transfer at the interface and internal electron-transfer dynamics within the semiconductor. Kinetics are characteristically complex, with dynamic events occurring on time scales from microseconds to milliseconds, with BET dominated by internal electron-

transfer dynamics within the semiconductor.<sup>350,356,381,350,382,322–324</sup> The injected electron localizes in “trap states”, initially at a localized surface or near surface state, followed by transfer to deeper trap states within the individual nanoparticles. Back electron transport to the surface occurs by electron hopping from trap state to trap state to a surface state from which BET occurs.

A variety of physical models have been proposed to describe intraparticle electron transport to the interface.<sup>380,383–385</sup> In one, electron transport occurs by electron tunneling between trap states, ultimately to a surface state. Rate-limiting tunneling has been shown to be physically implausible since the transit times between states ( $>\mu\text{s}$ ) are longer than the time scale for BET.<sup>380</sup> A second model assumes that electron transport occurs as a continuous-time random walk. In this model, illustrated in Figure 38, electrons occupying deep trap states undergo

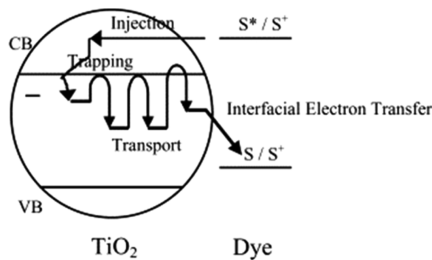


**Figure 38.** Illustration of the trapping/detrapping mechanism for electron transport in an oxide semiconductor following excitation and injection by excited state  $\text{S}^*$ .<sup>354</sup> Reprinted with permission from ref 354. Copyright 2004 Elsevier Publishing.

multiple cycles of thermally activated trapping/detrapping until the electron reaches a state near the surface.<sup>356,380</sup> In another model, electron transport is described as occurring by a hopping mechanism, with transfer between localized states near the conduction-band edge ultimately reaching the surface.<sup>383</sup> Thermal activation is required for the trapped electrons to populate the conduction band for transfer to the surface.

Regardless of the model used, the ensemble-averaged kinetics are complex due to the inherently variable number of trajectories, varying number of steps, and large number of associated single-step rate constants in the recombination process. Hole migration of the oxidized dye along the oxide surface can also play a role.<sup>200,386</sup> A number of mathematical treatments have been used to describe the kinetics, including a tri-exponential function and an expression derived from a sum of first- and second-order processes. In another, the time-dependent data have been treated by using the Kohlrausch–Williams–Watts (KWW) distribution function, eq 34. It is

$$k_{\text{KWW}} = \left[ \frac{1}{k_{\text{obs}} \beta} \Gamma\left(\frac{1}{\beta}\right) \right]^{-1} \quad (34)$$

based on a superposition of first-order reactions, each with a unique rate constant, assuming an exponential distribution.<sup>387</sup> As shown in eq 35, in this treatment of the data the fractional

$$\frac{\Delta \text{Abs}(t)}{\text{Abs}_0} = \exp[-(k_{\text{obs}} t)^\beta] \quad (35)$$

absorbance change with time,  $\text{Abs}(t)/\text{Abs}_0$ , varies with a rate constant,  $k_{\text{obs}}$ , and distribution width,  $\beta$ , with the latter varying from 0 to 1. In the limit that  $\beta = 1$ , the kinetics are first-order. The representative rate constant for the distribution,  $\langle k_{\text{KWW}} \rangle$ , is defined in eq 34, with  $\Gamma(1/\beta)$  the gamma function, eq 36.

$$\Gamma(n) = \int_0^\infty x^{n-1} e^{-x} dx = \frac{1}{n} \prod_{m=1}^{\infty} \frac{(1 + 1/m)^n}{1 + 1/m} \quad (36)$$

Equation 34 is appealing in that a wide range of dispersive kinetics can be modeled with only two adjustable parameters,  $k_{\text{KWW}}$  and  $\beta$ , which may or may not provide physical insight.<sup>388,389</sup>

As discussed in Section 3, rates for injection and BET to a surface-bound molecule or assembly depend on the density of acceptor or donor levels in the oxide. The density of levels varies with the semiconductor and conduction-band energy and can be modulated by applying a negative bias to increase the population density of electrons in the conduction band.<sup>390,391</sup> BET is also light-intensity-dependent, increasing with the number of injection events per semiconductor nanoparticle.<sup>135,391</sup> With high electron populations, the density of electrons in trap states near the conduction band increases, enhancing electron transport. Electron transport through the oxide remains rate-limiting under these conditions but can be significantly enhanced as the light intensity is increased.

Figure 39 illustrates the distribution of trap states in  $\text{SnO}_2$  and  $\text{TiO}_2$ .<sup>137</sup> The conduction band for  $\text{SnO}_2$  is more positive

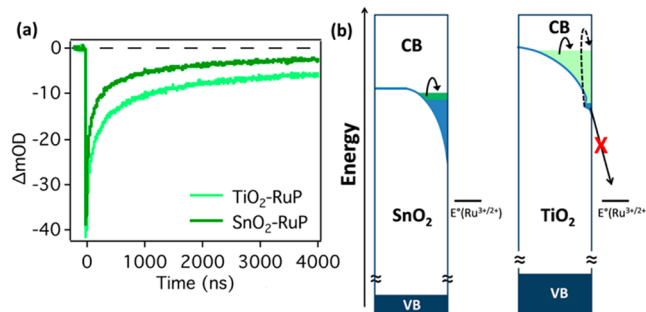


**Figure 39.** (a) Comparison of back electron transfer kinetics for  $\text{SnO}_2(\text{e}^-)-\text{RuP}^{3+}$  and  $\text{TiO}_2(\text{e}^-)-\text{RuP}^{3+}$ . (b) Density-of-state distributions for the two oxides, illustrating the effect of the narrower distribution of trap states for  $\text{SnO}_2$  and its effect on BET. Reprinted with permission from ref 137. Copyright 2013 American Chemical Society.

than that for  $\text{TiO}_2$  by 0.4 V, with a narrower distribution of trap states.<sup>134</sup> The narrower distribution decreases the number of sites to be traversed, and BET is more rapid by a factor of 2–3 for  $\text{SnO}_2(\text{e}^-)-\text{RuP}^{3+}$  compared to  $\text{TiO}_2(\text{e}^-)-\text{RuP}^{3+}$ .<sup>137</sup> As on  $\text{TiO}_2$ , BET on  $\text{SnO}_2$  is rate-limited by intra-oxide dynamics, with variations in driving force having a negligible effect.<sup>350,382</sup>

Because of the complexity of BET kinetics, absorbance–time data are often reported as the  $t_{1/2}$ , the time for half of the overall absorbance change to occur. Values of this parameter are listed in Table 2 for assemblies 16–20.<sup>126,266,268,269,365,379</sup> For assembly 16, values are reported for BET to both  $-[\text{Ru}^{II}-\text{Ru}^{III}-\text{OH}_2]^{5+}$  and  $-[\text{Ru}_a^{II}-\text{Ru}_b^{IV}=\text{O}]^{4+}$  following excitation and injection. The significantly decreased value of  $t_{1/2} = 0.76 \mu\text{s}$  for assembly 20 suggests that BET is largely dictated by

**Table 2.** Back Electron Transfer Half-Times ( $t_{1/2}$ ) in Daeerated 0.1 M HClO<sub>4</sub> at 22 °C with 420 nm Excitation

assembly	$\tau_{1/2}$ (μs) for BET
16	8.4 ( $\text{TiO}_2(\text{e}^-) \rightarrow -[\text{Ru}^{\text{II}}-\text{Ru}^{\text{III}}-\text{OH}]^{5+}$ ) 3.6 ( $\text{TiO}_2(\text{e}^-) \rightarrow -[\text{Ru}^{\text{II}}-\text{Ru}^{\text{IV}}=\text{O}]^{4+}$ )
17	6.7
19	~ 1
20	0.76

electron transfer from  $\text{TiO}_2(\text{e}^-)$  to the remote catalyst site in the ion-paired assembly.<sup>365</sup>

Although BET on  $\text{TiO}_2$  is dominated by electron transport dynamics within the oxide, recent studies on injection and BET on nanoITO show that electron transport within the oxide is rapid with interfacial BET rate-limiting. The results of a bias dependence study on BET on nanoITO have been shown to be consistent with Marcus–Gerischer theory.<sup>187</sup>

## 8. DSPEC WATER SPLITTING

### 8.1. Introduction

The origin of the DSPEC concept came from early experiments which demonstrated that oxidative quenching of the MLCT excited state of  $\text{Ru}(\text{bpy})_3^{2+}$  by methyl viologen dication ( $\text{MV}^{2+}$ ) in solution, Section 3.1,  $\text{Ru}(\text{bpy})_3^{2+*} + \text{MV}^{2+} \rightarrow \text{Ru}(\text{bpy})_3^{3+} + \text{MV}^+$ , led to the transient redox products,  $\text{Ru}(\text{bpy})_3^{3+} + \text{MV}^+$ . In acidic solution, the separated products were capable of water oxidation and  $\text{H}^+$  reduction.<sup>303–306</sup> The integration of chromophore–catalyst assemblies with n-type semiconductor oxides— $\text{TiO}_2$ ,  $\text{SnO}_2$ —opened the door to a PEC approach to water splitting based on molecular-level light absorption, excited-state injection, electron-transfer activation, and multi-electron-transfer catalysis. The initial concepts behind DSPEC photoelectrochemical water oxidation were discussed in early reports on dye-sensitized  $\text{TiO}_2$  nanoparticles,<sup>101–103,106,107,188,392–397</sup> and the first molecular-based DSPEC, for dehydrogenation of isopropanol, was reported in 1999.<sup>320</sup> As illustrated in the diagram in Figure 6, in DSPEC water splitting, a chromophore–catalyst assembly is surface-bound to an n-type semiconductor or core/shell oxide. The derivatized oxide is the photoanode in a PEC cell, with a separate cathode for  $\text{H}_2\text{O}/\text{H}^+$  reduction to  $\text{H}_2$ , typically with a proton-exchange membrane to separate the gases and allow for pH equilibration.

The methodologies for evaluating DSPEC performance follow straightforwardly from those used to evaluate DSSC and semiconductor PEC devices, with additional demands arising from the need to monitor photoproducts, ideally in real time. Evaluation of DSPEC device performance is discussed in Section 9.

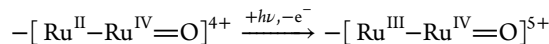
**8.1.1. Surface Binding and Stability.** Stability is a major consideration in DSPEC applications, with issues arising from both the stability of the assembly and its surface link to the oxide. In assembly 23, the interaction between chromophore and catalyst is electrostatic in nature. Desorption from the surface occurs rapidly, which greatly limits the time response of photocurrents under irradiation. Assemblies 16, 24, and 29 utilize surface carboxylate ester formation for surface-binding, and the resulting surfaces are unstable toward hydrolysis in aqueous solutions, especially at higher pH,<sup>154</sup> which greatly limits DSPEC performance.

As noted in Section 3.5, even phosphonate–oxide surface binding is unstable toward surface hydrolysis as the pH is

increased toward and beyond 7, typically with relatively rapid loss from the surface.<sup>136,154,155,160,398</sup> Strategies for stabilizing surface binding are available, Section 3.4.1, based on ALD of inert  $\text{Al}_2\text{O}_3$  or  $\text{TiO}_2$  overlayers,<sup>156–167,279,399,400</sup> solution deposition of hydrophobic polymeric overlayers,<sup>164</sup> formation of chemically stabilized networks by electro-assembly,<sup>165,401</sup> by use of siloxanes and other more stable surface binding links,<sup>136,155,402,403</sup> and by added hydrophobic groups to inhibit water or base penetration into the oxide surface.<sup>404</sup> The impact of ALD stabilization on extending DSPEC performance is impressive, with negligible loss from the surface even over periods of hours at higher pH with relatively high concentrations of added buffers,<sup>126</sup> and recent results with polymethylmethacrylate polymer overlayers are equally encouraging.<sup>164</sup>

**8.1.2. pH and Buffer Base Effects.** The thermodynamic potential for water oxidation decreases by 59 mV/pH unit from  $E^\circ = 1.23$  V at pH 0 to 0.82 V at pH 7 to 0.40 V at pH 14. Depending on the mechanism of water oxidation and its pH dependence, DSPEC photocurrents and efficiencies are typically enhanced at higher pH with added buffer bases. These are typically buffer base rather than pH effects with the addition of the base enhancing the rate of a slow step in the overall catalytic cycle, for the scheme in Figure 13 by enhancing the rate of the O–O bond-forming step and/or PCET oxidation of  $\text{Ru}^{\text{III}}-\text{OH}$  to  $\text{Ru}^{\text{IV}}=\text{O}$ , Section 3.8.

As an example, for assembly 18, the results of both DSPEC water splitting and electrocatalytic water oxidation are available.<sup>126,265</sup> Two sequential excitation/electro- transfer cycles lead to the twice-oxidized assembly  $-[\text{Ru}^{\text{II}}-\text{Ru}^{\text{IV}}=\text{O}]^{4+}$ , Scheme 2. However, water oxidation requires loss of an additional electron,



which is pH-independent. There is a buffer base dependence because O–O bond formation is catalyzed by added buffer bases by APT, Section 3.8.

By contrast, as noted in Section 3.7,  $2\text{e}^-/2\text{H}^+$  oxidation of  $[\text{Ru}^{\text{II}}(\text{tpy})(\text{bpz})(\text{OH}_2)]^{2+}$  gives  $[\text{Ru}^{\text{IV}}(\text{tpy})(\text{bpz})(\text{O})]^{2+}$ . The  $\text{Ru}^{\text{IV}}=\text{O}^{2+}$  form is thermodynamically capable of water oxidation from pH 0 to 14, with an overpotential of only 180 mV. In 1 M  $\text{PO}_4^{3-}$ , it undergoes APT water oxidation with  $t_{1/2} \approx 0.1$  s.<sup>405</sup> For water oxidation by  $\text{Ru}^{\text{IV}}=\text{O}^{2+}$ , the highest potential couple is pH-dependent. The potential required for water oxidation decreases with pH, with  $E^\circ = 0.85$  V to drive the catalyst couple at pH 11.

**8.1.3. Chromophore–Catalyst Stability.** In addition to surface binding, the chemical stability of chromophore–catalyst assemblies is a major issue in DSPEC applications. A systematic investigation of photochemical stability for the series of phosphonic-acid-derivatized Ru(II)–polypyridyl complexes in Figure 34, surface-bound to  $\text{TiO}_2$  and  $\text{ZrO}_2$ , revealed long-term instabilities arising from both desorption and ligand loss. Both processes were solvent- and pH-dependent, and both were influenced by  $\text{O}_2$ . The appearance of photosubstitution products provided evidence for MLCT excitation on the surface, followed by thermal population of low-lying dd states and ligand loss.<sup>136,154</sup>

There is evidence for long-term stability of Ru(II)–polypyridyl WOCs with catalytic cycles extended through tens of thousands of electrocatalytic water oxidation cycles.<sup>159,218,291</sup> The stability of the oxidized forms of analogous

chromophores is more problematic. The results of a systematic investigation on the instability of the oxidized form of  $-\text{RuP}^{2+}$ ,  $-\text{RuP}^{3+}$ , and related phosphonic acid Ru(II)–polypyridyl complexes on planar FTO electrodes in acid solution, with voltammetric monitoring, demonstrate that oxidation to Ru(III) results in a combination of slow desorption from the electrode and bpy ligand loss accompanied by aquation and/or anation.<sup>406</sup>

The instabilities that arise in the oxidized form of the chromophore can greatly limit the lifetime of DSPEC devices. The time scale for decomposition/desorption on the surface is related to the time spent in the oxidized form in the overall PEC cycle, for example, as  $-[\text{Ru}^{\text{III}}-\text{Ru}^{\text{IV}}=\text{O}]^{5+}$  for assembly 18. In a water oxidation cycle, the chromophore cycles through a  $4h\nu/4e^-$  sequence with an incident solar rate of  $1-2\text{ s}^{-1}$ . With water splitting rate limited by water oxidation and competing decomposition reaction slower by a factor of 100, 1% decomposition of the chromophore for each  $h\nu/e^-$  cycle would greatly limit assembly lifetime. Slow decomposition on this time scale, resulting in decreasing photocurrents, has been reported in a water splitting DSPEC based on assembly 18, even after ALD stabilization of surface binding.<sup>286</sup>

Chromophore instability is increasingly problematic at higher pH, where the instability of  $\text{Ru}(\text{bpy})_3^{3+}$  and related higher oxidation state polypyridyl complexes, arising from ligand hydrolysis and oxidation, is well documented. Under these conditions, sustained ligand decomposition can contribute significantly to observed photocurrents, and  $\text{O}_2$  measurements to verify water splitting are essential.<sup>108,407,408</sup> As noted in Section 3.6, the use of organic dyes in aqueous media under conditions used for water splitting is even more problematic, given the instability of organic cation radicals in aqueous solutions.

Avoiding oxidized chromophore decomposition is a major issue in the use of molecular assemblies in DSPEC applications. Stabilization strategies are currently under investigation, including surface stabilization by ALD or hydrophobic film overayers. Given the microscopic dynamics involved in the photoactivation process, another approach is to minimize the fraction of time in an activation cycle with the chromophore in an oxidized state. The strategy adopted by PSII in this regard is notable. In PSII, the oxidative equivalent initially localized on chlorophyll P<sub>680</sub> is transferred to adjacent Tyrosine Z by Tyr<sub>Z</sub>  $\rightarrow$  P<sub>680</sub><sup>+</sup> electron transfer, which occurs with  $\tau \approx 100$  ps.<sup>21,102,270–272</sup> Electron transfer in this case gives a more stable phenolic radical for later oxidative activation of the Mn<sub>4</sub>Ca WOC in the OEC.

Based on the microscopic dynamics for the covalently linked assemblies that have been investigated, excitation and injection are followed by rapid, sub-nanosecond transfer of oxidative equivalents to the WOC, an analogue of Tyr<sub>Z</sub><sup>•+</sup> oxidation of the OEC. The problem with decomposition arises at the  $-[\text{Ru}^{\text{III}}-\text{Ru}^{\text{IV}}=\text{O}]^{5+}$  stage, with slow water oxidation leading to a relatively long lifetimes for the chromophore in its oxidized state.

**8.1.4. Multi-Chromophore Advantage.** As noted in Section 3.6, under standard solar flux conditions, AM 1.5G, only  $\sim 2$  photons per second are absorbed per chromophore per assembly in the Vis and near-IR regions of the spectrum, limiting the rate of water oxidation to  $\sim 0.5\text{ s}^{-1}$ . In natural photosynthesis, hundreds of chlorophylls and ancillary pigments absorb light in the Vis and funnel the resulting excited-state energy rapidly and with high efficiency to the reaction

center and a single Mn<sub>4</sub>Ca cluster in the OEC.<sup>21,23,409</sup> The OEC undergoes relatively rapid oxidative activation and catalysis, with  $\text{O}_2$  evolved after the absorption of four photons. As noted in Section 3.6, the “antenna” effect in PSII has the advantage of enhancing the net rate of solar insolation and the rate of water oxidation, from seconds in ambient sunlight to milliseconds. In the limit of fast water oxidation catalysis, a similar advantage could exist for DSPECs. Strategies are being explored with multiple chromophores linked to single catalysts based on polymer and peptide frameworks.<sup>165,176,322,410–415</sup> For this strategy to be effective requires both rapid water oxidation catalysis and rapid, efficient intra-assembly dynamics. For co-surface-loaded assemblies 24 and 27 and related structures, the key is efficient cross-surface electron transfer following injection, coupled to rapid water oxidation.<sup>290</sup>

**8.1.5.  $\text{O}_2$  Measurements.** In most laboratory-scale DSPEC measurements, the photocurrents generated are small—in the tens to hundreds of microamperes—and often transient, decaying with time due to the instability of the assembly, for example. In this limit, only small (micromole) amounts of  $\text{O}_2$  are generated, limiting the use of traditional techniques such as gas chromatography or Clark electrodes.<sup>288,331–333</sup> Mallouk and co-workers have developed an electrochemical procedure with a second, monitoring electrode held at a close, fixed distance from the photoanode. Evolved  $\text{O}_2$  is analyzed by voltammetric scans at the monitoring electrode by current measurements on the  $\text{O}_2/\text{O}_2^-$  couple at  $-0.46\text{ V}$  vs saturated calomel electrode (SCE).<sup>336</sup> The high sensitivity of these techniques allows for quantitative analysis of oxygen in real-time.

For  $\text{O}_2$  evolved by assembly 18, a modified version of the rotating ring-disk electrode (RRDE) technique developed by Murray and co-workers<sup>339,416,417</sup> has been reported.<sup>126</sup> In this DSPEC application, a nanoITO/TiO<sub>2</sub> core/shell oxide was spun-cast onto the disk of an RRDE and then derivatized with the surface-attached assembly. The  $\text{O}_2$  produced by photolysis of the rotating disk was detected by scanning the potential of the outer ring with current monitoring, Figure 40.

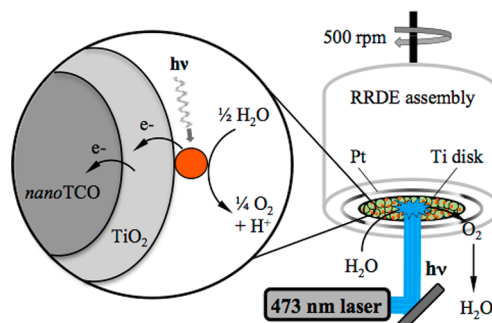
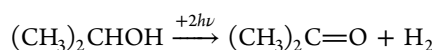


Figure 40. Illustration of a RRDE electrode modified for DSPEC oxygen detection with the chromophore–catalyst assembly shown as an orange ball. Reprinted from ref 126. Copyright 2013 Proceedings of the National Academy of Science.

**8.1.6. Initial Experiments: Related Results.** In 1999, the assembly 33 (Figure 41) on TiO<sub>2</sub> was shown to undergo photo-oxidation of isopropanol to acetone with  $\text{H}_2$  evolved at the cathode and the net reaction,<sup>320</sup>



Although photocurrents were low, incident photon-to-current efficiency (IPCE) measurements showed that the photoresponse followed the spectrum of the chromophore.

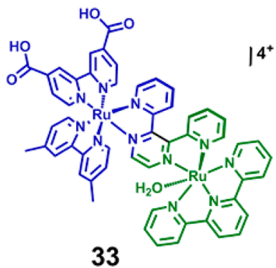
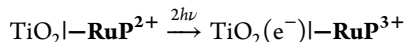


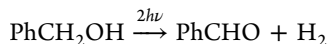
Figure 41. Structure of assembly 33.<sup>320</sup>

A model for H<sub>2</sub> generation in a DSPEC configuration was investigated with  $-\text{RuP}^{2+}$  surface-attached to TiO<sub>2</sub>, with triethanolamine or deprotonated EDTA (EDTA<sup>4-</sup>) added as reductive scavengers. With the added scavengers, excitation and injection,



was followed by chemical reduction of  $\text{TiO}_2(\text{e}^-)|-\text{RuP}^{3+}$  to  $\text{TiO}_2(\text{e}^-)|-\text{RuP}^{2+}$ , with  $k \approx 10^6 \text{ M}^{-1} \text{ s}^{-1}$ . The decrease in BET by reductive scavenging released injected electrons for H<sub>2</sub> production at the cathode.<sup>418</sup> For EDTA<sup>4-</sup> as the scavenger, electron collection efficiencies as high as 70% for H<sub>2</sub> production were obtained.

Light-driven dehydrogenation of benzyl alcohol to benzaldehyde,



was investigated in a DSPEC consisting of co-loaded surfaces of an excess of  $-\text{RuP}^{2+}$  and the catalyst  $[\text{Ru}(\text{Mebimpy})((4,4'-(\text{OH})_2\text{PO}-\text{CH}_2)_2\text{bpy})(\text{OH}_2)]^{2+}$ . Under steady-state photolysis conditions, a cross-surface pathway exists for building up  $\sim 10\%$  of the Ru<sup>IV</sup>=O form of the catalyst on the surface, which then oxidizes the alcohol to the aldehyde. On a nanoITO/TiO<sub>2</sub> core/shell electrode (see below) with optimized shell thickness, photocurrent enhancements of  $\sim 10$  were observed, with sustained absorbed photon-to-current efficiency (APCE) of 3.7%.<sup>419</sup>

## 8.2. Water Splitting by Chromophore–Catalyst Assemblies

In initial experiments demonstrating light-driven water splitting, Nafion film overlayers were utilized as an external medium to integrate catalysts with a chromophore surface-bound to TiO<sub>2</sub>, **24** and **25** in Figure 29. A report by Brimblecombe et al. described a photoanode for water oxidation with a 4.5:1 chromophore:catalyst ratio with the chromophore  $[\text{Ru}(4,4'-\text{COOH})\text{bpy})(\text{bpy})_2]^{2+}$  and the tetra-nuclear Mn-oxo cluster ( $[\text{Mn}_4\text{O}_4\text{L}_6]^+$  as oxidant with L = (MeOPh)<sub>2</sub>PO<sub>2</sub><sup>-</sup>) (**24**) in 0.1 M Na<sub>2</sub>SO<sub>4</sub>. The resulting PEC maintained sustained photocurrents under white light illumination (100 mW/cm<sup>2</sup>) over a 2 h period with *no external bias* and a TOF = 0.13 mol O<sub>2</sub> cluster<sup>-1</sup> s<sup>-1</sup> calculated from O<sub>2</sub> measurement by a Clark electrode.<sup>332</sup> The IPCE reached a highest value of 1.7% following MLCT excitation of the chromophore. Only a small decrease in the sustained photocurrent was observed over the 2 h period, likely due to desorption of chromophore and catalyst from the metal oxide surface. However, later X-ray absorption

spectroscopy and TEM measurements suggested that the  $[\text{Mn}_4\text{O}_4\text{L}_6]^+$  cluster merely acts as a precatalyst to generate Birnessite, a mixed Mn(III/IV) oxide which was suggested to be the active water oxidation catalysis.<sup>340,420</sup>

Hill and co-workers reported PEC water oxidation by ion-paired POM catalyst assembly **23** at pH 5.8 (30 mM NaSiF<sub>6</sub>) under 420–470 nm illumination (30 mW/cm<sup>2</sup>) with an APCE of 0.2%. Over the course of a 20 min experiment,  $\sim 40\%$  of the initial absorbance at 450 nm was lost due to chromophore and catalyst desorption from the surface (see Section 8.1.1).<sup>331</sup>

A photoanode based on co-loaded porphyrin chromophore–Ir(III) catalyst assembly **29** on TiO<sub>2</sub> was reported by Brudvig and co-workers.<sup>334</sup> Due to the relatively high potential for the Porphyrin<sup>+/1</sup>Porphyrin<sup>\*</sup> couple, excitation and injection were followed by oxidation of the precatalyst Ir<sup>III</sup>(Cp\*)(COOH-phy)(Cl) (Cp\* = cyclopentadienyl; COOH-phy = 3-(pyridin-2-yl)benzoic acid).<sup>228,229</sup> In 0.1 M Na<sub>2</sub>SO<sub>4</sub> with an applied bias of 0.497 V and 200 mW cm<sup>-2</sup> white light illumination (400 nm long-pass filter), assembly **29** maintained sustained photocurrents for 60 s, but with no information given concerning efficiencies or O<sub>2</sub> production.

The Sun group reported PEC water oxidation by assembly **25** at pH 7 in a phosphate buffer solution with an external bias of only  $-0.13$  V, with the catalyst supported in a Nafion overlayer. The catalyst underwent 16 turnovers in a 1 h period at a rate of 0.0044 s<sup>-1</sup> under illumination from a 500 W Xe lamp (400 nm long-pass filter), with photogenerated O<sub>2</sub> measured with a Clark electrode.<sup>333</sup> DSPEC water splitting was pH-dependent, with insignificant photocurrents at pH 1. The pH dependence was attributed to the pH dependence of the redox couples leading to catalyst activation. At pH 1,  $E^\circ' = 1.5$  V (vs NHE) for oxidation to the active form of the catalyst, which is higher than  $E^\circ' \approx 1.4$  V vs SCE for the  $-\text{RuP}^{3+/2+}$  couple. At pH 7, the potential for catalyst activation decreases to 0.98 V (vs NHE), making it accessible following excitation and injection by the chromophore. It is important to note that the proposed mechanism for this family of WOCs suggests that rate-limiting O–O bond formation is pH-independent.<sup>222</sup> No photophysical measurements were reported for either of the Nafion overlayer assemblies **24** or **25**.

The Sun group extended their DSPEC investigations to co-loaded assembly **27** on nanocrystalline TiO<sub>2</sub> and observed a buffer dependence.<sup>288</sup> At pH 6.8 in a phosphate buffer, electrocatalytic water oxidation by **27** occurs at the potential for the chromophore Ru<sup>III/II</sup> couple, showing that, following excitation and injection, the oxidized chromophore was capable of oxidizing the catalyst to its catalytically active form. A photoanode consisting of a 3:1 chromophore:catalyst ratio at pH 6.8 in a phosphate buffer underwent sustained photocurrents over a 500 s period with TON = 498 and TOF = 1 s<sup>-1</sup> with white light illumination (300 mW/cm<sup>2</sup>, 400 nm long-pass filter), with only a 0.2 V applied external bias. Faradaic efficiencies for O<sub>2</sub> and H<sub>2</sub> evolution, measured by gas chromatography, were 83% and 74%, respectively.

Enhanced photocurrents were observed for **27** with increasing pH in a phosphate buffer,<sup>288</sup> with the results consistent with base-dependent water oxidation and an APT pathway, Section 3.8.<sup>159,258,421</sup> As discussed above, in this pH range at low [OH<sup>-</sup>], there is no microscopic basis for utilizing the enhanced thermodynamic driving force arising from the more favorable water oxidation thermodynamics as the pH is increased.<sup>38,39,417,422</sup> In solutions at the same pH but with either phosphate or borate buffers, significantly enhanced

photocurrents were observed for phosphate compared to borate, note Figure 42. Given the difference in  $pK_a$  values of

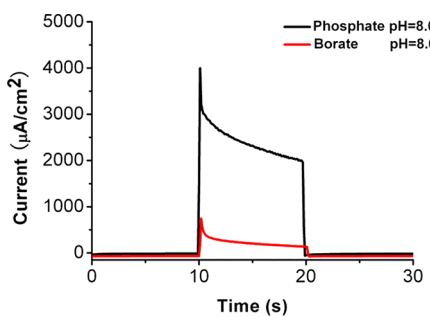


**Figure 42.** Photocurrents in a three-electrode cell assembly 27 on  $\text{TiO}_2$  as the photoanode in 0.1 M borate buffer (red) or 0.1 M phosphate buffer (black). Reprinted with permission from ref 288. Copyright 2013 American Chemical Society.

7.2 for  $\text{H}_2\text{PO}_4^-/\text{HPO}_4^{2-}$  and 9.2 for borate, this appears to be an additional consequence of the use of APT pathways in the water oxidation step and the low concentration of the borate buffer base at this pH.

Photoelectrochemical measurements on assembly 27 were extended to the assemblies in 28 with  $n = 1$  or 3 in order to explore the possible appearance of a surface bimolecular O---O coupling pathway. Kinetic studies in solution with Ce(IV) as oxidant have provided evidence for such a pathway following oxidation and coordination expansion to a reactive seven-coordinate Ru(V) intermediate.<sup>222,289</sup> In these experiments, enhanced photocurrents were observed for the surface-bound catalyst with the longer  $-\text{CH}_2-$  ( $n = 3$ ) link to the surface.

A series of PEC measurements were carried out on covalently linked molecular assembly 18 with visible (445 nm) excitation.<sup>126</sup> The key to successful DSPEC performance was the use of a “core/shell” oxide structure at the photoanode. The oxide core/shells were designed to overcome the kinetic limitations with  $\text{TiO}_2$  described in Section 3.9, arising from BET in competition with electron migration through the oxide

film to the cathode. The core/shell structures consisted of nanoparticle tin-doped indium oxide ( $\text{Sn(IV)}:\text{In}_2\text{O}_3$ , nanoITO) or antimony-doped tin oxide ( $\text{Sb(V)}:\text{SnO}_2$ , nanoATO) cores on transparent FTO. They were coated with 3.6 nm shells of  $\text{TiO}_2$  deposited by ALD.<sup>126</sup> A TEM image of a core/shell structure is shown in Figure 19. Following ALD deposition of the  $\text{TiO}_2$  shell, the core/shell oxides were derivatized with assembly 18 to give the photoanodes,  $\text{FTO}|\text{nanoITO}|[\text{TiO}_2] - [\text{Ru}^{II}-\text{Ru}^{II}-\text{OH}_2]^{4+}$ . Sustained water splitting was observed upon photolysis of a pH 4.6 acetate-buffered solution with an APCE of 4.4%. After 30 min of irradiation, the photocurrent decreased from 185  $\mu\text{A}/\text{cm}^2$  to 20  $\mu\text{A}/\text{cm}^2$ , due to a combination of desorption from the core/shell surface and decomposition of the chromophore.<sup>406</sup>

The core/shell was important in increasing cell efficiency by a factor of >10. As revealed by the results of TA experiments on a core/shell DSSC, the importance of the core/shell was in controlling interfacial dynamics.<sup>126</sup>

Following excitation and injection by the chromophore, transfer of the injected electrons through the conducting transparent oxide is greatly facilitated. BET to the surface-bound assembly occurred by electron tunneling and was inhibited as the thickness of the shell was increased. Cell efficiencies were maximized at a thickness of 3.6 nm. As the shell thickness was increased further, trap states appeared in the shell, inhibiting electron transport to the core.

In a follow-up experiment, assembly 18 was further investigated in a DSPEC on  $\text{SnO}_2/\text{TiO}_2$  core/shell electrodes (Figure 19).<sup>286</sup> In this structure, the ~0.4 V more positive conduction-band potential for  $\text{SnO}_2$  compared to  $\text{TiO}_2$  was exploited to create an uphill barrier to BET through the shell to the oxidized assembly. Photocurrent density enhancements of >30 were observed for core/shell structures compared to  $\text{SnO}_2$  and were maximized at a shell thickness of 4.5 nm. In order to avoid loss of the assembly by surface hydrolysis, the surface-bound assembly was stabilized by ALD overlayers of  $\text{TiO}_2$  or  $\text{Al}_2\text{O}_3$ . A structure of the surface-stabilized, derivatized core/shell assembly electrode,  $\text{FTO}|\text{nanoITO}|[\text{TiO}_2]$  (4.5 nm)l- $[\text{Ru}^{II}-\text{Ru}^{II}-\text{OH}_2]^{4+}$  ( $\text{Al}_2\text{O}_3$ , 0.3 nm), is shown in Figure

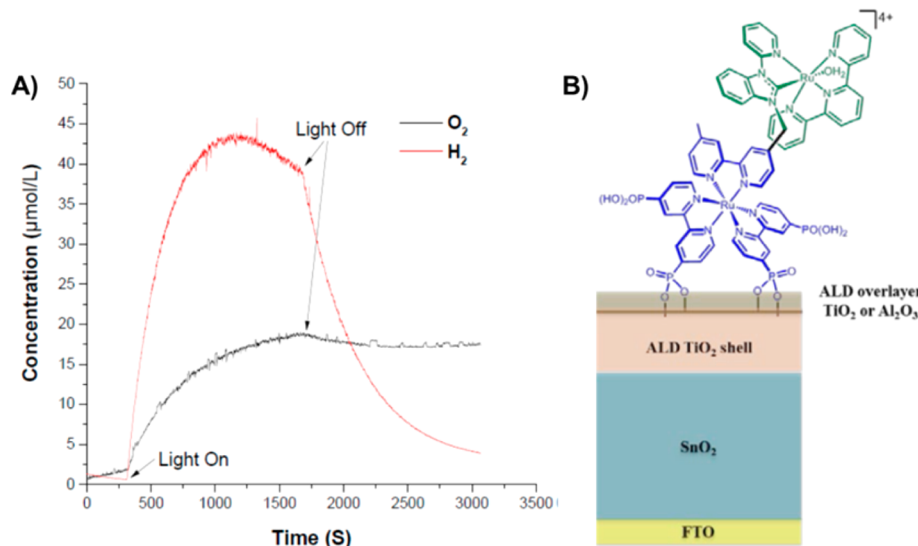


**Figure 43.** (A) Direct monitoring of  $\text{O}_2$  (photoanode) and  $\text{H}_2$  (cathode) by microelectrode sensing with a 600 mV applied bias in a 0.1 M  $\text{H}_2\text{PO}_4^-/\text{HPO}_4^{2-}$  buffer at pH 7 at room temperature of assembly 18, with the ionic strength adjusted to 0.5 M with  $\text{NaClO}_4$ . Illumination by a 455 nm light-emitting diode at 46.2 mW/cm<sup>2</sup>. (B) Structure of surface-stabilized, derivatized core/shell assembly 18.

43B. For the resulting stabilized assembly, maximum photocurrents of  $1.97 \text{ mA/cm}^2$  were obtained with a 4.5 nm  $\text{TiO}_2$  shell and 0.55 nm overlayer of  $\text{Al}_2\text{O}_3$ , with an APCE of  $\sim 20\%$  with 445 nm excitation. Direct monitoring of evolved  $\text{O}_2$  at the photoanode and  $\text{H}_2$  from the cathode by *in situ* microelectrode analysis is shown in Figure 43A.

The use of ALD and core/shell structures has been extended to a layer-by-layer assembly strategy, pioneered by Mallouk and co-workers,<sup>90,335,336</sup> based on prior surface binding of the phosphonic acid derivative  $[\text{Ru}(4,4'\text{-PO}_3\text{H}_2\text{bpy})_2(\text{bpy})]^{2+}$  ( $\text{RuP}_2^{2+}$ ; Figure 34), followed by a surface overlayer of  $\sim 2$  nm nanoparticles of the WOC  $\text{IrO}_x$ , Figure 44.<sup>423</sup> Significantly

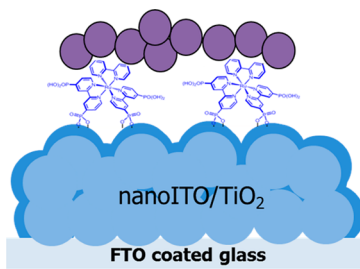


**Figure 44.** Illustration of the dip-coated, layer-by-layer assembly of surface-bound  $[\text{Ru}(4,4'\text{-PO}_3\text{H}_2\text{bpy})_2(\text{bpy})]^{2+}$  ( $\text{RuP}_2^{2+}$ ) and  $\text{IrO}_x$  nanoparticles on a nanoITO/TiO<sub>2</sub> core/shell to give FTO|nanoITO| $\text{TiO}_2|-\text{RuP}_2^{2+},\text{IrO}_x$ .<sup>423</sup>

enhanced, bias-dependent photocurrents for water splitting were observed upon Lumencor 455 nm 14.5 mW/cm<sup>2</sup> irradiation at pH 5.8 in a NaSiF<sub>6</sub> buffer with a Pt cathode. Photocurrents from the resulting photoanodes, FTO|nanoITO| $\text{TiO}_2|-\text{RuP}_2^{2+},\text{IrO}_x$ , were dependent on TiO<sub>2</sub> shell thickness and applied bias, reaching  $0.2 \text{ mA/cm}^2$  at  $0.5 \text{ V}$  vs AgCl/Ag with a shell thickness of 6.6 nm. Long-term photolysis resulted in a decrease in photocurrent due to surface hydrolysis and loss of the chromophore from the surface. Enhanced stability and sustained photocurrents were obtained by stabilization of the surface-bound chromophore by ALD overlayers of TiO<sub>2</sub>.

## 9. EVALUATING DSPEC PERFORMANCE

Standardized measures for quantifying DSPEC performance is becoming an increasingly important issue as the area evolves. Comparisons between and among systems is often difficult to assess due to differences in applied bias, supporting electrolyte, pH, driving force, surface loading, light intensity, experiment duration, etc. An additional complication arises from the use of different measures of efficiency ( $\eta$ ), including solar-to-hydrogen (STH), solar-to-oxygen (STO), applied bias photon-to-current efficiency (ABPE), incident photon-to-current efficiency (IPCE), and absorbed photon-to-current efficiency (APCE).<sup>73</sup> All five are discussed here briefly as ways to characterize PEC performance, noting ref 73 for a more detailed discussion on techniques and data interpretation.

Intrinsic cell efficiencies are derived from H<sub>2</sub> and O<sub>2</sub> product yield measurements giving values for STH and STO. They describe the efficiency of the device under broadband solar irradiance (AM 1.5G) without external bias. STH efficiencies are calculated by using eq 37, in which  $j_{\text{SC}}$  is the short-circuit

$$\text{STH} = \frac{j_{\text{SC}} 1.23V\eta_{\text{H}}}{P_{\text{total}}} \quad (37)$$

photocurrent density (in mA/cm<sup>2</sup>),  $P_{\text{total}}$  is the incident illumination power density (in mW/cm<sup>2</sup>),  $\eta_{\text{H}}$  is the Faradaic efficiency for hydrogen evolution, and 1.23 V is the thermodynamic potential for water splitting at 25 °C under standard conditions.<sup>73</sup> STO O<sub>2</sub> efficiencies are calculated in a similar manner by using eq 38, with  $\eta_{\text{O}}$  the Faradaic efficiency

$$\text{STO} = \frac{j_{\text{SC}} 1.23V\eta_{\text{O}}}{P_{\text{total}}} \quad (38)$$

for oxygen evolution. In a completely efficient water splitting cell, all Faradaic current is converted into H<sub>2</sub> and O<sub>2</sub>, and STH and STO are equal. Both are important quantities in a working PEC device because of possible contributions to the observed Faradaic current from impurities in the solution, decomposition of chromophore and/or catalyst, or a combination of the two. In thick films with all light absorbed and an AM 1.5G light source, measured STH and STO values give the limiting solar efficiencies for water splitting.

The applied bias forms of the H<sub>2</sub> and O<sub>2</sub> yields, ABPE, are analogous to STH and STO, obtained with broadband solar irradiance (AM 1.5G), but with applied bias to maximize photocurrent response. As noted in Section 3.1, an applied bias is required to maximize water splitting with TiO<sub>2</sub> or SnO<sub>2</sub> as the semiconductor oxides in order to drive H<sub>2</sub>O/H<sup>+</sup> reduction to completion. With the highly efficient SnO<sub>2</sub>/TiO<sub>2</sub> core/shell configuration in Figure 19, the applied potential for maximized current efficiency is  $\sim 0.4 \text{ V}$  higher than for TiO<sub>2</sub> because of the more positive conduction-band edge potential for SnO<sub>2</sub>.

With an applied bias, ABPE<sub>H<sub>2</sub></sub> or ABPE<sub>O<sub>2</sub></sub> is calculated from eq 39. In this equation,  $j_{\text{ph}}$  is the photocurrent density,  $V_b$  (vs

$$\text{ABPE}_x = \frac{j_{\text{ph}} (1.23V - V_b)\eta_x}{P_{\text{total}}} \quad (39)$$

NHE) is the applied bias, and  $\eta_x$  is the Faradaic efficiency for oxygen ( $\eta_{\text{O}}$ ) or hydrogen production ( $\eta_{\text{H}}$ ).<sup>73</sup> Measurements of ABPE are made in three-electrode cells with the working electrode held at a known potential against an external reference. The quantity  $V_b$  is the *measured* potential difference between the working electrode and the counter electrode in the operating photoelectrolysis cell.

The incident photon-to-current efficiency is a photochemical quantity providing insight into the microscopic efficiency of the cell. In an IPCE experiment, carried out under conditions of limited irradiance with monochromatic light, the current generated per photon absorbed is measured. In a typical experiment, photocurrents are measured with scanning through the absorption spectrum to identify the absorption features leading to injection. IPCE measurements can be conducted with or without an external bias with correction made for the steady state background current, if non-negligible. The IPCE at wavelength  $\lambda$  is calculated by using eq 40, where  $h$  is Planck's

$$\text{IPCE}(\lambda) = \frac{j_{\text{ph}} hc}{P_{\text{mono}}\lambda} \quad (40)$$

constant,  $c$  is the speed of light, and  $P_{\text{mono}}$  is the monochromated illumination power intensity.<sup>73</sup> IPCE measurements alone do not provide insight into the production of O<sub>2</sub>

and H<sub>2</sub> and those measurements must be conducted separately. Under conditions of broadband solar irradiance (AM 1.5G) with no external bias, the integrated area under a IPCE(λ)–λ trace gives maximum possible values for STH and STO.

The APCE, unlike STH, STO, ABPE, or IPCE, takes into account photons reflected or transmitted through the film and measures efficiencies as a function of actual photons absorbed. As for the IPCE experiment, it is a monochromatic measurement, giving the electrons generated per photon absorbed at a given wavelength or, with scanning, the quantitative photocurrent spectral response. It is also corrected for background photocurrents. APCE is calculated by using eq 41, in which A(λ) is the absorbance at wavelength λ. As with IPCE measurements, the Faradaic efficiencies for H<sub>2</sub> and O<sub>2</sub> are evaluated separately.

$$\text{APCE}(\lambda) = \frac{j_{\text{ph}} hc}{P_{\text{mono}} \lambda (1 - 10^{-A})} \quad (41)$$

## 10. POSTSCRIPT

The integration of chromophore–catalyst assemblies with semiconductor oxides has opened a new approach to solar energy conversion and storage based on the dye-sensitized photoelectrosynthesis cell (DSPEC). Its origins lie in the results of fundamental studies on molecular light absorption and excited-state reactivity, molecular catalysis of water oxidation, and significant advances in the design and synthesis of molecular assemblies. It integrates molecular-level light absorption and electron-transfer activation of catalysis, reactions that lie at the heart of natural photosynthesis, with the intrinsic properties of semiconductor oxides. It exploits molecules and chemical synthesis to modify light absorption and catalytic properties as a systematic way to address target solar fuel reactions.

An impressive number of chromophore–catalyst assembly strategies have been explored and documented in the literature. More will follow. High efficiencies for excited-state injection and intra-assembly electron-transfer activation have been demonstrated by transient absorption measurements. Water oxidation catalysts and conditions for maximizing rates of water oxidation have been identified with results approaching the rates and stabilities needed for application in DSPEC devices. Procedures have been developed for stabilizing surface binding of assemblies to oxide surfaces by atomic layer deposition, polymer film overlayers, and electro-assembly formation. Manipulation of oxide structure by use of atomic layer deposition has been used to prepare TiO<sub>2</sub>-based core/shells that have resulted in greatly enhanced efficiencies for DSPEC water splitting.

Many challenges remain:

- continued manipulation of molecular and interfacial structures in order to maximize the microscopic efficiency of light-driven water splitting;
- extension of the excitation wavelength range further into the visible region to achieve higher solar efficiencies;
- stabilizing surface binding and the chemical stability of assemblies for long-term performance in device configurations;
- incorporating organic dye molecules as chromophores and first row transition metal catalysts for water oxidation;

- extending the DSPEC design to bias-free, tandem configurations for water splitting and CO<sub>2</sub> reduction;
- developing photocathodes for CO<sub>2</sub> reduction including core–shell cathodes based on NiO;
- developing tandem cells for CO<sub>2</sub> reduction to syngas (CO:H<sub>2</sub>) for use in Fischer–Tropsch synthesis of hydrocarbons or to formate/formic acid for use in fuel cells;
- scaling-up and engineering practical devices based on zero-gap configurations, gas separation and storage designs, and integration in large scale devices;
- achieving indefinite stability of components and devices in device configurations or introducing designs for the facile replacement of components.

Much has been accomplished, but much remains to be done.

## AUTHOR INFORMATION

### Corresponding Author

\*E-mail: [tjmeyer@unc.edu](mailto:tjmeyer@unc.edu).

### Notes

The authors declare no competing financial interest.

### Biographies



Dennis L. Ashford received his Bachelor of Science degree in Chemistry from Northern Kentucky University in 2010. He worked under the supervision of Professors Joseph L. Templeton and Thomas J. Meyer at UNC–Chapel Hill on the design and synthesis of molecular chromophore–catalyst assemblies for photoelectrochemical water splitting and was awarded his Ph.D. in 2014. He is now an Advanced Research Chemist at Eastman Chemical Company in Kingsport, Tennessee.



Melissa K. Gish received her B.S. in Chemistry from the University of Southern California in 2011. During her time in Los Angeles, her

research under Professor Andrey F. Vilesov was focused on nuclear spin conversion of isolated water molecules using low-temperature FTIR. She is currently pursuing her Ph.D. in physical chemistry at UNC–Chapel Hill in Professor John M. Papanikolas' research group. Her current research is focused on studying the electron transfer processes in DSPEC photoanodes using ultrafast and nanosecond spectroscopic techniques.



Aaron K. Vannucci is an assistant professor at The University of South Carolina in the department of chemistry and biochemistry. His group studies the transformations of small molecules through photo- and electrocatalytic processes. He received his Bachelor of Arts degree from the College of Wooster in 2004. At The University of Arizona he worked under Prof. Dennis L. Lichtenberger combining electrochemical, spectroscopic and computational techniques to study hydrogenase inspired catalysts and was awarded his Ph.D. in chemistry in 2009. Aaron then worked as a post-doctoral fellow at UNC–Chapel Hill with Thomas J. Meyer studying electrocatalytic water oxidation and hydrocarbon functionalization mechanisms of electrode-surface-bound Ru-oxo catalysts.



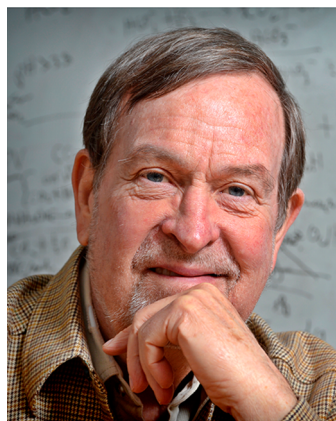
M. Kyle Brenneman received a B.S. from the University of North Alabama in 1998, received his Ph.D. from UNC–Chapel Hill under the direction of Professor John M. Papanikolas in 2004, and completed postdoctoral work at UNC-Chapel Hill under the direction of Professor Thomas J. Meyer from 2005 to 2009. Since then, he has worked in the UNC Center for Solar Fuels, an energy frontier research center funded by the U.S. Department of Energy, as a senior scientist (laser spectroscopist) and facilities director. His research interests include artificial photosynthesis, electron transfer on interfaces and in rigid media, and proton-coupled electron transfer.



Joseph L. Templeton, Venable Professor of Chemistry at UNC–Chapel Hill, received his undergraduate degree at Caltech, his graduate degree at Iowa State, and then spent one year at Imperial College in London before joining the faculty in chemistry at the University of North Carolina at Chapel Hill in 1976.



John Papanikolas received his undergraduate degree in Chemistry from Bowdoin College in 1987, before moving to the University of Colorado at Boulder. There, he earned his PhD in Chemical Physics (1994) and pursued postdoctoral work. In 1997 he moved to the University of North Carolina at Chapel Hill to join the faculty in the Department of Chemistry. Since 2009 he has served as Deputy Director of the UNC Energy Frontier Research Center. His research interests include the use of ultrafast spectroscopies to study molecular systems and materials targeted for solar energy conversion applications.



Thomas J. Meyer first identified proton-coupled electron transfer and designed the first molecular water catalyst. He was an early pioneer in the field of artificial photosynthesis and solar fuels beginning with research published in the 1970s. He has gained an international

reputation in photochemistry, mechanisms, and chemical reactivity and catalysis. He is currently Arey Professor of Chemistry at UNC–Chapel Hill and Director of the UNC Energy Frontier Research Center where the focus is on water oxidation, carbon dioxide reduction, chromophore-catalyst assemblies, and dye sensitized photoelectrosynthesis cells for water splitting and reduction of carbon dioxide.

## ACKNOWLEDGMENTS

This research was supported by the University of North Carolina Energy Frontier Research Center (UNC EFRC), Center for Solar Fuels, an Energy Frontier Research Center supported by the U.S. Department of Energy, Office of Science, Office of Basic Energy Sciences, under Award DE-SC0001011, supporting D.L.A., M.K.G., A.K.V., and M.K.B.

## ABBREVIATIONS

FTO	fluoride-doped tin oxide
ITO	tin-doped indium oxide
nanoITO	nanocrystalline tin-doped indium oxide
TCO	transparent conducting oxide
NHE	normal hydrogen electrode
SCE	saturated calomel electrode
STH	solar-to-hydrogen
STO	solar-to-oxygen
ABPE	applied bias photon-to-current efficiency
APCE	absorbed photon-to-current efficiency
IPCE	incident photon-to-current efficiency
WOC	water oxidation catalyst
DSPEC	dye-sensitized photoelectrochemical cell
DSSC	dye-sensitized solar cell
MLCT	metal-to-ligand charge transfer
BET	back electron transfer
PCET	proton-coupled electron transfer
APT	atom–proton transfer
EPT	electron–proton transfer
EAPT	electron–atom–proton transfer
OEC	oxygen-evolving complex
AM 1.5G	air mass 1.5 global
TA	transient absorption
CV	cyclic voltammetry
SWV	square wave voltammetry
TEM	transmission electron microscopy
UV	ultraviolet
Vis	visible
IR	infrared
ALD	atomic layer deposition
$e^-$	electron
$h^+$	hole
$\alpha$	activity
$\epsilon$	molar extinction coefficient
$\Gamma$	surface coverage
$\nu$	scan rate
$h\nu$	irradiation
$\Phi_{\text{inj}}$	electron injection yield
$\lambda$	wavelength
$\lambda_o$	medium (solvent) reorganization energy
$E_{\text{CB}}$	conduction band energy
$E_{1/2}$	half-wave potential
$\Delta E_{1/2}$	electrochemical gap
$E_0$	0–0 energy gap
$E^\circ$	standard potential

$E^\circ'$	formal potential
$\tau$	lifetime
$t_{1/2}$	half-life
$Q$	charge
$\Delta Q_{\text{eq}}$	equilibrium displacement change
$\Delta \bar{\nu}_{1/2}$	bandwidth at half-height
$\Delta G_{\text{ES}}$	free energy of the excited state
$F$	Faraday's constant
$k_B$	Boltzmann constant

## REFERENCES

- (1) *Annual Energy Outlook*; U.S. Department of Energy, Washington, DC, 2013.
- (2) Lewis, N. S.; Nocera, D. G. Powering the planet: chemical challenges in solar energy utilization. *Proc. Natl. Acad. Sci. U. S. A.* **2006**, *103*, 15729–15735.
- (3) Shafiee, S.; Topal, E. When will fossil fuel reserves be diminished? *Energy Policy* **2009**, *37*, 181–189.
- (4) Dresselhaus, M. S.; Thomas, I. L. Alternative energy technologies. *Nature* **2001**, *414*, 332–337.
- (5) Murray, J.; King, D. Climate policy: Oil's tipping point has passed. *Nature* **2012**, *481*, 433–435.
- (6) Sigman, D. M.; Hain, M. P.; Haug, G. H. The polar ocean and glacial cycles in atmospheric CO<sub>2</sub> concentration. *Nature* **2010**, *466*, 47–55.
- (7) Breecker, D. O.; Sharp, Z. D.; McFadden, L. D. Atmospheric CO<sub>2</sub> concentrations during ancient greenhouse climates were similar to those predicted for A.D. 2100. *Proc. Natl. Acad. Sci. U. S. A.* **2010**, *107*, 576–580.
- (8) Petit, J. R.; Jouzel, J.; Raynaud, D.; Barkov, N. I.; Barnola, J. M.; Basile, I.; Bender, M.; Chappellaz, J.; Davis, M.; Delaygue, G.; et al. Climate and atmospheric history of the past 420,000 years from the Vostok ice core, Antarctica. *Nature* **1999**, *399*, 429–436.
- (9) Siegenthaler, U.; Stocker, T. F.; Monnin, E.; Luethi, D.; Schwander, J.; Stauffer, B.; Raynaud, D.; Barnola, J.-M.; Fischer, H.; Masson-Delmotte, V.; et al. Stable carbon cycle-climate relationship during the Late Pleistocene. *Science* **2005**, *310*, 1313–1317.
- (10) Wigley, T. M. L.; Richels, R.; Edmonds, J. A. Economic and environmental choices in the stabilization of atmospheric CO<sub>2</sub> concentrations. *Nature* **1996**, *379*, 240–243.
- (11) Bak, T.; Nowotny, J.; Rekas, M.; Sorrell, C. C. Photoelectrochemical hydrogen generation from water using solar energy. Materials-related aspects. *Int. J. Hydrogen Energy* **2002**, *27*, 991–1022.
- (12) Valentine, K. *ThinkProgress* **2013**.
- (13) Christensen, J.; Albertus, P.; Sanchez-Carrera, R. S.; Lohmann, T.; Kozinsky, B.; Liedtke, R.; Ahmed, J.; Kojic, A. A Critical Review of Li/Air Batteries. *J. Electrochem. Soc.* **2012**, *159*, R1–R30.
- (14) Bruce, P. G.; Freunberger, S. A.; Hardwick, L. J.; Tarascon, J.-M. Li-O<sub>2</sub> and Li-S batteries with high energy storage. *Nat. Mater.* **2012**, *11*, 19–29.
- (15) Gao, M.-R.; Xu, Y.-F.; Jiang, J.; Yu, S.-H. Nanostructured metal chalcogenides: synthesis, modification, and applications in energy conversion and storage devices. *Chem. Soc. Rev.* **2013**, *42*, 2986–3017.
- (16) Lu, Y.-C.; Gallant, B. M.; Kwabi, D. G.; Harding, J. R.; Mitchell, R. R.; Whittingham, M. S.; Shao-Horn, Y. Lithium-oxygen batteries: bridging mechanistic understanding and battery performance. *Energy Environ. Sci.* **2013**, *6*, 750–768.
- (17) Shao, Y.; Park, S.; Xiao, J.; Zhang, J.-G.; Wang, Y.; Liu, J. Electrocatalysts for Nonaqueous Lithium-Air Batteries: Status, Challenges, and Perspective. *ACS Catal.* **2012**, *2*, 844–857.
- (18) Wang, W.; Luo, Q.; Li, B.; Wei, X.; Li, L.; Yang, Z. Recent Progress in Redox Flow Battery Research and Development. *Adv. Funct. Mater.* **2013**, *23*, 970–986.
- (19) Seh, Z. W.; Li, W.; Cha, J. J.; Zheng, G.; Yang, Y.; McDowell, M. T.; Hsu, P.-C.; Cui, Y. Sulphur-TiO<sub>2</sub> yolk-shell nanoarchitecture with internal void space for long-cycle lithium-sulphur batteries. *Nat. Commun.* **2013**, *4*, 1331.

- (20) Renger, G. Oxidative photosynthetic water splitting: Energetics, kinetics and mechanism. *Photosynth. Res.* **2007**, *92*, 407–425.
- (21) Ferreira, K. N.; Iverson, T. M.; Maghlaoui, K.; Barber, J.; Iwata, S. Architecture of the Photosynthetic Oxygen-Evolving Center. *Science* **2004**, *303*, 1831–1838.
- (22) Barber, J. Engine of life and big bang of evolution: a personal perspective. *Photosynth. Res.* **2004**, *80*, 137–155.
- (23) Umena, Y.; Kawakami, K.; Shen, J.-R.; Kamiya, N. Crystal structure of oxygen-evolving photosystem II at a resolution of 1.9 Å. *Nature* **2011**, *473*, 55–60.
- (24) Song, W.; Chen, Z.; Glasson, C. R.; Hanson, K.; Luo, H.; Norris, M. R.; Ashford, D. L.; Concepcion, J. J.; Brennaman, M. K.; Meyer, T. J. Interfacial Dynamics and Solar Fuel Formation in Dye-Sensitized Photoelectrosynthesis Cells. *ChemPhysChem* **2012**, *13*, 2882–2890.
- (25) Zhu, X.-G.; Long, S. P.; Ort, D. R. Improving photosynthetic efficiency for greater yield. *Annu. Rev. Plant Biol.* **2010**, *61*, 235–261.
- (26) Wijffels, R. H.; Barbosa, M. J. An Outlook on Microalgal Biofuels. *Science* **2010**, *329*, 796–799.
- (27) Blankenship, R. E.; Tiede, D. M.; Barber, J.; Brudvig, G. W.; Fleming, G.; Ghirardi, M.; Gunner, M. R.; Junge, W.; Kramer, D. M.; Melis, A.; et al. Comparing Photosynthetic and Photovoltaic Efficiencies and Recognizing the Potential for Improvement. *Science* **2011**, *332*, 805–809.
- (28) Reece, S. Y.; Hamel, J. A.; Sung, K.; Jarvi, T. D.; Esswein, A. J.; Pijpers, J. J. H.; Nocera, D. G. Wireless Solar Water Splitting Using Silicon-Based Semiconductors and Earth-Abundant Catalysts. *Science* **2011**, *334*, 645–648.
- (29) Gust, D.; Moore, T. A.; Moore, A. L. Solar Fuels via Artificial Photosynthesis. *Acc. Chem. Res.* **2009**, *42*, 1890–1898.
- (30) Gilbert, J. A.; Eggleston, D. S.; Murphy, W. R., Jr.; Geselowitz, D. A.; Gersten, S. W.; Hodgson, D. J.; Meyer, T. J. Structure and redox properties of the water-oxidation catalyst [(bpy)2(OH2)RuORu(OH2)(bpy)2]4+. *J. Am. Chem. Soc.* **1985**, *107*, 3855–3864.
- (31) Yagi, M.; Kaneko, M. Molecular Catalysts for Water Oxidation. *Chem. Rev.* **2001**, *101*, 21–35.
- (32) Meyer, T. J.; Huynh, M. H. V.; Thorp, H. H. The possible role of proton-coupled electron transfer (PCET) in water oxidation by photosystem II. *Angew. Chem., Int. Ed.* **2007**, *46*, 5284–5304.
- (33) Concepcion, J. J.; Jurss, J. W.; Norris, M. R.; Chen, Z. F.; Templeton, J. L.; Meyer, T. J. Catalytic Water Oxidation by Single-Site Ruthenium Catalysts. *Inorg. Chem.* **2010**, *49*, 1277–1279.
- (34) Concepcion, J. J.; Jurss, J. W.; Templeton, J. L.; Meyer, T. J. One Site is Enough. Catalytic Water Oxidation by [Ru(tpy)(bpym)(OH2)]2+ and [Ru(tpy)(bpz)(OH2)]2+. *J. Am. Chem. Soc.* **2008**, *130*, 16462–16463.
- (35) Concepcion, J. J.; Tsai, M. K.; Muckerman, J. T.; Meyer, T. J. Mechanism of Water Oxidation by Single-Site Ruthenium Complex Catalysts. *J. Am. Chem. Soc.* **2010**, *132*, 1545–1557.
- (36) Hurst, J. K.; Cape, J. L.; Clark, A. E.; Das, S.; Qin, C. Mechanisms of Water Oxidation Catalyzed by Ruthenium Diimine Complexes. *Inorg. Chem.* **2008**, *47*, 1753–1764.
- (37) Brimblecombe, R.; Dismukes, G. C.; Swiegers, G. F.; Spiccia, L. Molecular water-oxidation catalysts for photoelectrochemical cells. *Dalton Trans.* **2009**, 9374–9384.
- (38) Weinberg, D. R.; Gagliardi, C. J.; Hull, J. F.; Murphy, C. F.; Kent, C. A.; Westlake, B. C.; Paul, A.; Ess, D. H.; McCafferty, D. G.; Meyer, T. J. Proton-Coupled Electron Transfer. *Chem. Rev.* **2012**, *112*, 4016–4093.
- (39) Huynh, M. H. V.; Meyer, T. J. Proton-Coupled Electron Transfer. *Chem. Rev.* **2007**, *107*, 5004–5064.
- (40) Cukier, R. I.; Nocera, D. G. Proton-coupled electron transfer. *Annu. Rev. Phys. Chem.* **1998**, *49*, 337–369.
- (41) Mayer, J. M. Proton-coupled electron transfer: A reaction chemist's view. *Annu. Rev. Phys. Chem.* **2004**, *55*, 363–390.
- (42) Concepcion, J. J.; Jurss, J. W.; Brennaman, M. K.; Hoertz, P. G.; Patrocino, A. O. T.; Murakami Iha, N. Y.; Templeton, J. L.; Meyer, T. J. Making Oxygen with Ruthenium Complexes. *Acc. Chem. Res.* **2009**, *42*, 1954–1965.
- (43) Nocera, D. G. The Artificial Leaf. *Acc. Chem. Res.* **2012**, *45*, 767–776.
- (44) Kanan, M. W.; Nocera, D. G. In Situ Formation of an Oxygen-Evolving Catalyst in Neutral Water Containing Phosphate and Co2+. *Science* **2008**, *321*, 1072–1075.
- (45) Fujishima, A.; Honda, K. Electrochemical photolysis of water at a semiconductor electrode. *Nature* **1972**, *238*, 37–38.
- (46) Chen, X.; Shen, S.; Guo, L.; Mao, S. S. Semiconductor-based Photocatalytic Hydrogen Generation. *Chem. Rev.* **2010**, *110*, 6503–6570.
- (47) Kudo, A.; Kato, H.; Tsuji, I. Strategies for the development of visible-light-driven photocatalysts for water splitting. *Chem. Lett.* **2004**, *33*, 1534–1539.
- (48) Young, K. M. H.; Klahr, B. M.; Zandi, O.; Hamann, T. W. Photocatalytic water oxidation with hematite electrodes. *Catal. Sci. Technol.* **2013**, *3*, 1660–1671.
- (49) Butler, M. A. Photoelectrolysis and physical properties of the semiconducting electrode tungsten trioxide. *J. Appl. Phys.* **1977**, *48*, 1914–1920.
- (50) Hong, S. J.; Lee, S.; Jang, J. S.; Lee, J. S. Heterojunction BiVO4/WO3 electrodes for enhanced photoactivity of water oxidation. *Energy Environ. Sci.* **2011**, *4*, 1781–1787.
- (51) Katz, M. J.; Riha, S. C.; Jeong, N. C.; Martinson, A. B. F.; Farha, O. K.; Hupp, J. T. Toward solar fuels: Water splitting with sunlight and "rust"? *Coord. Chem. Rev.* **2012**, *256*, 2521–2529.
- (52) Kay, A.; Cesar, I.; Graetzel, M. New Benchmark for Water Photooxidation by Nanostructured  $\alpha$ -Fe2O3 Films. *J. Am. Chem. Soc.* **2006**, *128*, 15714–15721.
- (53) Ling, Y.; Wang, G.; Wheeler, D. A.; Zhang, J. Z.; Li, Y. Sn-Doped Hematite Nanostructures for Photoelectrochemical Water Splitting. *Nano Lett.* **2011**, *11*, 2119–2125.
- (54) Albero, J.; Clifford, J. N.; Palomares, E. Quantum dot based molecular solar cells. *Coord. Chem. Rev.* **2014**, *53*, 263–264.
- (55) Kochuveedu, S. T.; Jang, Y. H.; Kim, D. H. A study on the mechanism for the interaction of light with noble metal-metal oxide semiconductor nanostructures for various photophysical applications. *Chem. Soc. Rev.* **2013**, *42*, 8467–8493.
- (56) Alexander, B. D.; Kulesza, P. J.; Rutkowska, I.; Solarska, R.; Augustynski, J. Metal oxide photoanodes for solar hydrogen production. *J. Mater. Chem.* **2008**, *18*, 2298–2303.
- (57) Guo, L.; Hung, D.; Wang, W.; Shen, W.; Zhu, L.; Chien, C.-L.; Seearson, P. C. Tunnel barrier photoelectrodes for solar water splitting. *Appl. Phys. Lett.* **2010**, *97*, 063111–063113.
- (58) Zhang, Z.; Dua, R.; Zhang, L.; Zhu, H.; Zhang, H.; Wang, P. Carbon-Layer-Protected Cuprous Oxide Nanowire Arrays for Efficient Water Reduction. *ACS Nano* **2013**, *7*, 1709–1717.
- (59) Duonghong, D.; Borgarello, E.; Graetzel, M. Dynamics of light-induced water cleavage in colloidal systems. *J. Am. Chem. Soc.* **1981**, *103*, 4685–4690.
- (60) Osterloh, F. E. Inorganic nanostructures for photoelectrochemical and photocatalytic water splitting. *Chem. Soc. Rev.* **2013**, *42*, 2294–2320.
- (61) Kudo, A.; Miseki, Y. Heterogeneous photocatalyst materials for water splitting. *Chem. Soc. Rev.* **2009**, *38*, 253–278.
- (62) Osterloh, F. E. Inorganic Materials as Catalysts for Photochemical Splitting of Water. *Chem. Mater.* **2008**, *20*, 35–54.
- (63) Osterloh, F. E.; Parkinson, B. A. Recent developments in solar water-splitting photocatalysis. *MRS Bull.* **2011**, *36*, 17–22.
- (64) Maeda, K. Z-Scheme Water Splitting Using Two Different Semiconductor Photocatalysts. *ACS Catal.* **2013**, *3*, 1486–1503.
- (65) Yang, J.; Wang, D.; Han, H.; Li, C. Roles of cocatalysts in photocatalysis and photoelectrocatalysis. *Acc. Chem. Res.* **2013**, *46*, 1900–1909.
- (66) Maeda, K.; Lu, D.; Domen, K. Direct Water Splitting into Hydrogen and Oxygen under Visible Light by using Modified TaON Photocatalysts with d0 Electronic Configuration. *Chem. - Eur. J.* **2013**, *19*, 4986–4991.
- (67) Kelzenberg, M. D.; Boettcher, S. W.; Petykiewicz, J. A.; Turner-Evans, D. B.; Putnam, M. C.; Warren, E. L.; Spurgeon, J. M.; Briggs, R.

- M.; Lewis, N. S.; Atwater, H. A. Enhanced absorption and carrier collection in Si wire arrays for photovoltaic applications. *Nat. Mater.* **2010**, *9*, 239–244.
- (68) Walter, M. G.; Warren, E. L.; McKone, J. R.; Boettcher, S. W.; Mi, Q.; Santori, E. A.; Lewis, N. S. Solar Water Splitting Cells. *Chem. Rev.* **2010**, *110*, 6446–6473.
- (69) Spurgeon, J. M.; Boettcher, S. W.; Kelzenberg, M. D.; Brunschwig, B. S.; Atwater, H. A.; Lewis, N. S. Flexible, polymer-supported, Si wire array photoelectrodes. *Adv. Mater.* **2010**, *22*, 3277–3281.
- (70) Spurgeon, J. M.; Walter, M. G.; Zhou, J.; Kohl, P. A.; Lewis, N. S. Electrical conductivity, ionic conductivity, optical absorption, and gas separation properties of ionically conductive polymer membranes embedded with Si microwire arrays. *Energy Environ. Sci.* **2011**, *4*, 1772–1780.
- (71) Lewis, N. S. Toward Cost-Effective Solar Energy Use. *Science* **2007**, *315*, 798–801.
- (72) Hou, Y.; Abrams, B. L.; Vesborg, P. C. K.; Bjoerketun, M. E.; Herbst, K.; Bech, L.; Setti, A. M.; Damsgaard, C. D.; Pedersen, T.; Hansen, O.; et al. Bioinspired molecular co-catalysts bonded to a silicon photocathode for solar hydrogen evolution. *Nat. Mater.* **2011**, *10*, 434–438.
- (73) Chen, Z.; Dinh, H. N.; Miller, E. *Photoelectrochemical Water Splitting: Standards, Experimental Methods, and Protocols*; Springer: New York, NY, 2013.
- (74) Rocheleau, R. E.; Miller, E. L.; Misra, A. High-efficiency photoelectrochemical hydrogen production using multijunction amorphous silicon photoelectrodes. *Energy Fuels* **1998**, *12*, 3–10.
- (75) Surendranath, Y.; Dinca, M.; Nocera, D. G. Electrolyte-Dependent Electrosynthesis and Activity of Cobalt-Based Water Oxidation Catalysts. *J. Am. Chem. Soc.* **2009**, *131*, 2615–2620.
- (76) Lutterman, D. A.; Surendranath, Y.; Nocera, D. G. A Self-Healing Oxygen-Evolving Catalyst. *J. Am. Chem. Soc.* **2009**, *131*, 3838–3839.
- (77) Khaselev, O.; Turner, J. A. A monolithic photovoltaic-photoelectrochemical device for hydrogen production via water splitting. *Science* **1998**, *280*, 425–427.
- (78) Joya, K. S.; Joya, Y. F.; Ocakoglu, K.; van de Krol, R. Water-splitting catalysis and solar fuel devices: artificial leaves on the move. *Angew. Chem., Int. Ed.* **2013**, *52*, 10426–10437.
- (79) Bard, A. J. Photoelectrochemistry and heterogeneous photocatalysis at semiconductors. *J. Photochem.* **1979**, *10*, 59–75.
- (80) Maeda, K.; Higashi, M.; Lu, D.; Abe, R.; Domen, K. Efficient Nonsacrificial Water Splitting through Two-Step Photoexcitation by Visible Light using a Modified Oxynitride as a Hydrogen Evolution Photocatalyst. *J. Am. Chem. Soc.* **2010**, *132*, 5858–5868.
- (81) Tada, H.; Mitsui, T.; Kyonaga, T.; Akita, T.; Tanaka, K. All-solid-state Z-scheme in CdS-Au-TiO<sub>2</sub> three-component nanojunction system. *Nat. Mater.* **2006**, *5*, 782–786.
- (82) Iwase, A.; Ng, Y. H.; Ishiguro, Y.; Kudo, A.; Amal, R. Reduced Graphene Oxide as a Solid-State Electron Mediator in Z-Scheme Photocatalytic Water Splitting under Visible Light. *J. Am. Chem. Soc.* **2011**, *133*, 11054–11057.
- (83) Kudo, A. Z-scheme photocatalyst systems for water splitting under visible light irradiation. *MRS Bull.* **2011**, *36*, 32–38.
- (84) Ingram, D. B.; Linic, S. Water splitting on composite plasmonic-metal/semiconductor photoelectrodes: evidence for selective plasmon-induced formation of charge carriers near the semiconductor surface. *J. Am. Chem. Soc.* **2011**, *133*, 5202–5205.
- (85) Mor, G. K.; Shankar, K.; Paulose, M.; Varghese, O. K.; Grimes, C. A. Enhanced Photocleavage of Water Using Titania Nanotube Arrays. *Nano Lett.* **2005**, *5*, 191–195.
- (86) Zhu, K.; Neale, N. R.; Miedaner, A.; Frank, A. J. Enhanced Charge-Collection Efficiencies and Light Scattering in Dye-Sensitized Solar Cells Using Oriented TiO<sub>2</sub> Nanotubes Arrays. *Nano Lett.* **2007**, *7*, 69–74.
- (87) Klimov, V. I. Mechanisms for Photogeneration and Recombination of Multiexcitons in Semiconductor Nanocrystals: Implications for Lasing and Solar Energy Conversion. *J. Phys. Chem. B* **2006**, *110*, 16827–16845.
- (88) Meyer, B. K.; Alves, H.; Hofmann, D. M.; Kriegseis, W.; Forster, D.; Bertram, F.; Christen, J.; Hoffmann, A.; Strassburg, M.; Dworzak, M.; et al. Bound exciton and donor-acceptor pair recombinations in ZnO. *Phys. Status Solidi B* **2004**, *241*, 231–260.
- (89) Barnhart, C. J.; Dale, M.; Brandt, A. R.; Benson, S. M. The energetic implications of curtailing versus storing solar- and wind-generated electricity. *Energy Environ. Sci.* **2013**, *6*, 2804–2810.
- (90) Youngblood, W. J.; Lee, S.-H. A.; Maeda, K.; Mallouk, T. E. Visible Light Water Splitting using Dye-Sensitized Oxide Semiconductors. *Acc. Chem. Res.* **2009**, *42*, 1966–1973.
- (91) Young, K. J.; Martini, L. A.; Milot, R. L.; Snoeberger, R. C.; Batista, V. S.; Schmuttenmaer, C. A.; Crabtree, R. H.; Brudvig, G. W. Light-driven water oxidation for solar fuels. *Coord. Chem. Rev.* **2012**, *256*, 2503–2520.
- (92) Concepcion, J. J.; House, R. L.; Papanikolas, J. M.; Meyer, T. J. Chemical approaches to artificial photosynthesis. *Proc. Natl. Acad. Sci. U. S. A.* **2012**, *109*, 15560–15564.
- (93) Gratzel, M. Photoelectrochemical cells. *Nature* **2001**, *414*, 338–344.
- (94) Hamann, T. W. Water splitting An adaptive junction. *Nat. Mater.* **2014**, *13*, 3–4.
- (95) Sun, J.; Zhong, D. K.; Gamelin, D. R. Composite photoanodes for photoelectrochemical solar water splitting. *Energy Environ. Sci.* **2010**, *3*, 1252–1261.
- (96) Jiang, C.; Wang, R.; Parkinson, B. A. Combinatorial Approach to Improve Photoelectrodes Based on BiVO<sub>4</sub>. *ACS Comb. Sci.* **2013**, *15*, 639–645.
- (97) Rowley, J. G.; Do, T. D.; Cleary, D. A.; Parkinson, B. A. Combinatorial Discovery Through a Distributed Outreach Program: Investigation of the Photoelectrolysis Activity of p-Type Fe, Cr, Al Oxides. *ACS Appl. Mater. Interfaces* **2014**, *6*, 9046–9052.
- (98) Soley, D.; Ayers, K.; Parkinson, B. A. Combinatorial search for improved metal oxide oxygen evolution electrocatalysts in acidic electrolytes. *ACS Comb. Sci.* **2013**, *15*, 82–89.
- (99) Xiang, C.; Suram, S. K.; Haber, J. A.; Guevarra, D. W.; Soedarmadji, E.; Jin, J.; Gregoire, J. M. High-Throughput Bubble Screening Method for Combinatorial Discovery of Electrocatalysts for Water Splitting. *ACS Comb. Sci.* **2014**, *16*, 47–52.
- (100) Marcus, R. A.; Sutin, N. Electron transfers in chemistry and biology. *Biochim. Biophys. Acta, Rev. Bioenerg.* **1985**, *811*, 265–322.
- (101) Meyer, T. J. Chemical approaches to artificial photosynthesis. *Acc. Chem. Res.* **1989**, *22*, 163–170.
- (102) Wasielewski, M. R. Photoinduced electron transfer in supramolecular systems for artificial photosynthesis. *Chem. Rev.* **1992**, *92*, 435–461.
- (103) Gust, D.; Moore, T. A.; Moore, A. L. Molecular mimicry of photosynthetic energy and electron transfer. *Acc. Chem. Res.* **1993**, *26*, 198–205.
- (104) Kay, A.; Graetzel, M. Artificial photosynthesis. 1. Photosensitization of titania solar cells with chlorophyll derivatives and related natural porphyrins. *J. Phys. Chem.* **1993**, *97*, 6272–6277.
- (105) Bard, A. J.; Fox, M. A. Artificial Photosynthesis: Solar Splitting of Water to Hydrogen and Oxygen. *Acc. Chem. Res.* **1995**, *28*, 141–145.
- (106) Balzani, V.; Credi, A.; Venturi, M. Photochemical conversion of solar energy. *ChemSusChem* **2008**, *1*, 26–58.
- (107) Juris, A.; Balzani, V.; Barigelletti, F.; Campagna, S.; Belser, P.; Von Zelewsky, A. Ruthenium(II) polypyridine complexes: photo-physics, photochemistry, electrochemistry, and chemiluminescence. *Coord. Chem. Rev.* **1988**, *84*, 85–277.
- (108) Ghosh, P. K.; Brunschwig, B. S.; Chou, M.; Creutz, C.; Sutin, N. Thermal and light-induced reduction of the ruthenium complex cation Ru(bpy)<sub>3</sub><sup>2+</sup> in aqueous solution. *J. Am. Chem. Soc.* **1984**, *106*, 4772–4783.
- (109) Hagfeldt, A.; Boschloo, G.; Sun, L.; Kloof, L.; Pettersson, H. Dye-Sensitized Solar Cells. *Chem. Rev.* **2010**, *110*, 6595–6663.

- (110) Gratzel, M. Dye-sensitized solar cells. *J. Photochem. Photobiol.*, C **2003**, *4*, 145–153.
- (111) Gratzel, M. Recent advances in sensitized mesoscopic solar cells. *Acc. Chem. Res.* **2009**, *42*, 1788–1798.
- (112) Graetzel, M. Solar Energy Conversion by Dye-Sensitized Photovoltaic Cells. *Inorg. Chem.* **2005**, *44*, 6841–6851.
- (113) O'Regan, B.; Graetzel, M. A low-cost, high-efficiency solar cell based on dye-sensitized colloidal titanium dioxide films. *Nature* **1991**, *353*, 737–740.
- (114) Swierk, J. R.; Mallouk, T. E. Design and development of photoanodes for water-splitting dye-sensitized photoelectrochemical cells. *Chem. Soc. Rev.* **2013**, *42*, 2357–2387.
- (115) Frischmann, P. D.; Mahata, K.; Wuerthner, F. Powering the future of molecular artificial photosynthesis with light-harvesting metallosupramolecular dye assemblies. *Chem. Soc. Rev.* **2013**, *42*, 1847–1870.
- (116) Ashford, D. L.; Glasson, C. R. K.; Norris, M. R.; Hanson, K.; Concepcion, J. J.; Keinan, S.; Brennaman, M. K.; Templeton, J. L.; Meyer, T. J. Controlling Ground and Excited State Properties through Ligand Changes in Ruthenium Polypyridyl Complexes. *Inorg. Chem.* **2014**, *53*, 5637–5646.
- (117) Thompson, D. W.; Ito, A.; Meyer, T. J.  $[\text{Ru}(\text{bpy})_3]^{2+*}$  and other remarkable metal-to-ligand charge transfer (MLCT) excited states. *Pure Appl. Chem.* **2013**, *85*, 1257–1305.
- (118) Lever, A. B. P. Electrochemical parametrization of metal complex redox potentials, using the ruthenium(III)/ruthenium(II) couple to generate a ligand electrochemical series. *Inorg. Chem.* **1990**, *29*, 1271–1285.
- (119) Yam, V. W.-W.; Lee, V. W.-M.; Ke, F.; Siu, K.-W. M. Synthesis, Photophysics, and Electrochemistry of Ruthenium(II) Polypyridine Complexes with Crown Ether Pendants. *Inorg. Chem.* **1997**, *36*, 2124–2129.
- (120) Mikkelsen, M.; Jorgensen, M.; Krebs, F. C. The teraton challenge. A review of fixation and transformation of carbon dioxide. *Energy Environ. Sci.* **2010**, *3*, 43–81.
- (121) Rakowski Dubois, M.; Dubois, D. L. Development of Molecular Electrocatalysts for CO<sub>2</sub> Reduction and H<sub>2</sub> Production/Oxidation. *Acc. Chem. Res.* **2009**, *42*, 1974–1982.
- (122) Schneider, J.; Jia, H.; Muckerman, J. T.; Fujita, E. Thermodynamics and kinetics of CO<sub>2</sub>, CO, and H<sup>+</sup> binding to the metal center of CO<sub>2</sub> reduction catalysts. *Chem. Soc. Rev.* **2012**, *41*, 2036–2051.
- (123) Takeda, H.; Ishitani, O. Development of efficient photocatalytic systems for CO<sub>2</sub> reduction using mononuclear and multinuclear metal complexes based on mechanistic studies. *Coord. Chem. Rev.* **2010**, *254*, 346–354.
- (124) Odobel, F.; Le Pleux, L.; Pellegrin, Y.; Blart, E. New Photovoltaic Devices Based on the Sensitization of p-type Semiconductors: Challenges and Opportunities. *Acc. Chem. Res.* **2010**, *43*, 1063–1071.
- (125) Odobel, F.; Pellegrin, Y. Recent advances in the sensitization of wide-band-gap nanostructured p-type semiconductors. Photovoltaic and photocatalytic applications. *J. Phys. Chem. Lett.* **2013**, *4*, 2551–2564.
- (126) Alibabaei, L.; Brennaman, K. M.; Norris, M. R.; Kalanyan, B.; Song, W.; Losego, M. D.; Concepcion, J. J.; Binstead, R. A.; Parsons, G. N.; Meyer, T. J. Solar Water Splitting in a Molecular Photoelectrochemical Cell. *Proc. Natl. Acad. Sci. U. S. A.* **2013**, *110*, 20008–20013.
- (127) Morandeira, A.; Fortage, J.; Edvinsson, T.; Le Pleux, L.; Blart, E.; Boschloo, G.; Hagfeldt, A.; Hammarstrom, L.; Odobel, F. Improved Photon-to-Current Conversion Efficiency with a Nanoporous p-Type NiO Electrode by the Use of a Sensitizer-Acceptor Dyad. *J. Phys. Chem. C* **2008**, *112*, 1721–1728.
- (128) He, J.; Lindstroem, H.; Hagfeldt, A.; Lindquist, S.-E. Dye-Sensitized Nanostructured p-Type Nickel Oxide Film as a Photocathode for a Solar Cell. *J. Phys. Chem. B* **1999**, *103*, 8940–8943.
- (129) Gibson, E. A.; Smeigh, A. L.; Le Pleux, L.; Fortage, J.; Boschloo, G.; Blart, E.; Pellegrin, Y.; Odobel, F.; Hagfeldt, A.; Hammarstrom, L. A p-type NiO-based dye-sensitized solar cell with an open-circuit voltage of 0.35 V. *Angew. Chem., Int. Ed.* **2009**, *48*, 4402–4405.
- (130) Gibson, E. A.; Smeigh, A. L.; Le Pleux, L.; Hammarstrom, L.; Odobel, F.; Boschloo, G.; Hagfeldt, A. Cobalt Polypyridyl-Based Electrolytes for p-Type Dye-Sensitized Solar Cells. *J. Phys. Chem. C* **2011**, *115*, 9772–9779.
- (131) Le Pleux, L.; Smeigh, A. L.; Gibson, E.; Pellegrin, Y.; Blart, E.; Boschloo, G.; Hagfeldt, A.; Hammarstrom, L.; Odobel, F. Synthesis, photophysical and photovoltaic investigations of acceptor-functionalized perylene monoimide dyes for nickel oxide p-type dye-sensitized solar cells. *Energy Environ. Sci.* **2011**, *4*, 2075–2084.
- (132) Morandeira, A.; Boschloo, G.; Hagfeldt, A.; Hammarstrom, L. Photoinduced Ultrafast Dynamics of Coumarin 343 Sensitized p-Type-Nanostructured NiO Films. *J. Phys. Chem. B* **2005**, *109*, 19403–19410.
- (133) Li, L.; Duan, L.; Wen, F.; Li, C.; Wang, M.; Hagfeldt, A.; Sun, L. Visible light driven hydrogen production from a photo-active cathode based on molecular catalyst and organic dye-sensitized p-type nanostructured NiO. *Chem. Commun.* **2012**, *48*, 988–990.
- (134) Green, A. N. M.; Palomares, E.; Haque, S. A.; Kroon, J. M.; Durrant, J. R. Charge Transport versus Recombination in Dye-Sensitized Solar Cells Employing Nanocrystalline TiO<sub>2</sub> and SnO<sub>2</sub> Films. *J. Phys. Chem. B* **2005**, *109*, 12525–12533.
- (135) Brennaman, M. K.; Patrocinio, A. O. T.; Song, W.-J.; Jurss, J. W.; Concepcion, J. J.; Hoertz, P. G.; Traub, M. C.; Murakami Ihara, N. Y.; Meyer, T. J. Interfacial Electron Transfer Dynamics Following Laser Flash Photolysis of  $[\text{Ru}(\text{bpy})_2((4,4'\text{-PO}_3\text{H}_2)_2\text{bpy})]^{2+}$  in TiO<sub>2</sub> Nanoparticle Films in Aqueous Environments. *ChemSusChem* **2011**, *4*, 216–227.
- (136) Hanson, K.; Brennaman, M. K.; Ito, A.; Luo, H.; Song, W.; Parker, K. A.; Ghosh, R.; Norris, M. R.; Glasson, C. R. K.; Concepcion, J. J.; et al. Structure-Property Relationships in Phosphonate-Derivatized, RuII Polypyridyl Dyes on Metal Oxide Surfaces in an Aqueous Environment. *J. Phys. Chem. C* **2012**, *116*, 14837–14847.
- (137) Knauf, R. R.; Brennaman, M. K.; Alibabaei, L.; Norris, M. R.; Dempsey, J. L. Revealing the Relationship between Semiconductor Electronic Structure and Electron Transfer Dynamics at Metal Oxide-Chromophore Interfaces. *J. Phys. Chem. C* **2013**, *117*, 25259–25268.
- (138) Nayak, A.; Knauf, R. R.; Hanson, K.; Alibabaei, L.; Concepcion, J. J.; Ashford, D. L.; Dempsey, J. L.; Meyer, T. J. Synthesis and photophysical characterization of porphyrin and porphyrin-Ru(ii) polypyridyl chromophore–catalyst assemblies on mesoporous metal oxides. *Chemical Science* **2014**, *5*, 3115–3119.
- (139) Arai, T.; Sato, S.; Kajino, T.; Morikawa, T. Solar CO<sub>2</sub> reduction using H<sub>2</sub>O by a semiconductor/metal-complex hybrid photocatalyst: enhanced efficiency and demonstration of a wireless system using SrTiO<sub>3</sub> photoanodes. *Energy Environ. Sci.* **2013**, *6*, 1274–1282.
- (140) Sato, S.; Arai, T.; Morikawa, T.; Uemura, K.; Suzuki, T. M.; Tanaka, H.; Kajino, T. Selective CO<sub>2</sub> Conversion to Formate Conjugated with H<sub>2</sub>O Oxidation Utilizing Semiconductor/Complex Hybrid Photocatalysts. *J. Am. Chem. Soc.* **2011**, *133*, 15240–15243.
- (141) Luo, H.; Song, W.; Hoertz, P. G.; Hanson, K.; Ghosh, R.; Rangan, S.; Brennaman, M. K.; Concepcion, J. J.; Binstead, R. A.; Bartynski, R. A.; et al. A Sensitized Nb<sub>2</sub>O<sub>5</sub> Photoanode for Hydrogen Production in a Dye-Sensitized Photoelectrosynthesis Cell. *Chem. Mater.* **2013**, *25*, 122–131.
- (142) Zheng, H.; Tachibana, Y.; Kalantar-zadeh, K. Dye-sensitized solar cells based on WO<sub>3</sub>. *Langmuir* **2010**, *26*, 19148–19152.
- (143) Sadek, A. Z.; Zheng, H.; Breedon, M.; Bansal, V.; Bhargava, S. K.; Latham, K.; Zhu, J.; Yu, L.; Hu, Z.; Spizzirri, P. G.; et al. High-Temperature Anodized WO<sub>3</sub> Nanoplatelet Films for Photosensitive Devices. *Langmuir* **2009**, *25*, 9545–9551.
- (144) Anta, J. A.; Guillen, E.; Tena-Zaera, R. ZnO-Based Dye-Sensitized Solar Cells. *J. Phys. Chem. C* **2012**, *116*, 11413–11425.
- (145) Xu, F.; Sun, L. Solution-derived ZnO nanostructures for photoanodes of dye-sensitized solar cells. *Energy Environ. Sci.* **2011**, *4*, 818–841.

- (146) Lenzmann, F.; Krueger, J.; Burnside, S.; Brooks, K.; Graetzel, M.; Gal, D.; Ruehle, S.; Cahen, D. Surface Photovoltage Spectroscopy of Dye-Sensitized Solar Cells with TiO<sub>2</sub>, Nb<sub>2</sub>O<sub>5</sub>, and SrTiO<sub>3</sub> Nanocrystalline Photoanodes: Indication for Electron Injection from Higher Excited Dye States. *J. Phys. Chem. B* **2001**, *105*, 6347–6352.
- (147) Coutts, T. J.; Young, D. L.; Li, X.; Mulligan, W. P.; Wu, X. Search for improved transparent conducting oxides: A fundamental investigation of CdO, Cd<sub>2</sub>SnO<sub>4</sub>, and Zn<sub>2</sub>SnO<sub>4</sub>. *J. Vac. Sci. Technol., A* **2000**, *18*, 2646–2660.
- (148) Yang, S.-M.; Kou, H.-Z.; Wang, H.-J.; Cheng, K.; Wang, J.-C. Preparation and Band Energetics of Transparent Nanostructured SrTiO<sub>3</sub> Film Electrodes. *J. Phys. Chem. C* **2010**, *114*, 815–819.
- (149) Burnside, S.; Moser, J.-E.; Brooks, K.; Graetzel, M.; Cahen, D. Nanocrystalline Mesoporous Strontium Titanate as Photoelectrode Material for Photosensitized Solar Devices: Increasing Photovoltage through Flatband Potential Engineering. *J. Phys. Chem. B* **1999**, *103*, 9328–9332.
- (150) Zou, C.; Wrighton, M. S. Synthesis of octamethylferrocene derivatives via reaction of (octamethylferrocenyl)methyl carbocation with nucleophiles and application to functionalization of surfaces. *J. Am. Chem. Soc.* **1990**, *112*, 7578–7584.
- (151) McNamara, W. R.; Milot, R. L.; Song, H.-e.; Snoeberger, R. C., III; Batista, V. S.; Schmuttenmaer, C. A.; Brudvig, G. W.; Crabtree, R. H. Water-stable, hydroxamate anchors for functionalization of TiO<sub>2</sub> surfaces with ultrafast interfacial electron transfer. *Energy Environ. Sci.* **2010**, *3*, 917–923.
- (152) Haller, I. Covalently attached organic monolayers on semiconductor surfaces. *J. Am. Chem. Soc.* **1978**, *100*, 8050–8055.
- (153) McNamara, W. R.; Snoeberger, R. C.; Li, G.; Schleicher, J. M.; Cady, C. W.; Poyatos, M.; Schmuttenmaer, C. A.; Crabtree, R. H.; Brudvig, G. W.; Batista, V. S. Acetylacetone Anchors for Robust Functionalization of TiO<sub>2</sub> Nanoparticles with Mn(II)-Terpyridine Complexes. *J. Am. Chem. Soc.* **2008**, *130*, 14329–14338.
- (154) Hanson, K.; Brennaman, M. K.; Luo, H.; Glasson, C. R. K.; Concepcion, J. J.; Song, W.; Meyer, T. J. Photostability of Phosphonate-Derivatized, Ru(II) Polypyridyl Complexes on Metal Oxide Surfaces. *ACS Appl. Mater. Interfaces* **2012**, *4*, 1462–1469.
- (155) Brown, D. G.; Schauer, P. A.; Bora-Garcia, J.; Fancy, B. R.; Berlinguette, C. P. Stabilization of Ruthenium Sensitizers to TiO<sub>2</sub> Surfaces through Cooperative Anchoring Groups. *J. Am. Chem. Soc.* **2013**, *135*, 1692–1695.
- (156) Hanson, K.; Losego, M. D.; Kalanyan, B.; Ashford, D. L.; Parsons, G. N.; Meyer, T. J. Stabilization of [Ru(bpy)<sub>2</sub>(4,4'-(PO<sub>3</sub>H<sub>2</sub>)bpy)]<sup>2+</sup> on Mesoporous TiO<sub>2</sub> with Atomic Layer Deposition of Al<sub>2</sub>O<sub>3</sub>. *Chem. Mater.* **2013**, *25*, 3–5.
- (157) Hanson, K.; Losego, M. D.; Kalanyan, B.; Parsons, G. N.; Meyer, T. J. Stabilizing Small Molecules on Metal Oxide Surfaces Using Atomic Layer Deposition. *Nano Lett.* **2013**, *13*, 4802–4809.
- (158) Losego, M. D.; Hanson, K. Stabilizing molecular sensitizers in aqueous environs. *Nano Energy* **2013**, *2*, 1067–1069.
- (159) Vannucci, A. K.; Alibabaei, L.; Losego, M. D.; Concepcion, J. J.; Kalanyan, B.; Parsons, G. N.; Meyer, T. J. Crossign the Divide Between Homogenous and Heterogeneous Catalysis. *Proc. Natl. Acad. Sci. U. S. A.* **2013**, *110*, 20918–20922.
- (160) Son, H.-J.; Wang, X.; Prasittichai, C.; Jeong, N. C.; Aaltonen, T.; Gordon, R. G.; Hupp, J. T. Glass-Encapsulated Light Harvesters: More Efficient Dye-Sensitized Solar Cells by Deposition of Self-Aligned, Conformal, and Self-Limited Silica Layers. *J. Am. Chem. Soc.* **2012**, *134*, 9537–9540.
- (161) Son, H.-J.; Prasittichai, C.; Mondloch, J. E.; Luo, L.; Wu, J.; Kim, D. W.; Farha, O. K.; Hupp, J. T. Dye Stabilization and Enhanced Photoelectrode Wettability in Water-Based Dye-Sensitized Solar Cells through Post-assembly Atomic Layer Deposition of TiO<sub>2</sub>. *J. Am. Chem. Soc.* **2013**, *135*, 11529–11532.
- (162) Antila, L. J.; Heikkila, M. J.; Makinen, V.; Humalamaki, N.; Laitinen, M.; Linko, V.; Jalkanen, P.; Toppuri, J.; Aumanen, V.; Kemell, M.; et al. ALD Grown Aluminum Oxide Submonolayers in Dye-Sensitized Solar Cells: The Effect on Interfacial Electron Transfer and Performance. *J. Phys. Chem. C* **2011**, *115*, 16720–16729.
- (163) Prasittichai, C.; Hupp, J. T. Surface Modification of SnO<sub>2</sub> Photoelectrodes in Dye-Sensitized Solar Cells: Significant Improvements in Photovoltage via Al<sub>2</sub>O<sub>3</sub> Atomic Layer Deposition. *J. Phys. Chem. Lett.* **2010**, *1*, 1611–1615.
- (164) Wee, K.-R.; Brennaman, M. K.; Alibabaei, L.; Farnum, B. H.; Sherman, B.; Lapides, A. M.; Meyer, T. J. Stabilization of Ruthenium(II) Polypyridyl Chromophores on Nanoparticle Metal-Oxide Electrodes in Water by Hydrophobic PMMA Overlays. *J. Am. Chem. Soc.* **2014**, *136*, 13514–13517.
- (165) Ashford, D. L.; Lapides, A. M.; Vannucci, A. K.; Hanson, K.; Torelli, D. A.; Harrison, D. P.; Templeton, J. L.; Meyer, T. J. Water Oxidation by an Electropolymerized Catalyst on Derivatized Mesoporous Metal Oxide Electrodes. *J. Am. Chem. Soc.* **2014**, *136*, 6578–6581.
- (166) Lapides, A. M.; Ashford, D. L.; Hanson, K.; Torelli, D. A.; Templeton, J. L.; Meyer, T. J. Stabilization of a Ruthenium(II) Polypyridyl Dye on Nanocrystalline TiO<sub>2</sub> by an Electropolymerized Overlay. *J. Am. Chem. Soc.* **2013**, *135*, 15450–15458.
- (167) Ashford, D. L.; Sherman, B. D.; Binstead, R. A.; Templeton, J. L.; Meyer, T. J. Electro-Assembly of a Chromophore–Catalyst Bilayer for Water Oxidation and Photocatalytic Water Splitting. *Angew. Chem., Int. Ed.* **2015**, *54*, 4778–4781.
- (168) Liu, F.; Concepcion, J. J.; Jurss, J. W.; Cardolaccia, T.; Templeton, J. L.; Meyer, T. J. Mechanisms of Water Oxidation from the Blue Dimer to Photosystem II. *Inorg. Chem.* **2008**, *47*, 1727–1752.
- (169) Akimov, A. V.; Neukirch, A. J.; Prezhdo, O. V. Theoretical Insights into Photoinduced Charge Transfer and Catalysis at Oxide Interfaces. *Chem. Rev.* **2013**, *113*, 4496–4565.
- (170) Kaerkaes, M. D.; Verho, O.; Johnston, E. V.; Aakermark, B. Artificial Photosynthesis: Molecular Systems for Catalytic Water Oxidation. *Chem. Rev.* **2014**, *114*, 11863–12001.
- (171) Ardo, S.; Meyer, G. J. Photodriven heterogeneous charge transfer with transition-metal compounds anchored to TiO<sub>2</sub> semiconductor surfaces. *Chem. Soc. Rev.* **2009**, *38*, 115–164.
- (172) Li, J.; Djurovich, P. I.; Alleyne, B. D.; Yousufuddin, M.; Ho, N. N.; Thomas, J. C.; Peters, J. C.; Bau, R.; Thompson, M. E. Synthetic Control of Excited-State Properties in Cyclometalated Ir(III) Complexes Using Ancillary Ligands. *Inorg. Chem.* **2005**, *44*, 1713–1727.
- (173) Chen, P.; Meyer, T. J. Medium Effects on Charge Transfer in Metal Complexes. *Chem. Rev.* **1998**, *98*, 1439–1477.
- (174) Juban, E. A.; Smeigh, A. L.; Monat, J. E.; McCusker, J. K. Ultrafast dynamics of ligand-field excited states. *Coord. Chem. Rev.* **2006**, *250*, 1783–1791.
- (175) Kalyanasundaram, K. Photophysics, photochemistry and solar energy conversion with tris(bipyridyl)ruthenium(II) and its analogs. *Coord. Chem. Rev.* **1982**, *46*, 159–244.
- (176) Huynh, M. H. V.; Dattelbaum, D. M.; Meyer, T. J. Exited state electron and energy transfer in molecular assemblies. *Coord. Chem. Rev.* **2005**, *249*, 457–483.
- (177) Anderson, P. A.; Strouse, G. F.; Treadway, J. A.; Keene, F. R.; Meyer, T. J. Black MLCT Absorbers. *Inorg. Chem.* **1994**, *33*, 3863–3864.
- (178) Kakiage, K.; Aoyama, Y.; Yano, T.; Oya, K.; Kyomen, T.; Hanaya, M. Fabrication of a high-performance dye-sensitized solar cell with 12.8% conversion efficiency using organic silyl-anchor dyes. *Chem. Commun.* **2015**, *51*, 6315–6317.
- (179) Martinez-Diaz, M. V.; de la Torre, G.; Torres, T. Lighting porphyrins and phthalocyanines for molecular photovoltaics. *Chem. Commun.* **2010**, *46*, 7090–7108.
- (180) Wang, Z.-S.; Koumura, N.; Cui, Y.; Takahashi, M.; Sekiguchi, H.; Mori, A.; Kubo, T.; Furube, A.; Hara, K. Hexylthiophene-Functionalized Carbazole Dyes for Efficient Molecular Photovoltaics: Tuning of Solar-Cell Performance by Structural Modification. *Chem. Mater.* **2008**, *20*, 3993–4003.
- (181) Jeon, N. J.; Noh, J. H.; Yang, W. S.; Kim, Y. C.; Ryu, S.; Seo, J.; Seok, S. I. Compositional engineering of perovskite materials for high-performance solar cells. *Nature* **2015**, *517*, 476–480.

- (182) Gagliardi, C. J.; Westlake, B. C.; Kent, C. A.; Paul, J. J.; Papanikolas, J. M.; Meyer, T. J. Integrating proton coupled electron transfer (PCET) and excited states. *Coord. Chem. Rev.* **2010**, *254*, 2459–2471.
- (183) McEvoy, J. P.; Brudvig, G. W. Water-splitting chemistry of photosystem II. *Chem. Rev.* **2006**, *106*, 4455–4483.
- (184) Barber, J.; Ferreira, K.; Maghlaoui, K.; Iwata, S. Structural model of the oxygen-evolving centre of photosystem II with mechanistic implications. *Phys. Chem. Chem. Phys.* **2004**, *6*, 4737–4742.
- (185) Ishikita, H.; Saenger, W.; Loll, B.; Biesiadka, J.; Knapp, E.-W. Energetics of a Possible Proton Exit Pathway for Water Oxidation in Photosystem II. *Biochemistry* **2006**, *45*, 2063–2071.
- (186) Farnum, B. H.; Morseth, Z. A.; Brennaman, M. K.; Papanikolas, J. M.; Meyer, T. J. Driving Force Dependent, Photo-induced Electron Transfer at Degenerately Doped, Optically Transparent Semiconductor Nanoparticle Interfaces. *J. Am. Chem. Soc.* **2014**, *136*, 15869–15872.
- (187) Farnum, B. H.; Morseth, Z. A.; Brennaman, M. K.; Papanikolas, J. M.; Meyer, T. J. Application of Degenerately Doped Metal Oxides in the Study of Photoinduced Interfacial Electron Transfer. *J. Phys. Chem. B* **2015**, *119*, 7698–7711.
- (188) Alstrum-Acevedo, J. H.; Brennaman, M. K.; Meyer, T. J. Chemical Approaches to Artificial Photosynthesis. 2. *Inorg. Chem.* **2005**, *44*, 6802–6827.
- (189) Ulstrup, J.; Jortner, J. Effect of intramolecular quantum modes on free energy relations for electron transfer reactions. *J. Chem. Phys.* **1975**, *63*, 4358–4368.
- (190) Kestner, N. R.; Logan, J.; Jortner, J. Thermal electron transfer reactions in polar solvents. *J. Phys. Chem.* **1974**, *78*, 2148–2166.
- (191) Jortner, J. Temperature dependent activation energy for electron transfer between biological molecules. *J. Chem. Phys.* **1976**, *64*, 4860–4867.
- (192) Sutin, N. Theory of electron transfer reactions: insights and hindsights. *Prog. Inorg. Chem.* **1983**, *30*, 441–498.
- (193) Meyer, T. J.; Taube, H. In *Comprehensive Coordination Chemistry, The Synthesis, Reactions, Properties and Applications of Coordination Compounds*; Pergamon Press: Oxford, U.K., 1987; Vol. 1.
- (194) Kim, H. B.; Kitamura, N.; Tazuke, S. Time-dependent nonradiative decay in the metal-to-ligand charge-transfer excited state of tris(2,2'-bipyridine)ruthenium(2+). *J. Phys. Chem.* **1990**, *94*, 7401–7405.
- (195) Ito, A.; Meyer, T. J. The Golden Rule. Application for fun and profit in electron transfer, energy transfer, and excited-state decay. *Phys. Chem. Chem. Phys.* **2012**, *14*, 13731–13745.
- (196) Giokas, P. G.; Miller, S. A.; Hanson, K.; Norris, M. R.; Glasson, C. R. K.; Concepcion, J. J.; Bettis, S. E.; Meyer, T. J.; Moran, A. M. Spectroscopy and Dynamics of Phosphonate-Derivatized Ruthenium Complexes on TiO<sub>2</sub>. *J. Phys. Chem. C* **2013**, *117*, 812–824.
- (197) Caspar, J. V.; Meyer, T. J. Photochemistry of tris(2,2'-bipyridine)ruthenium(2+) ion (Ru(bpy)<sub>3</sub><sup>2+</sup>). Solvent effects. *J. Am. Chem. Soc.* **1983**, *105*, 5583–5590.
- (198) Kestell, J. D.; Williams, Z. L.; Stultz, L. K.; Claude, J. P. Medium Dependence of Intramolecular Vibrational Modes Coupled to MLCT Transitions in Metal Polypyridyl Complexes. *J. Phys. Chem. A* **2002**, *106*, 5768–5778.
- (199) Nozaki, K.; Takamori, K.; Nakatsugawa, Y.; Ohno, T. Theoretical Studies of Phosphorescence Spectra of Tris(2,2'-bipyridine) Transition Metal Compounds. *Inorg. Chem.* **2006**, *45*, 6161–6178.
- (200) Ardo, S.; Sun, Y.; Castellano, F. N.; Meyer, G. J. Excited-State Electron Transfer from Ruthenium-Polypyridyl Compounds to Anatase TiO<sub>2</sub> Nanocrystallites: Evidence for a Stark Effect. *J. Phys. Chem. B* **2010**, *114*, 14596–14604.
- (201) Miller, S. A.; West, B. A.; Curtis, A. C.; Papanikolas, J. M.; Moran, A. M. Communication: Uncovering molecule-TiO<sub>2</sub> interactions with nonlinear spectroscopy. *J. Chem. Phys.* **2011**, *135*, 081101–081104.
- (202) Hannappel, T.; Burfeindt, B.; Storck, W.; Willig, F. Measurement of ultrafast photoinduced electron transfer from chemically anchored Ru-dye molecules into empty electronic states in a colloidal anatase TiO<sub>2</sub> film. *J. Phys. Chem. B* **1997**, *101*, 6799–6802.
- (203) Tachibana, Y.; Haque, S. A.; Mercer, I. P.; Durrant, J. R.; Klug, D. R. Electron Injection and Recombination in Dye Sensitized Nanocrystalline Titanium Dioxide Films: A Comparison of Ruthenium Bipyridyl and Porphyrin Sensitizer Dyes. *J. Phys. Chem. B* **2000**, *104*, 1198–1205.
- (204) Tachibana, Y.; Moser, J. E.; Graetzel, M.; Klug, D. R.; Durrant, J. R. Subpicosecond interfacial charge separation in dye-sensitized nanocrystalline titanium dioxide films. *J. Phys. Chem.* **1996**, *100*, 20056–20062.
- (205) Doyle, R. L.; Godwin, I. J.; Brandon, M. P.; Lyons, M. E. G. Redox and electrochemical water splitting catalytic properties of hydrated metal oxide modified electrodes. *Phys. Chem. Chem. Phys.* **2013**, *15*, 13737–13783.
- (206) Jiao, F.; Frei, H. Nanostructured cobalt and manganese oxide clusters as efficient water oxidation catalysts. *Energy Environ. Sci.* **2010**, *3*, 1018–1027.
- (207) Fang, Y.-H.; Liu, Z.-P. Mechanism and Tafel lines of electro-oxidation of water to oxygen on RuO<sub>2</sub>(110). *J. Am. Chem. Soc.* **2010**, *132*, 18214–18222.
- (208) Winther-Jensen, B.; Winther-Jensen, O.; Forsyth, M.; MacFarlane, D. R. High Rates of Oxygen Reduction over a Vapor Phase-Polymerized PEDOT Electrode. *Science* **2008**, *321*, 671–674.
- (209) Da Silva, L. M.; Boodts, J. F. C.; De Faria, L. A. Oxygen evolution at RuO<sub>2</sub>(x)+Co<sub>3</sub>O<sub>4</sub>(1-x) electrodes from acid solution. *Electrochim. Acta* **2001**, *46*, 1369–1375.
- (210) Jirkovsky, J.; Makarova, M.; Krtil, P. Particle size dependence of oxygen evolution reaction on nanocrystalline RuO<sub>2</sub> and Ru<sub>0.8</sub>Co<sub>0.2</sub>O<sub>2-x</sub>. *Electrochim. Commun.* **2006**, *8*, 1417–1422.
- (211) Bertoncello, R.; Cattarin, S.; Frateur, I.; Musiani, M. Preparation of anodes for oxygen evolution by electrodeposition of composite oxides of Pb and Ru on Ti. *J. Electroanal. Chem.* **2000**, *492*, 145–149.
- (212) Hurst, J. K. Water oxidation catalyzed by dimeric  $\mu$ -oxo bridged ruthenium diimine complexes. *Coord. Chem. Rev.* **2005**, *249*, 313–328.
- (213) Gersten, S. W.; Samuels, G. J.; Meyer, T. J. Catalytic oxidation of water by an oxo-bridged ruthenium dimer. *J. Am. Chem. Soc.* **1982**, *104*, 4029–4030.
- (214) Jurss, J. W.; Concepcion, J. J.; Butler, J. M.; Omberg, K. M.; Baraldo, L. M.; Thompson, D. G.; Lebeau, E. L.; Hornstein, B.; Schoonover, J. R.; Jude, H.; et al. Electronic Structure of the Water Oxidation Catalyst *cis,cis*-[(bpy)<sub>2</sub>(H<sub>2</sub>O)](Ru<sup>III</sup>ORu<sup>III</sup>)-O-<sup>III</sup>(OH<sub>2</sub>)(bpy)<sub>2</sub>]<sup>4+</sup>, The Blue Dimer. *Inorg. Chem.* **2012**, *51*, 1345–1358.
- (215) Jurss, J. W.; Concepcion, J. C.; Norris, M. R.; Templeton, J. L.; Meyer, T. J. Surface Catalysis of Water Oxidation by the Blue Ruthenium Dimer. *Inorg. Chem.* **2010**, *49*, 3980–3982.
- (216) Concepcion, J. J.; Jurss, J. W.; Templeton, J. L.; Meyer, T. J. Mediator-assisted water oxidation by the ruthenium "blue dimer" *cis,cis*-[(bpy)<sub>2</sub>(H<sub>2</sub>O)RuORu(OH<sub>2</sub>)(bpy)<sub>2</sub>]<sup>4+</sup>. *Proc. Natl. Acad. Sci. U. S. A.* **2008**, *105*, 17632–17635.
- (217) Chen, Z.; Concepcion, J. J.; Jurss, J. W.; Meyer, T. J. Single-Site, Catalytic Water Oxidation on Oxide Surfaces. *J. Am. Chem. Soc.* **2009**, *131*, 15580–15581.
- (218) Concepcion, J. J.; Jurss, J. W.; Hoertz, P. G.; Meyer, T. J. Catalytic and Surface-Electrocatalytic Water Oxidation by Redox Mediator-Catalyst Assemblies. *Angew. Chem., Int. Ed.* **2009**, *48*, 9473–9476.
- (219) Zong, R.; Thummel, R. P. A New Family of Ru Complexes for Water Oxidation. *J. Am. Chem. Soc.* **2005**, *127*, 12802–12803.
- (220) Tseng, H.-W.; Zong, R.; Muckerman, J. T.; Thummel, R. Mononuclear Ruthenium(II) Complexes That Catalyze Water Oxidation. *Inorg. Chem.* **2008**, *47*, 11763–11773.

- (221) Chen, Z.; Concepcion, J. J.; Hull, J. F.; Hoertz, P. G.; Meyer, T. J. Catalytic water oxidation on derivatized nanoITO. *Dalton Transactions* **2010**, *39*, 6950–6952.
- (222) Duan, L.; Bozoglian, F.; Mandal, S.; Stewart, B.; Privalov, T.; Llobet, A.; Sun, L. A molecular ruthenium catalyst with water-oxidation activity comparable to that of photosystem II. *Nat. Chem.* **2012**, *4*, 418–423.
- (223) Duan, L.; Wang, L.; Inge, A. K.; Fischer, A.; Zou, X.; Sun, L. Insights into Ru-Based Molecular Water Oxidation Catalysts: Electronic and Noncovalent-Interaction Effects on Their Catalytic Activities. *Inorg. Chem.* **2013**, *52*, 7844–7852.
- (224) Li, F.; Zhang, B.; Li, X.; Jiang, Y.; Chen, L.; Li, Y.; Sun, L. Highly Efficient Oxidation of Water by a Molecular Catalyst Immobilized on Carbon Nanotubes. *Angew. Chem., Int. Ed.* **2011**, *50*, 12276–12279.
- (225) Wasylenko, D. J.; Ganeshamoorthy, C.; Koivisto, B. D.; Henderson, M. A.; Berlinguet, C. P. Insight into Water Oxidation by Mononuclear Polypyridyl Ru Catalysts. *Inorg. Chem.* **2010**, *49*, 2202–2209.
- (226) Badiee, Y. M.; Polyansky, D. E.; Muckerman, J. T.; Szalda, D. J.; Haberdrar, R.; Zong, R.; Thummel, R. P.; Fujita, E. Water Oxidation with Mononuclear Ruthenium(II) Polypyridine Complexes Involving a Direct RuIV=O Pathway in Neutral and Alkaline Media. *Inorg. Chem.* **2013**, *52*, 8845–8850.
- (227) Sala, X.; Maji, S.; Bofill, R.; Garcia-Antón, J.; Escriche, L.; Llobet, A. Molecular Water Oxidation Mechanisms Followed by Transition Metals: State of the Art. *Acc. Chem. Res.* **2014**, *47*, 504–516.
- (228) Hull, J. F.; Balcells, D.; Blakemore, J. D.; Incarvito, C. D.; Eisenstein, O.; Brudvig, G. W.; Crabtree, R. H. Highly Active and Robust Cp<sup>\*</sup> Iridium Complexes for Catalytic Water Oxidation. *J. Am. Chem. Soc.* **2009**, *131*, 8730–8731.
- (229) Blakemore, J. D.; Schley, N. D.; Balcells, D.; Hull, J. F.; Olack, G. W.; Incarvito, C. D.; Eisenstein, O.; Brudvig, G. W.; Crabtree, R. H. Half-Sandwich Iridium Complexes for Homogeneous Water-Oxidation Catalysis. *J. Am. Chem. Soc.* **2010**, *132*, 16017–16029.
- (230) Schley, N. D.; Blakemore, J. D.; Subbaiyan, N. K.; Incarvito, C. D.; D’Souza, F.; Crabtree, R. H.; Brudvig, G. W. Distinguishing Homogeneous from Heterogeneous Catalysis in Electrode-Driven Water Oxidation with Molecular Iridium Complexes. *J. Am. Chem. Soc.* **2011**, *133*, 10473–10481.
- (231) Joya, K. S.; Subbaiyan, N. K.; D’Souza, F.; de Groot, H. J. M. Surface-Immobilized Single-Site Iridium Complexes for Electrocatalytic Water Splitting. *Angew. Chem., Int. Ed.* **2012**, *51*, 9601–9605.
- (232) McDaniel, N. D.; Coughlin, F. J.; Tinker, L. L.; Bernhard, S. Cyclometalated Iridium(III) Aquo Complexes: Efficient and Tunable Catalysts for the Homogeneous Oxidation of Water. *J. Am. Chem. Soc.* **2008**, *130*, 210–217.
- (233) Savini, A.; Bellachioma, G.; Ciancaleoni, G.; Zuccaccia, C.; Zuccaccia, D.; Macchioni, A. Iridium(III) molecular catalysts for water oxidation: the simpler the faster. *Chem. Commun.* **2010**, *46*, 9218–9219.
- (234) Wasylenko, D. J.; Ganeshamoorthy, C.; Borau-García, J.; Berlinguet, C. P. Electrochemical evidence for catalytic water oxidation mediated by a high-valent cobalt complex. *Chem. Commun.* **2011**, *47*, 4249–4251.
- (235) Dogutan, D. K.; McGuire, R.; Nocera, D. G. Electrocatalytic Water Oxidation by Cobalt(III) Hangman β-Octafluoro Corroles. *J. Am. Chem. Soc.* **2011**, *133*, 9178–9180.
- (236) Barnett, S. M.; Goldberg, K. I.; Mayer, J. M. A soluble copper-bipyridine water-oxidation electrocatalyst. *Nat. Chem.* **2012**, *4*, 498–502.
- (237) Codola, Z.; Garcia-Bosch, I.; Acuna-Pares, F.; Prat, I.; Luis, J. M.; Costas, M.; Lloret-Fillol, J. Electronic Effects on Single-Site Iron Catalysts for Water Oxidation. *Chem. - Eur. J.* **2013**, *19*, 8042–8047.
- (238) Ellis, W. C.; McDaniel, N. D.; Bernhard, S.; Collins, T. J. Fast Water Oxidation Using Iron. *J. Am. Chem. Soc.* **2010**, *132*, 10990–10991.
- (239) Fillol, J. L.; Codola, Z.; Garcia-Bosch, I.; Gomez, L.; Pla, J. J.; Costas, M. Efficient water oxidation catalysts based on readily available iron coordination complexes. *Nat. Chem.* **2011**, *3*, 807–813.
- (240) Joya, K. S.; Valles-Pardo, J. L.; Joya, Y. F.; Eisenmayer, T.; Thomas, B.; Buda, F.; de Groot, H. J. M. Molecular Catalytic Assemblies for Electrodriven Water Splitting. *ChemPlusChem* **2013**, *78*, 35–47.
- (241) Wasylenko, D. J.; Palmer, R. D.; Berlinguet, C. P. Homogeneous water oxidation catalysts containing a single metal site. *Chem. Commun.* **2013**, *49*, 218–227.
- (242) Cao, R.; Lai, W.; Du, P. Catalytic water oxidation at single metal sites. *Energy Environ. Sci.* **2012**, *5*, 8134–8157.
- (243) Singh, A.; Spiccia, L. Water oxidation catalysts based on abundant 1st row transition metals. *Coord. Chem. Rev.* **2013**, *257*, 2607–2622.
- (244) Hintermair, U.; Sheehan, S. W.; Parent, A. R.; Ess, D. H.; Richens, D. T.; Vaccaro, P. H.; Brudvig, G. W.; Crabtree, R. H. Precursor Transformation during Molecular Oxidation Catalysis with Organometallic Iridium Complexes. *J. Am. Chem. Soc.* **2013**, *135*, 10837–10851.
- (245) Blakemore, J. D.; Mara, M. W.; Kushner-Lenhoff, M. N.; Schley, N. D.; Konezny, S. J.; Rivalta, I.; Negre, C. F. A.; Snoeberger, R. C.; Kokhan, O.; Huang, J.; et al. Characterization of an Amorphous Iridium Water-Oxidation Catalyst Electrodeposited from Organometallic Precursors. *Inorg. Chem.* **2013**, *52*, 1860–1871.
- (246) Wang, D.; Groves, J. T. Efficient water oxidation catalyzed by homogeneous cationic cobalt porphyrins with critical roles for the buffer base. *Proc. Natl. Acad. Sci. U. S. A.* **2013**, *110*, 15579–15584.
- (247) Lopez, A. M.; Natali, M.; Pizzolato, E.; Chiorboli, C.; Bonchio, M.; Sartorel, A.; Scandola, F. A Co(II)-Ru(II) dyad relevant to light-driven water oxidation catalysis. *Phys. Chem. Chem. Phys.* **2014**, *16*, 12000–12007.
- (248) Chen, Z. F.; Meyer, T. J. Copper(II) Catalysis of Water Oxidation. *Angew. Chem., Int. Ed.* **2013**, *52*, 700–703.
- (249) Zhang, M. T.; Chen, Z. F.; Kang, P.; Meyer, T. J. Electrocatalytic Water Oxidation with a Copper(II) Polypeptide Complex. *J. Am. Chem. Soc.* **2013**, *135*, 2048–2051.
- (250) de Oliveira, F. T.; Chanda, A.; Banerjee, D.; Shan, X.; Mondal, S.; Que, L., Jr.; Bominaar, E. L.; Muenck, E.; Collins, T. J. Chemical and spectroscopic evidence for an FeV-Oxo Complex. *Science* **2007**, *315*, 835–838.
- (251) Gagliardi, C. J.; Vannucci, A. K.; Concepcion, J. J.; Chen, Z. F.; Meyer, T. J. The role of proton coupled electron transfer in water oxidation. *Energy Environ. Sci.* **2012**, *5*, 7704–7717.
- (252) Lin, X.; Hu, X.; Concepcion, J. J.; Chen, Z.; Liu, S.; Meyer, T. J.; Yang, W. Theoretical study of catalytic mechanism for single-site water oxidation process. *Proc. Natl. Acad. Sci. U. S. A.* **2012**, *109*, 15669–15672.
- (253) Hughes, T. F.; Friesner, R. A. Systematic Investigation of the Catalytic Cycle of a Single Site Ruthenium Oxygen Evolving Complex Using Density Functional Theory. *J. Phys. Chem. B* **2011**, *115*, 9280–9289.
- (254) Duan, L.; Fischer, A.; Xu, Y.; Sun, L. Isolated Seven-Coordinate Ru(IV) Dimer Complex with [HOHOH]– Bridging Ligand as an Intermediate for Catalytic Water Oxidation. *J. Am. Chem. Soc.* **2009**, *131*, 10397–10399.
- (255) Dau, H.; Limberg, C.; Reier, T.; Risch, M.; Roggan, S.; Strasser, P. The Mechanism of Water Oxidation: from Electrolysis via Homogeneous to Biological Catalysis. *ChemCatChem* **2010**, *2*, 724–761.
- (256) Cady, C. W.; Crabtree, R. H.; Brudvig, G. W. Functional models for the oxygen-evolving complex of photosystem II. *Coord. Chem. Rev.* **2008**, *252*, 444–455.
- (257) Chen, Z.; Concepcion, J. J.; Hu, X.; Yang, W.; Hoertz, P. G.; Meyer, T. J. Concerted O atom-proton transfer in the O-O bond forming step in water oxidation. *Proc. Natl. Acad. Sci. U. S. A.* **2010**, *107*, 7225–7229.
- (258) Chen, Z. F.; Concepcion, J. J.; Hu, X. Q.; Yang, W. T.; Hoertz, P. G.; Meyer, T. J. Concerted O atom-proton transfer in the O-O

- bond forming step in water oxidation. *Proc. Natl. Acad. Sci. U. S. A.* **2010**, *107*, 7225–7229.
- (259) Chen, Z. F.; Concepcion, J. J.; Luo, H. L.; Hull, J. F.; Paul, A.; Meyer, T. J. Nonaqueous Catalytic Water Oxidation. *J. Am. Chem. Soc.* **2010**, *132*, 17670–17673.
- (260) Duan, L.; Araujo, C. M.; Ahlquist, M. S. G.; Sun, L. Highly efficient and robust molecular ruthenium catalysts for water oxidation. *Proc. Natl. Acad. Sci. U. S. A.* **2012**, *109*, 15584–15588.
- (261) Concepcion, J. J.; Zhong, D. K.; Szalda, D. J.; Muckerman, J. T.; Fujita, E. Mechanism of water oxidation by [Ru(bda)(L)<sub>2</sub>]: the return of the "blue dimer". *Chem. Commun.* **2015**, *51*, 4105–4108.
- (262) Song, N.; Concepcion, J. J.; Binstead, R. A.; Rudd, J. A.; Vannucci, A. K.; Dares, C. J.; Coggins, M. K.; Meyer, T. J. Base Enhanced Catalytic Water Oxidation by a Carboxylate-Bipyridine Ru(II) Complex. *Proc. Natl. Acad. Sci. U. S. A.* **2015**, *112*, 4935–4940.
- (263) Chen, Z. F.; Concepcion, J. J.; Hull, J. F.; Hoertz, P. G.; Meyer, T. J. Catalytic water oxidation on derivatized nanoITO. *Dalton Trans.* **2010**, *39*, 6950–6952.
- (264) Hoertz, P. G.; Goldstein, A.; Donley, C.; Meyer, T. J. Using the Voids Evidence for an Antenna Effect in Dye-Sensitized Mesoporous TiO<sub>2</sub> Thin Films. *J. Phys. Chem. B* **2010**, *114*, 14772–14777.
- (265) Norris, M. R.; Concepcion, J. J.; Fang, Z.; Templeton, J. L.; Meyer, T. J. Low Overpotential Water Oxidation by a Surface-Bound Ruthenium-Chromophore-Ruthenium-Catalyst Assembly. *Angew. Chem., Int. Ed.* **2013**, *52*, 13580–13583.
- (266) Ashford, D. L.; Song, W. J.; Concepcion, J. J.; Glasson, C. R. K.; Brennaman, M. K.; Norris, M. R.; Fang, Z.; Templeton, J. L.; Meyer, T. J. Photoinduced Electron Transfer in a Chromophore-Catalyst Assembly Anchored to TiO<sub>2</sub>. *J. Am. Chem. Soc.* **2012**, *134*, 19189–19198.
- (267) Ashford, D. L.; Stewart, D. J.; Glasson, C. R.; Binstead, R. A.; Harrison, D. P.; Norris, M. R.; Concepcion, J. J.; Fang, Z.; Templeton, J. L.; Meyer, T. J. An Amide-Linked Chromophore-Catalyst Assembly for Water Oxidation. *Inorg. Chem.* **2012**, *51*, 6428–6430.
- (268) Wang, L.; Ashford, D. L.; Thompson, D. W.; Meyer, T. J.; Papanikolas, J. M. Watching Photoactivation in a Ru(II) Chromophore-Catalyst Assembly on TiO<sub>2</sub> by Ultrafast Spectroscopy. *J. Phys. Chem. C* **2013**, *117*, 24250–24258.
- (269) Song, W.; Glasson, C. R. K.; Luo, H.; Hanson, K.; Brennaman, M. K.; Concepcion, J. J.; Meyer, T. J. Photoinduced Stepwise Oxidative Activation of a Chromophore-Catalyst Assembly on TiO<sub>2</sub>. *J. Phys. Chem. Lett.* **2011**, *2*, 1808–1813.
- (270) Donovan, B.; Walker, L. A., II; Yocom, C. F.; Sension, R. J. Transient Absorption Studies of the Primary Charge Separation in Photosystem II. *J. Phys. Chem.* **1996**, *100*, 1945–1949.
- (271) Pullerits, T.; Sundstroem, V. Photosynthetic Light-Harvesting Pigment-Protein Complexes: Toward Understanding How and Why. *Acc. Chem. Res.* **1996**, *29*, 381–389.
- (272) Song, W.; Chen, Z.; Brennaman, M. K.; Concepcion, J. J.; Patrocino, A. O. T.; Iha, N. Y. M.; Meyer, T. J. Making solar fuels by artificial photosynthesis. *Pure Appl. Chem.* **2011**, *83*, 749–768.
- (273) Li, R.; Liu, J.; Cai, N.; Zhang, M.; Wang, P. Synchronously Reduced Surface States, Charge Recombination, and Light Absorption Length for High-Performance Organic Dye-Sensitized Solar Cells. *J. Phys. Chem. B* **2010**, *114*, 4461–4464.
- (274) Lai, H.; Hong, J.; Liu, P.; Yuan, C.; Li, Y.; Fang, Q. Multi-carbazole derivatives: new dyes for highly efficient dye-sensitized solar cells. *RSC Adv.* **2012**, *2*, 2427–2432.
- (275) Kim, M.-J.; Yu, Y.-J.; Kim, J.-H.; Jung, Y.-S.; Kay, K.-Y.; Ko, S.-B.; Lee, C.-R.; Jang, I.-H.; Kwon, Y.-U.; Park, N.-G. Tuning of spacer groups in organic dyes for efficient inhibition of charge recombination in dye-sensitized solar cells. *Dyes Pigm.* **2012**, *95*, 134–141.
- (276) Cowan, A. J.; Durrant, J. R. Long-lived charge separated states in nanostructured semiconductor photoelectrodes for the production of solar fuels. *Chem. Soc. Rev.* **2013**, *42*, 2281–2293.
- (277) Murakami, T. N.; Koumura, N.; Uchiyama, T.; Uemura, Y.; Obuchi, K.; Masaki, N.; Kimura, M.; Mori, S. Recombination inhibitive structure of organic dyes for cobalt complex redox electrolytes in dye-sensitized solar cells. *J. Mater. Chem. A* **2013**, *1*, 792–798.
- (278) Lin, C.; Tsai, F.-Y.; Lee, M.-H.; Lee, C.-H.; Tien, T.-C.; Wang, L.-P.; Tsai, S.-Y. Enhanced performance of dye-sensitized solar cells by an Al<sub>2</sub>O<sub>3</sub> charge-recombination barrier formed by low-temperature atomic layer deposition. *J. Mater. Chem.* **2009**, *19*, 2999–3003.
- (279) Hamann, T. W.; Farha, O. K.; Hupp, J. T. Outer-Sphere Redox Couples as Shuttles in Dye-Sensitized Solar Cells. Performance Enhancement Based on Photoelectrode Modification via Atomic Layer Deposition. *J. Phys. Chem. C* **2008**, *112*, 19756–19764.
- (280) Wu, M.; Yang, Z. H.; Jiang, Y. H.; Zhang, J. J.; Liu, S. Q.; Sun, Y. M. Improvement of dye-sensitized solar cell performance through electrodepositing a close-packed TiO<sub>2</sub> film. *J. Solid State Electrochem.* **2010**, *14*, 857–863.
- (281) Li, X.; Qiu, Y.; Wang, S.; Lu, S.; Gruar, R. I.; Zhang, X.; Darr, J. A.; He, T. Electrophoretically deposited TiO<sub>2</sub> compact layers using aqueous suspension for dye-sensitized solar cells. *Phys. Chem. Chem. Phys.* **2013**, *15*, 14729–14735.
- (282) Kang, S. H.; Kim, J.-Y.; Kim, Y.; Kim, H. S.; Sung, Y.-E. Surface Modification of Stretched TiO<sub>2</sub> Nanotubes for Solid-State Dye-Sensitized Solar Cells. *J. Phys. Chem. C* **2007**, *111*, 9614–9623.
- (283) Song, J.; Yang, H. B.; Wang, X.; Khoo, S. Y.; Wong, C. C.; Liu, X.-W.; Li, C. M. Improved Utilization of Photogenerated Charge Using Fluorine-Doped TiO<sub>2</sub> Hollow Spheres Scattering Layer in Dye-Sensitized Solar Cells. *ACS Appl. Mater. Interfaces* **2012**, *4*, 3712–3717.
- (284) Yang, H. B.; Guo, C. X.; Guai, G. H.; Song, Q. L.; Jiang, S. P.; Li, C. M. Reduction of Charge Recombination by an Amorphous Titanium Oxide Interlayer in Layered Graphene/Quantum Dots Photochemical Cells. *ACS Appl. Mater. Interfaces* **2011**, *3*, 1940–1945.
- (285) Chen, Z.; Kang, P.; Zhang, M.-T.; Meyer, T. J. Making syngas electrocatalytically using a polypyridyl ruthenium catalyst. *Chem. Commun.* **2014**, *50*, 335–337.
- (286) Alibabaei, L.; Sherman, B. D.; Norris, M. R.; Brennaman, M. K.; Meyer, T. J. Visible Photoelectrochemical Water Splitting into H<sub>2</sub> and O<sub>2</sub> in a Dye Sensitized Photoelectrosynthesis Cell. *Proc. Natl. Acad. Sci. U. S. A.* **2015**, *112*, 5899–5902.
- (287) Alibabaei, L.; Farnum, B. H.; Kalanyan, B.; Brennaman, M. K.; Losego, M. D.; Parsons, G. N.; Meyer, T. J. Atomic Layer Deposition of TiO<sub>2</sub> on Mesoporous nanoITO: Conductive Core-Shell Photo-anodes for Dye-Sensitized Solar Cells. *Nano Lett.* **2014**, *14*, 3255–3261.
- (288) Gao, Y.; Ding, X.; Liu, J.; Wang, L.; Lu, Z.; Li, L.; Sun, L. Visible light driven water splitting in a molecular device with unprecedentedly high photocurrent density. *J. Am. Chem. Soc.* **2013**, *135*, 4219–4222.
- (289) Gao, Y.; Zhang, L.; Ding, X.; Sun, L. Artificial photosynthesis - functional devices for light driven water splitting with photoactive anodes based on molecular catalysts. *Phys. Chem. Chem. Phys.* **2014**, *16*, 12008–12013.
- (290) Song, W.; Ito, A.; Binstead, R. A.; Hanson, K.; Luo, H.; Brennaman, M. K.; Concepcion, J. J.; Meyer, T. J. Accumulation of Multiple Oxidative Equivalents at a Single Site by Cross-Surface Electron Transfer on TiO<sub>2</sub>. *J. Am. Chem. Soc.* **2013**, *135*, 11587–11594.
- (291) Kaerkaes, M. D.; Johnston, E. V.; Verho, O.; Aakermark, B. Artificial Photosynthesis: From Nanosecond Electron Transfer to Catalytic Water Oxidation. *Acc. Chem. Res.* **2014**, *47*, 100–111.
- (292) Bottari, G.; Trukhina, O.; Ince, M.; Torres, T. Towards artificial photosynthesis: Supramolecular, donor-acceptor, porphyrin- and phthalocyanine/carbon nanostructure ensembles. *Coord. Chem. Rev.* **2012**, *256*, 2453–2477.
- (293) Murata, K.; Araki, M.; Inagaki, A.; Akita, M. Syntheses, photophysical properties, and reactivities of novel bichromophoric Pd complexes composed of Ru(II)-polypyridyl and naphthyl moieties. *Dalton Trans.* **2013**, *42*, 6989–7001.
- (294) Li, F.; Jiang, Y.; Zhang, B.; Huang, F.; Gao, Y.; Sun, L. Towards A Solar Fuel Device: Light-Driven Water Oxidation Catalyzed by a Supramolecular Assembly. *Angew. Chem., Int. Ed.* **2012**, *51*, 2417–2420.

- (295) Wang, L.; Mirmohades, M.; Brown, A.; Duan, L.; Li, F.; Daniel, Q.; Lomoth, R.; Sun, L.; Hammarström, L. Sensitizer-Catalyst Assemblies for Water Oxidation. *Inorg. Chem.* **2015**, *54*, 2742–2751.
- (296) Herrero, C.; Quaranta, A.; Fallahpour, R.-A.; Leibl, W.; Aukauloo, A. Identification of the Different Mechanisms of Activation of a [RuII(tpy)(OH<sub>2</sub>)<sub>2</sub><sup>+</sup>] Catalyst by Modified Ruthenium Sensitizers in Supramolecular Complexes. *J. Phys. Chem. C* **2013**, *117*, 9605–9612.
- (297) Dietrich, J.; Thorenz, U.; Foerster, C.; Heinze, K. Effects of Sequence, Connectivity, and Counter Ions in New Amide-Linked Ru(tpy)<sub>2</sub>-Re(bpy) Chromophores on Redox Chemistry and Photophysics. *Inorg. Chem.* **2013**, *52*, 1248–1264.
- (298) Norris, M. R.; Concepcion, J. J.; Harrison, D. P.; Binstead, R. A.; Ashford, D. L.; Fang, Z.; Templeton, J. L.; Meyer, T. J. Redox Mediator Effect on Water Oxidation in a Ruthenium-Based Chromophore-Catalyst Assembly. *J. Am. Chem. Soc.* **2013**, *135*, 2080–2083.
- (299) Herrero, C.; Batchelor, L.; Baron, A.; El Ghachoui, S.; Sheth, S.; Guillot, R.; Vauzeilles, B.; Sircoglou, M.; Mallah, T.; Leibl, W.; et al. Click Chemistry as a Convenient Tool for the Incorporation of a Ruthenium Chromophore and a Nickel-Salen Monomer into a Visible-Light-Active Assembly. *Eur. J. Inorg. Chem.* **2013**, *2013*, 494–499.
- (300) Zhang, P.; Wang, M.; Li, C.; Li, X.; Dong, J.; Sun, L. Photochemical H<sub>2</sub> production with noble-metal-free molecular devices comprising a porphyrin photosensitizer and a cobaloxime catalyst. *Chem. Commun.* **2009**, *46*, 8806–8808.
- (301) McCormick, T. M.; Han, Z.; Weinberg, D. J.; Brennessel, W. W.; Holland, P. L.; Eisenberg, R. Impact of Ligand Exchange in Hydrogen Production from Cobaloxime-Containing Photocatalytic Systems. *Inorg. Chem.* **2011**, *50*, 10660–10666.
- (302) Vagnini, M. T.; Smeigh, A. L.; Blakemore, J. D.; Eaton, S. W.; Schley, N. D.; D'Souza, F.; Crabtree, R. H.; Brudvig, G. W.; Co, D. T.; Wasielewski, M. R. Ultrafast photodriven intramolecular electron transfer from an iridium-based water-oxidation catalyst to perylene diimide derivatives. *Proc. Natl. Acad. Sci. U. S. A.* **2012**, *109*, 15651–15656.
- (303) Bock, C. R.; Connor, J. A.; Gutierrez, A. R.; Meyer, T. J.; Whitten, D. G.; Sullivan, B. P.; Nagle, J. K. Estimation of excited-state redox potentials by electron-transfer quenching. Application of electron-transfer theory to excited-state redox processes. *J. Am. Chem. Soc.* **1979**, *101*, 4815–4824.
- (304) Bock, C. R.; Meyer, T. J.; Whitten, D. G. Electron transfer quenching of the luminescent excited state of tris(2,2'-bipyridine)-ruthenium(II). Flash photolysis relaxation technique for measuring the rates of very rapid electron transfer reactions. *J. Am. Chem. Soc.* **1974**, *96*, 4710–4712.
- (305) Demas, J. N.; Adamson, A. W. Tris (2,2'-bipyridine)-ruthenium(II) sensitized reactions of some oxalato complexes. *J. Am. Chem. Soc.* **1973**, *95*, 5159–5168.
- (306) Young, R. C.; Meyer, T. J.; Whitten, D. G. Electron transfer quenching of excited states of metal complexes. *J. Am. Chem. Soc.* **1976**, *98*, 286–287.
- (307) Ellmer, K. Past achievements and future challenges in the development of optically transparent electrodes. *Nat. Photonics* **2012**, *6*, 809–817.
- (308) Hosono, H.; Ohta, H.; Orita, M.; Ueda, K.; Hirano, M. Frontier of transparent conductive oxide thin films. *Vacuum* **2002**, *66*, 419–425.
- (309) van Deelen, J.; Illiberi, A.; Hovestad, A.; Barbu, I.; Klerk, L.; Buskens, P. Transparent conducting materials: overview and recent results. *Proc. SPIE* **2012**, 8470.
- (310) Alibabaei, L.; Luo, H. L.; House, R. L.; Hoertz, P. G.; Lopez, R.; Meyer, T. J. Applications of metal oxide materials in dye sensitized photoelectrosynthesis cells for making solar fuels: let the molecules do the work. *J. Mater. Chem. A* **2013**, *1*, 4133–4145.
- (311) Bahr, J. L.; Tour, J. M. Covalent chemistry of single-wall carbon nanotubes. *J. Mater. Chem.* **2002**, *12*, 1952–1958.
- (312) Cosnier, S. Biomolecule immobilization on electrode surfaces by entrapment or attachment to electrochemically polymerized films. A review. *Biosens. Bioelectron.* **1999**, *14*, 443–456.
- (313) Stein, A.; Wang, Z.; Fierke, M. A. Functionalization of porous carbon materials with designed pore architecture. *Adv. Mater.* **2009**, *21*, 265–293.
- (314) Krumpfer, J. W.; Gao, L.; Fadeev, A. Y.; McCarthy, T. J. Using surface-attached organosilanes to control and understand hydrophobicity and superhydrophobicity. *Adv. Silicon Sci.* **2012**, *4*, 95–114.
- (315) Mirkhalaf, F.; Graves, J. E. Nanostructured electrocatalysts immobilised on electrode surfaces and organic film templates. *Chem. Pap.* **2012**, *66*, 472–483.
- (316) Vannucci, A. K.; Hull, J. F.; Chen, Z.; Binstead, R. A.; Concepcion, J. J.; Meyer, T. J. Water Oxidation Intermediates Applied to Catalysis: Benzyl Alcohol Oxidation. *J. Am. Chem. Soc.* **2012**, *134*, 3972–3975.
- (317) Trammell, S. A.; Meyer, T. J. Diffusional Mediation of Surface Electron Transfer on TiO<sub>2</sub>. *J. Phys. Chem. B* **1999**, *103*, 104–107.
- (318) Langmuir, I. The adsorption of gases on plane surfaces of glass, mica and platinum. *J. Am. Chem. Soc.* **1918**, *40*, 1361–1402.
- (319) Ashford, D. L.; Brennaman, M. K.; Brown, R. J.; Keinan, S.; Concepcion, J. J.; Papanikolas, J. M.; Templeton, J. L.; Meyer, T. J. Varying the Electronic Structure of Surface-Bound Ruthenium(II) Polypyridyl Complexes. *Inorg. Chem.* **2014**, *53*, 460–469.
- (320) Treadway, J. A.; Moss, J. A.; Meyer, T. J. Visible Region Photooxidation on TiO<sub>2</sub> with a Chromophore-Catalyst Molecular Assembly. *Inorg. Chem.* **1999**, *38*, 4386–4387.
- (321) Trammell, S. A.; Moss, J. A.; Yang, J. C.; Nakhle, B. M.; Slate, C. A.; Odobel, F.; Sykora, M.; Erickson, B. W.; Meyer, T. J. Sensitization of TiO<sub>2</sub> by Phosphonate-Derivatized Proline Assemblies. *Inorg. Chem.* **1999**, *38*, 3665–3669.
- (322) Hanson, K.; Wilger, D. J.; Jones, S. T.; Harrison, D. P.; Bettis, S. E.; Luo, H.; Papanikolas, J. M.; Waters, M. L.; Meyer, T. J. Electron transfer dynamics of peptide-derivatized Ru<sup>II</sup>-polypyridyl complexes on nanocrystalline metal oxide films. *Biopolymers* **2013**, *100*, 25–37.
- (323) Springer, J. W.; Parkes-Loach, P. S.; Reddy, K. R.; Krayer, M.; Jiao, J.; Lee, G. M.; Niedzwiedzki, D. M.; Harris, M. A.; Kirmaier, C.; Bocian, D. F.; et al. Biohybrid Photosynthetic Antenna Complexes for Enhanced Light-Harvesting. *J. Am. Chem. Soc.* **2012**, *134*, 4589–4599.
- (324) Wilger, D. J.; Bettis, S. E.; Materese, C. K.; Minakova, M.; Papoian, G. A.; Papanikolas, J. M.; Waters, M. L. Tunable Energy Transfer Rates via Control of Primary, Secondary, and Tertiary Structure of a Coiled Coil Peptide Scaffold. *Inorg. Chem.* **2012**, *51*, 11324–11338.
- (325) Polo, F.; Antonello, S.; Formaggio, F.; Toniolo, C.; Maran, F. Evidence Against the Hopping Mechanism as an Important Electron Transfer Pathway for Conformationally Constrained Oligopeptides. *J. Am. Chem. Soc.* **2005**, *127*, 492–493.
- (326) Ryan, D. M.; Coggins, M. K.; Concepcion, J. J.; Ashford, D. L.; Fang, Z.; Alibabaei, L.; Ma, D.; Meyer, T. J.; Waters, M. L. Synthesis and Electrocatalytic Water Oxidation by Electrode-Bound Helical Peptide Chromophore–Catalyst Assemblies. *Inorg. Chem.* **2014**, *53*, 8120–8128.
- (327) Ma, D.; Bettis, S. E.; Hanson, K.; Minakova, M.; Alibabaei, L.; Fondrie, W.; Ryan, D. M.; Papoian, G. A.; Meyer, T. J.; Waters, M. L.; et al. Interfacial Energy Conversion in Ru<sup>II</sup> Polypyridyl-Derivatized Oligoproline Assemblies on TiO<sub>2</sub>. *J. Am. Chem. Soc.* **2013**, *135*, 5250–5253.
- (328) Hanson, K.; Torelli, D. A.; Vannucci, A. K.; Brennaman, M. K.; Luo, H.; Alibabaei, L.; Song, W.; Ashford, D. L.; Norris, M. R.; Glasson, C. R. K.; et al. Self-assembled Bilayer Films of Ru(II) Polypyridyl Complexes by Layer-by-Layer Deposition on Nanostructured Metal Oxides. *Angew. Chem., Int. Ed.* **2012**, *51*, 12782–12785.
- (329) Ding, X.; Gao, Y.; Zhang, L.; Yu, Z.; Liu, J.; Sun, L. Visible Light-Driven Water Splitting in Photoelectrochemical Cells with Supramolecular Catalysts on Photoanodes. *ACS Catal.* **2014**, *4*, 2347–2350.

- (330) Glasson, C. R. K.; Song, W.; Ashford, D. L.; Vannucci, A.; Chen, Z.; Concepcion, J. J.; Holland, P. L.; Meyer, T. J. Self-Assembled Bilayers on Indium-Tin Oxide (SAB-ITO) Electrodes: A Design for Chromophore-Catalyst Photoanodes. *Inorg. Chem.* **2012**, *51*, 8637–8639.
- (331) Xiang, X.; Fielden, J.; Rodriguez-Cordoba, W.; Huang, Z.; Zhang, N.; Luo, Z.; Musaev, D. G.; Lian, T.; Hill, C. L. Electron Transfer Dynamics in Semiconductor-Chromophore-Polyoxometalate Catalyst Photoanodes. *J. Phys. Chem. C* **2013**, *117*, 918–926.
- (332) Brimblecombe, R.; Koo, A.; Dismukes, G. C.; Swiegers, G. F.; Spiccia, L. Solar-driven Water Oxidation by a Bio-inspired Manganese Molecular Catalyst. *J. Am. Chem. Soc.* **2010**, *132*, 2892–2894.
- (333) Li, L.; Duan, L.; Xu, Y.; Gorlov, M.; Hagfeldt, A.; Sun, L. A photoelectrochemical device for visible light driven water splitting by a molecular ruthenium catalyst assembled on dye-sensitized nanostructured TiO<sub>2</sub>. *Chem. Commun.* **2010**, *46*, 7307–7309.
- (334) Moore, G. F.; Blakemore, J. D.; Milot, R. L.; Hull, J. F.; Song, H.-e.; Cai, L.; Schmuttenmaer, C. A.; Crabtree, R. H.; Brudvig, G. W. A visible light water-splitting cell with a photoanode formed by codeposition of a high-potential porphyrin and an iridium water-oxidation catalyst. *Energy Environ. Sci.* **2011**, *4*, 2389–2392.
- (335) Youngblood, W. J.; Lee, S.-H. A.; Kobayashi, Y.; Hernandez-Pagan, E. A.; Hoertz, P. G.; Moore, T. A.; Moore, A. L.; Gust, D.; Mallouk, T. E. Photoassisted Overall Water Splitting in a Visible Light-Absorbing Dye-Sensitized Photoelectrochemical Cell. *J. Am. Chem. Soc.* **2009**, *131*, 926–927.
- (336) Lee, S.-H. A.; Zhao, Y.; Hernandez-Pagan, E. A.; Blasdel, L.; Youngblood, W. J.; Mallouk, T. E. Electron transfer kinetics in water splitting dye-sensitized solar cells based on core-shell oxide electrodes. *Faraday Discuss.* **2012**, *155*, 165–176.
- (337) Gambardella, A. A.; Bjorge, N. S.; Alspaugh, V. K.; Murray, R. W. Voltammetry of Diffusing 2 nm Iridium Oxide Nanoparticles. *J. Phys. Chem. C* **2011**, *115*, 21659–21665.
- (338) Gambardella, A. A.; Feldberg, S. W.; Murray, R. W. Electron Transfer Dynamics of Iridium Oxide Nanoparticles Attached to Electrodes by Self-Assembled Monolayers. *J. Am. Chem. Soc.* **2012**, *134*, 5774–5777.
- (339) Nakagawa, T.; Bjorge, N. S.; Murray, R. W. Electrogenerated IrO<sub>x</sub> Nanoparticles as Dissolved Redox Catalysts for Water Oxidation. *J. Am. Chem. Soc.* **2009**, *131*, 15578–15579.
- (340) Crabtree, R. H. Resolving Heterogeneity Problems and Impurity Artifacts in Operationally Homogeneous Transition Metal Catalysts. *Chem. Rev.* **2012**, *112*, 1536–1554.
- (341) Cape, J. L.; Hurst, J. K. Detection and Mechanistic Relevance of Transient Ligand Radicals Formed during [Ru(bpy)<sub>2</sub>(OH<sub>2</sub>)<sub>2</sub>O<sub>4+</sub>] Catalyzed Water Oxidation. *J. Am. Chem. Soc.* **2008**, *130*, 827–829.
- (342) Heimer, T. A.; Heilweil, E. J.; Bignozzi, C. A.; Meyer, G. J. Electron Injection, Recombination, and Halide Oxidation Dynamics at Dye-Sensitized Metal Oxide Interfaces. *J. Phys. Chem. A* **2000**, *104*, 4256–4262.
- (343) O'Donnell, R. M.; Ardo, S.; Meyer, G. J. Charge-Screening Kinetics at Sensitized TiO<sub>2</sub> Interfaces. *J. Phys. Chem. Lett.* **2013**, *4*, 2817–2821.
- (344) Hilgendorff, M.; Sundstroem, V. Dynamics of Electron Injection and Recombination of Dye-Sensitized TiO<sub>2</sub> Particles. *J. Phys. Chem. B* **1998**, *102*, 10505–10514.
- (345) Miller, S. A.; West, B. A.; Curtis, A. C.; Papanikolas, J. M.; Moran, A. M. Communication: Uncovering molecule-TiO<sub>2</sub> interactions with nonlinear spectroscopy. *J. Chem. Phys.* **2011**, *135*, 081101–081104.
- (346) Morandeira, A.; Lopez-Duarte, I.; Martinez-Diaz, M. V.; O'Regan, B.; Shuttle, C.; Haji-Zainulabidin, N. A.; Torres, T.; Palomares, E.; Durrant, J. R. Slow electron injection on Ru-phthalocyanine sensitized TiO<sub>2</sub>. *J. Am. Chem. Soc.* **2007**, *129*, 9250–9251.
- (347) Asbury, J. B.; Hao, E.; Wang, Y.; Ghosh, H. N.; Lian, T. Ultrafast Electron Transfer Dynamics from Molecular Adsorbates to Semiconductor Nanocrystalline Thin Films. *J. Phys. Chem. B* **2001**, *105*, 4545–4557.
- (348) Verma, S.; Kar, P.; Das, A.; Palit, D. K.; Ghosh, H. N. The Effect of Heavy Atoms on Photoinduced Electron Injection from Nonthermalized and Thermalized Donor States of MII-Polypyridyl (M = Ru/Os) Complexes to Nanoparticulate TiO<sub>2</sub> Surfaces: An Ultrafast Time-Resolved Absorption Study. *Chem. - Eur. J.* **2010**, *16*, 611–619.
- (349) Benkoe, G.; Kallioinen, J.; Myllyperkio, P.; Trif, F.; Korppi-Tommola, J. E. I.; Yartsev, A. P.; Sundstroem, V. Interligand Electron Transfer Determines Triplet Excited State Electron Injection in RuN<sub>3</sub>-Sensitized TiO<sub>2</sub> Films. *J. Phys. Chem. B* **2004**, *108*, 2862–2867.
- (350) Hasselmann, G. M.; Meyer, G. J. Diffusion-Limited Interfacial Electron Transfer with Large Apparent Driving Forces. *J. Phys. Chem. B* **1999**, *103*, 7671–7675.
- (351) Liu, F.; Meyer, G. J. Remote and Adjacent Excited-State Electron Transfer at TiO<sub>2</sub> Interfaces Sensitized to Visible Light with Ru(II) Compounds. *Inorg. Chem.* **2005**, *44*, 9305–9313.
- (352) She, C.; Guo, J.; Irle, S.; Morokuma, K.; Mohler, D. L.; Zabri, H.; Odobel, F.; Youm, K.-T.; Liu, F.; Hupp, J. T.; et al. Comparison of Interfacial Electron Transfer through Carboxylate and Phosphonate Anchoring Groups. *J. Phys. Chem. A* **2007**, *111*, 6832–6842.
- (353) Gillaizeau-Gauthier, I.; Odobel, F.; Alebbi, M.; Argazzi, R.; Costa, E.; Bignozzi, C. A.; Qu, P.; Meyer, G. J. Phosphonate-based bipyridine dyes for stable photovoltaic devices. *Inorg. Chem.* **2001**, *40*, 6073–6079.
- (354) Durrant, J. R.; Haque, S. A.; Palomares, E. Towards optimization of electron transfer processes in dye sensitised solar cells. *Coord. Chem. Rev.* **2004**, *248*, 1247–1257.
- (355) Dang, X.; Hupp, J. T. Interfacial Charge-Transfer Pathways: Evidence for Marcus-Type Inverted Electron Transfer in Metal Oxide Semiconductor/Inorganic Dye Systems. *J. Am. Chem. Soc.* **1999**, *121*, 8399–8400.
- (356) Boschloo, G.; Hagfeldt, A. Activation Energy of Electron Transport in Dye-Sensitized TiO<sub>2</sub> Solar Cells. *J. Phys. Chem. B* **2005**, *109*, 12093–12098.
- (357) Frank, A. J.; Kopidakis, N.; van de Lagemaat, J. Electrons in nanostructured TiO<sub>2</sub> solar cells: transport, recombination and photovoltaic properties. *Coord. Chem. Rev.* **2004**, *248*, 1165–1179.
- (358) Haque, S. A.; Palomares, E.; Cho, B. M.; Green, A. N. M.; Hirata, N.; Klug, D. R.; Durrant, J. R. Charge Separation versus Recombination in Dye-Sensitized Nanocrystalline Solar Cells: the Minimization of Kinetic Redundancy. *J. Am. Chem. Soc.* **2005**, *127*, 3456–3462.
- (359) McNeil, I.; Ashford, D. L.; Glasson, C. R. K.; Luo, H.; Fecko, C. J. Power-law kinetics in the photoluminescence of dye-sensitized nanoparticle films: Implications for electron injection and charge transport. *J. Phys. Chem. C* **2012**, *116*, 15888–15899.
- (360) McNeil, I. J.; Alibabaei, L.; Ashford, D. L.; Fecko, C. J. Investigation of Factors That Affect Excited State Lifetime Distribution of Dye-Sensitized Nanoparticle Films. *J. Phys. Chem. C* **2013**, *117*, 17412–17420.
- (361) De Angelis, F.; Fantacci, S.; Mosconi, E.; Nazeeruddin, M. K.; Gratzel, M. Absorption Spectra and Excited State Energy Levels of the N719 Dye on TiO<sub>2</sub> in Dye-Sensitized Solar Cell Models. *J. Phys. Chem. C* **2011**, *115*, 8825–8831.
- (362) Wenger, B.; Graetzel, M.; Moser, J.-E. Rationale for Kinetic Heterogeneity of Ultrafast Light-Induced Electron Transfer from Ru(II) Complex Sensitzers to Nanocrystalline TiO<sub>2</sub>. *J. Am. Chem. Soc.* **2005**, *127*, 12150–12151.
- (363) Antila, L. J.; Myllyperkio, P.; Mustalahti, S.; Lehtivuori, H.; Korppi-Tommola, J. Injection and ultrafast regeneration in dye-sensitized solar cells. *J. Phys. Chem. C* **2014**, *118*, 7772–7780.
- (364) Halme, J.; Boschloo, G.; Hagfeldt, A.; Lund, P. Spectral Characteristics of Light Harvesting, Electron Injection, and Steady-State Charge Collection in Pressed TiO<sub>2</sub> Dye Solar Cells. *J. Phys. Chem. C* **2008**, *112*, 5623–5637.
- (365) Bettis, S. E.; Hanson, K.; Wang, L.; Gish, M. K.; Concepcion, J. J.; Fang, Z.; Meyer, T. J.; Papanikolas, J. M. Photophysical Characterization of a Chromophore/Water Oxidation Catalyst Containing a Layer-by-Layer Assembly on Nanocrystalline TiO<sub>2</sub>

- Using Ultrafast Spectroscopy. *J. Phys. Chem. A* **2014**, *118*, 10301–10308.
- (366) Milot, R. L.; Moore, G. F.; Crabtree, R. H.; Brudvig, G. W.; Schmuttenmaer, C. A. Electron Injection Dynamics from Photoexcited Porphyrin Dyes into SnO<sub>2</sub> and TiO<sub>2</sub> Nanoparticles. *J. Phys. Chem. C* **2013**, *117*, 21662–21670.
- (367) Koops, S. E.; Barnes, P. R. F.; O'Regan, B. C.; Durrant, J. R. Kinetic Competition in a Coumarin Dye-Sensitized Solar Cell: Injection and Recombination Limitations upon Device Performance. *J. Phys. Chem. C* **2010**, *114*, 8054–8061.
- (368) Wiberg, J.; Marinado, T.; Hagberg, D. P.; Sun, L.; Hagfeldt, A.; Albinsson, B. Effect of Anchoring Group on Electron Injection and Recombination Dynamics in Organic Dye-Sensitized Solar Cells. *J. Phys. Chem. C* **2009**, *113*, 3881–3886.
- (369) Chang, C.-W.; Luo, L.; Chou, C.-K.; Lo, C.-F.; Lin, C.-Y.; Hung, C.-S.; Lee, Y.-P.; Diau, E. W.-G. Femtosecond Transient Absorption of Zinc Porphyrins with Oligo(phenylethynyl) Linkers in Solution and on TiO<sub>2</sub> Films. *J. Phys. Chem. C* **2009**, *113*, 11524–11531.
- (370) Dos Santos, T.; Morandeira, A.; Koops, S.; Mozer, A. J.; Tsekouras, G.; Dong, Y.; Wagner, P.; Wallace, G.; Earles, J. C.; Gordon, K. C.; et al. Injection Limitations in a Series of Porphyrin Dye-Sensitized Solar Cells. *J. Phys. Chem. C* **2010**, *114*, 3276–3279.
- (371) Myahkostupov, M.; Piotrowiak, P.; Wang, D.; Galoppini, E. Ru(II)-Bpy Complexes Bound to Nanocrystalline TiO<sub>2</sub> Films through Phenyleneethynylene (OPE) Linkers: Effect of the Linkers Length on Electron Injection Rates. *J. Phys. Chem. C* **2007**, *111*, 2827–2829.
- (372) Fessenden, R. W.; Kamat, P. V. Rate Constants for Charge Injection from Excited Sensitizer into SnO<sub>2</sub>, ZnO, and TiO<sub>2</sub> Semiconductor Nanocrystallites. *J. Phys. Chem.* **1995**, *99*, 12902–12906.
- (373) Kuciauskas, D.; Monat, J. E.; Villahermosa, R.; Gray, H. B.; Lewis, N. S.; McCusker, J. K. Transient Absorption Spectroscopy of Ruthenium and Osmium Polypyridyl Complexes Adsorbed onto Nanocrystalline TiO<sub>2</sub> Photoelectrodes. *J. Phys. Chem. B* **2002**, *106*, 9347–9358.
- (374) Benkoe, G.; Kallioinen, J.; Korppi-Tommola, J. E. I.; Yartsev, A. P.; Sundstroem, V. Photoinduced ultrafast dye-to-semiconductor electron injection from nonthermalized and thermalized donor states. *J. Am. Chem. Soc.* **2002**, *124*, 489–493.
- (375) Asbury, J. B.; Anderson, N. A.; Hao, E.; Ai, X.; Lian, T. Parameters affecting electron injection dynamics from ruthenium dyes to titanium dioxide nanocrystalline thin film. *J. Phys. Chem. B* **2003**, *107*, 7376–7386.
- (376) Myahkostupov, M.; Piotrowiak, P.; Wang, D.; Galoppini, E. Ru(II)-Bpy Complexes Bound to Nanocrystalline TiO<sub>2</sub> Films through Phenyleneethynylene (OPE) Linkers: Effect of the Linkers Length on Electron Injection Rates. *J. Phys. Chem. C* **2007**, *111*, 2827–2829.
- (377) Damrauer, N. H.; Boussie, T. R.; Devenney, M.; McCusker, J. K. Effects of Intraligand Electron Delocalization, Steric Tuning, and Excited-State Vibrionic Coupling on the Photophysics of Aryl-Substituted Bipyridyl Complexes of Ru(II). *J. Am. Chem. Soc.* **1997**, *119*, 8253–8268.
- (378) Damrauer, N. H.; McCusker, J. K. Ultrafast Dynamics in the Metal-to-Ligand Charge Transfer Excited-State Evolution of [Ru(4,4'-diphenyl-2,2'-bipyridine)3]2+. *J. Phys. Chem. A* **1999**, *103*, 8440–8446.
- (379) Bettis, S. E.; Ryan, D. M.; Gish, M. K.; Alibabaei, L.; Meyer, T. J.; Waters, M. L.; Papanikolas, J. M. Photophysical Characterization of a Helical Peptide Chromophore-Water Oxidation Catalyst Assembly on a Semiconductor Surface Using Ultrafast Spectroscopy. *J. Phys. Chem. C* **2014**, *118*, 6029–6037.
- (380) Nelson, J.; Haque, S. A.; Klug, D. R.; Durrant, J. R. Trap-limited recombination in dye-sensitized nanocrystalline metal oxide electrodes. *Phys. Rev. B: Condens. Matter Mater. Phys.* **2001**, *63*, 205321–205329.
- (381) Nelson, J.; Chandler, R. E. Random walk models of charge transfer and transport in dye sensitized systems. *Coord. Chem. Rev.* **2004**, *248*, 1181–1194.
- (382) Clifford, J. N.; Palomares, E.; Nazeeruddin, M. K.; Graetzel, M.; Nelson, J.; Li, X.; Long, N. J.; Durrant, J. R. Molecular Control of Recombination Dynamics in Dye-Sensitized Nanocrystalline TiO<sub>2</sub> Films: Free Energy vs Distance Dependence. *J. Am. Chem. Soc.* **2004**, *126*, 5225–5233.
- (383) Bisquert, J. Hopping Transport of Electrons in Dye-Sensitized Solar Cells. *J. Phys. Chem. C* **2007**, *111*, 17163–17168.
- (384) Barzykin, A. V.; Tachiya, M. Mechanism of Charge Recombination in Dye-Sensitized Nanocrystalline Semiconductors: Random Flight Model. *J. Phys. Chem. B* **2002**, *106*, 4356–4363.
- (385) Bisquert, J.; Zaban, A.; Salvador, P. Analysis of the Mechanisms of Electron Recombination in Nanoporous TiO<sub>2</sub> Dye-Sensitized Solar Cells. Nonequilibrium Steady-State Statistics and Interfacial Electron Transfer via Surface States. *J. Phys. Chem. B* **2002**, *106*, 8774–8782.
- (386) Hu, K.; Robson, K. C. D.; Beauvilliers, E. E.; Schott, E.; Zarate, X.; Arratia-Perez, R.; Berlinguette, C. P.; Meyer, G. J. Intramolecular and Lateral Intermolecular Hole Transfer at the Sensitized TiO<sub>2</sub> Interface. *J. Am. Chem. Soc.* **2014**, *136*, 1034–1046.
- (387) Williams, G.; Watts, D. C. Non-symmetrical dielectric relaxation behavior arising from a simple empirical decay function. *Trans. Faraday Soc.* **1970**, *66*, 80–85.
- (388) Adelt, M.; Devenney, M.; Meyer, T. J.; Thompson, D. W.; Treadway, J. A. Ruthenium(II) MLCT Excited States. Stabilization toward Ligand Loss in Rigid Media. *Inorg. Chem.* **1998**, *37*, 2616–2617.
- (389) Thompson, D. W.; Fleming, C. N.; Myron, B. D.; Meyer, T. J. Rigid medium stabilization of metal-to-ligand charge transfer excited states. *J. Phys. Chem. B* **2007**, *111*, 6930–6941.
- (390) Haque, S. A.; Tachibana, Y.; Klug, D. R.; Durrant, J. R. Charge Recombination Kinetics in Dye-Sensitized Nanocrystalline Titanium Dioxide Films under Externally Applied Bias. *J. Phys. Chem. B* **1998**, *102*, 1745–1749.
- (391) Haque, S. A.; Tachibana, Y.; Willis, R. L.; Moser, J. E.; Graetzel, M.; Klug, D. R.; Durrant, J. R. Parameters Influencing Charge Recombination Kinetics in Dye-Sensitized Nanocrystalline Titanium Dioxide Films. *J. Phys. Chem. B* **2000**, *104*, 538–547.
- (392) Gust, D.; Moore, T. A.; Moore, A. L. Mimicking Photosynthetic Solar Energy Transduction. *Acc. Chem. Res.* **2001**, *34*, 40–48.
- (393) Arakawa, H.; Aresta, M.; Armor, J. N.; Barreau, M. A.; Beckman, E. J.; Bell, A. T.; Bercaw, J. E.; Creutz, C.; Dinjus, E.; Dixon, D. A.; et al. Catalysis research of relevance to carbon management: progress, challenges, and opportunities. *Chem. Rev.* **2001**, *101*, 953–996.
- (394) Balzani, V.; Credi, A.; Raymo, F. M.; Stoddart, J. F. Artificial molecular machines. *Angew. Chem., Int. Ed.* **2000**, *39*, 3348–3391.
- (395) Anderson, S.; Constable, E. C.; Dare-Edwards, M. P.; Goodenough, J. B.; Hamnett, A.; Seddon, K. R.; Wright, R. D. Chemical modification of a titanium(IV) oxide electrode to give stable dye sensitization without a supersensitizer. *Nature* **1979**, *280*, 571–573.
- (396) Memming, R.; Schroepel, F. Electron transfer reactions of excited ruthenium(II) complexes in monolayer assemblies at the tin dioxide-water interface. *Chem. Phys. Lett.* **1979**, *62*, 207–210.
- (397) Memming, R.; Schroepel, F.; Bringmann, U. Sensitized oxidation of water by tris(2,2'-bipyridyl) ruthenium at stannic oxide electrodes. *J. Electroanal. Chem. Interfacial Electrochem.* **1979**, *100*, 307–318.
- (398) Gillaizeau-Gauthier, I.; Odobel, F.; Alebbi, M.; Argazzi, R.; Costa, E.; Bignozzi, C. A.; Qu, P.; Meyer, G. J. Phosphonate-based bipyridine dyes for stable photovoltaic devices. *Inorg. Chem.* **2001**, *40*, 6073–6079.
- (399) Kim, D. H.; Losego, M. D.; Hanson, K.; Alibabaei, L.; Lee, K.; Meyer, T. J.; Parsons, G. N. Stabilizing Chromophore Binding on TiO<sub>2</sub> for Long-Term Stability of Dye-Sensitized Solar Cells Using Multicomponent Atomic Layer Deposition. *Phys. Chem. Chem. Phys.* **2014**, *16*, 8615–8622.
- (400) O'Neill, B. J.; Jackson, D. H. K.; Lee, J.; Canlas, C.; Stair, P. C.; Marshall, C. L.; Elam, J. W.; Kuech, T. F.; Dumesic, J. A.; Huber, G.

- W. Catalyst Design with Atomic Layer Deposition. *ACS Catal.* **2015**, *5*, 1804–1825.
- (401) Moss, J. A.; Yang, J. C.; Stipkala, J. M.; Wen, X.; Bignozzi, C. A.; Meyer, G. J.; Meyer, T. J. Sensitization and Stabilization of TiO<sub>2</sub> Photoanodes with Electropolymerized Overlayer Films of Ruthenium and Zinc Polypyridyl Complexes: A Stable Aqueous Photoelectrochemical Cell. *Inorg. Chem.* **2004**, *43*, 1784–1792.
- (402) Szpakolski, K.; Latham, K.; Rix, C.; Rani, R. A.; Kalantar-zadeh, K. Silane: A new linker for chromophores in dye-sensitized solar cells. *Polyhedron* **2013**, *52*, 719–732.
- (403) McNamara, W. R.; Snoeberger, R. C., III; Li, G.; Richter, C.; Allen, L. J.; Milot, R. L.; Schmuttenmaer, C. A.; Crabtree, R. H.; Brudvig, G. W.; Batista, V. S. Hydroxamate anchors for water-stable attachment to TiO<sub>2</sub> nanoparticles. *Energy Environ. Sci.* **2009**, *2*, 1173–1175.
- (404) Zakeeruddin, S. M.; Nazeeruddin, M. K.; Humphry-Baker, R.; Péchy, P.; Quagliotto, P.; Barolo, C.; Viscardi, G.; Grätzel, M. Design, Synthesis, and Application of Amphiphilic Ruthenium Polypyridyl Photosensitizers in Solar Cells Based on Nanocrystalline TiO<sub>2</sub> Films. *Langmuir* **2002**, *18*, 952–954.
- (405) Tamaki, Y.; Vannucci, A. K.; Dares, C. J.; Binstead, R. A.; Meyer, T. J. One-Electron Activation of Water Oxidation Catalysis. *J. Am. Chem. Soc.* **2014**, *136*, 6854–6857.
- (406) Hyde, J. T.; Hanson, K.; Vannucci, A. K.; Lapides, A. M.; Alibabaei, L.; Norris, M. R.; Meyer, T. J.; Harrison, D. P. Electrochemical Instability of Phosphonate-Derivatized, Ru(III) Poly-pyridyl Complexes on Metal Oxide Surfaces. *ACS Appl. Mater. Interfaces* **2015**, *7*, 9554–9562.
- (407) Limburg, B.; Bouwman, E.; Bonnet, S. Molecular water oxidation catalysts based on transition metals and their decomposition pathways. *Coord. Chem. Rev.* **2012**, *256*, 1451–1467.
- (408) Roecker, L.; Kutner, W.; Gilbert, J. A.; Simmons, M.; Murray, R. W.; Meyer, T. J. Instability of the oxidation catalysts  $[(\text{bpy})_2(\text{py})\text{Ru}(\text{O})]^{2+}$  and oxo(1,10-phenanthroline)(2,2',2"-terpyridine)ruthenium(2+)  $[(\text{trpy})(\text{phen})\text{Ru}(\text{O})]^{2+}$  in basic solution. *Inorg. Chem.* **1985**, *24*, 3784–3791.
- (409) Zouni, A.; Witt, H.-T.; Kern, J.; Fromme, P.; Krauss, N.; Saenger, W.; Orth, P. Crystal structure of photosystem II from *Synechococcus elongatus* at 3.8 [angst] resolution. *Nature* **2001**, *409*, 739–743.
- (410) Peek, B. M.; Ross, G. T.; Edwards, S. W.; Meyer, G. J.; Meyer, T. J.; Erickson, B. W. Synthesis of redox derivatives of lysine and related peptides containing phenothiazine of tris(2,2'-bipyridine)-ruthenium(II). *Int. J. Pept. Protein Res.* **1991**, *38*, 114–123.
- (411) Serron, S. A.; Aldridge, W. S., III; Fleming, C. N.; Danell, R. M.; Baik, M.-H.; Sykora, M.; Dattelbaum, D. M.; Meyer, T. J. Evidence for Through-Space Electron Transfer in the Distance Dependence of Normal and Inverted Electron Transfer in Oligoproline Arrays. *J. Am. Chem. Soc.* **2004**, *126*, 14506–14514.
- (412) Wang, J. L.; Wang, C.; deKrafft, K. E.; Lin, W. B. Cross-linked Polymers with Exceptionally High Ru(bipy)<sub>3</sub><sup>2+</sup> Loadings for Efficient Heterogeneous Photocatalysis. *ACS Catal.* **2012**, *2*, 417–424.
- (413) Sun, Y. L.; Chen, Z.; Puodziukynaitė, E.; Jenkins, D. M.; Reynolds, J. R.; Schanze, K. S. Light Harvesting Arrays of Polypyridine Ruthenium(II) Chromophores Prepared by Reversible Addition-Fragmentation Chain Transfer Polymerization. *Macromolecules* **2012**, *45*, 2632–2642.
- (414) Qiu, D.; Zhao, Q.; Bao, X.; Liu, K.; Wang, H.; Guo, Y.; Zhang, L.; Zeng, J.; Wang, H. Electropolymerization and characterization of an alternatively conjugated donor-acceptor metallocopolymer: Poly-[Ru(4'-(4-(Diphenylamino)phenyl)-2,2':6',2"-Terpyridine)2]<sup>2+</sup>. *Inorg. Chem. Commun.* **2011**, *14*, 296–299.
- (415) Fang, Z.; Keinan, S.; Alibabaei, L.; Luo, H.; Ito, A.; Meyer, T. J. Controlled Electropolymerization of Ruthenium(II) Vinylbipyridyl Complexes in Mesoporous Nanoparticle Films of TiO<sub>2</sub>. *Angew. Chem., Int. Ed.* **2014**, *53*, 4872–4876.
- (416) Nakagawa, T.; Beasley, C. A.; Murray, R. W. Efficient Electro-Oxidation of Water near Its Reversible Potential by a Mesoporous IrO<sub>x</sub> Nanoparticle Film. *J. Phys. Chem. C* **2009**, *113*, 12958–12961.
- (417) Concepcion, J. J.; Binstead, R. A.; Alibabaei, L.; Meyer, T. J. Application of the Rotating Ring-Disc-Electrode Technique to Water Oxidation by Surface-Bound Molecular Catalysts. *Inorg. Chem.* **2013**, *52*, 10744–10746.
- (418) Song, W. J.; Brennaman, M. K.; Concepcion, J. J.; Jurss, J. W.; Hoertz, P. C.; Luo, H. L.; Chen, C. C.; Hanson, K.; Meyer, T. J. Interfacial Electron Transfer Dynamics for  $[\text{Ru}(\text{bpy})_2((4,4'\text{-PO}_3\text{H}_2)_2\text{bpy})]^{2+}$  Sensitized TiO<sub>2</sub> in a Dye-Sensitized Photoelectrosynthesis Cell: Factors Influencing Efficiency and Dynamics. *J. Phys. Chem. C* **2011**, *115*, 7081–7091.
- (419) Song, W.; Vannucci, A. K.; Farnum, B. H.; Lapides, A. M.; Brennaman, M. K.; Kalanyan, B.; Alibabaei, L.; Concepcion, J. J.; Losego, M. D.; Parsons, G. N.; et al. Visible Light Driven Benzyl Alcohol Dehydrogenation in a Dye-Sensitized Photoelectrosynthesis Cell. *J. Am. Chem. Soc.* **2014**, *136*, 9773–9779.
- (420) Hocking, R. K.; Brimblecombe, R.; Chang, L.-Y.; Singh, A.; Cheah, M. H.; Glover, C.; Casey, W. H.; Spiccia, L. Water-oxidation catalysis by manganese in a geochemical-like cycle. *Nat. Chem.* **2011**, *3*, 461–466.
- (421) Chen, Z. F.; Vannucci, A. K.; Concepcion, J. J.; Jurss, J. W.; Meyer, T. J. Proton-coupled electron transfer at modified electrodes by multiple pathways. *Proc. Natl. Acad. Sci. U. S. A.* **2011**, *108*, E1461–E1469.
- (422) Lang, Z.-L.; Yang, G.-C.; Ma, N.-N.; Wen, S.-Z.; Yan, L.-K.; Guan, W.; Su, Z.-M. DFT characterization on the mechanism of water splitting catalyzed by single-Ru-substituted polyoxometalates. *Dalton Trans.* **2013**, *42*, 10617–10625.
- (423) Michaux, K. E.; Gambardella, A. A.; Alibabaei, L.; Ashford, D. L.; Sherman, B. D.; Binstead, R. A.; Meyer, T. J.; Murray, R. W. Visible Photoelectrochemical Water Splitting Based on a Ru(II) Polypyridyl Chromophore and Iridium Oxide Nanoparticle Catalyst. *J. Phys. Chem. C* **2015**, *119*, 17023–17027.